Projected Pupil Plane Pattern:an alternative LGS wavefront sensing technique

HUIZHE YANG

Projected Pupil Plane Pattern: an alternative LGS wavefront sensing technique

Huizhe Yang

A thesis presented for the degree of

Doctor of Philosophy

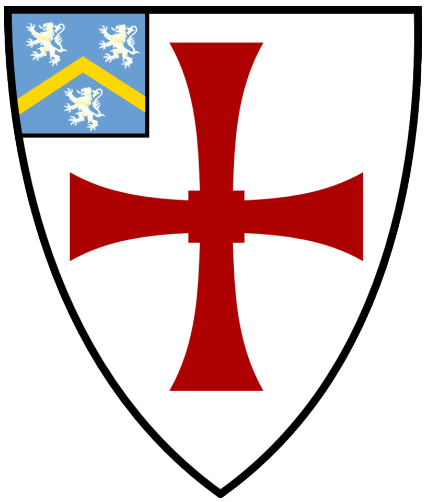

Centre for Advanced Instrumentation

The University of Durham

United Kingdom

June 2019

Dedicated to

my family and my husband Wenfeng Tan

Projected Pupil Plane Pattern: an alternative LGS wavefront sensing technique

Huizhe Yang

Abstract

For the next generation of extremely large telescopes, Focal Anisoplanatism (FA) renders single Laser Guide Star AO useless. Here we analyze a novel LGS alternative configuration with corresponding wavefront sensing and reconstruction method, termed Projected Pupil Plane Pattern, to solve the problem of Focal Anisoplanatism. With PPPP, turbulence is sensed during uplink by a laser beam projected as a collimated beam from the whole telescope primary mirror. Phase changes due to the turbulence introduce intensity variations that then increase in amplitude with propagation distance. By observing the distribution of intensity at two distant planes, the Transport-of-Intensity equation can be used to determine the phase aberration encountered during the uplink path. A simple imaging camera can then be used to measure the wavefront by imaging the backscattered light patterns.

We have successfully demonstrated PPPP works both by simulation and laboratory experiment, where we find that PPPP can achieve equivalent performance to a SH WFS associated with a NGS. However it is shown that the main problem of PPPP is its low Signal-to-Noise Ratio if a 20 W laser is used. To reduce the requirement for high laser power, an alternative reconstructor based upon nonlinear Artificial Neural Networks has been developed, and provides a wavefront with measurement error around 160 nm RMS with a single 200 W laser on a 4-m diameter telescope. PPPP is therefore ready for a practical on-sky test, which we are currently undertaking at Electro Optical Systems (EOS) Debris Laser Ranging (DLR) system, Australia.

Supervisors: Nazim Bharmal and Richard Myers

Acknowledgements

I acknowledge financial support from China Scholarship Council (CSC) for covering the living expenses during my first three years of study, and from Durham University for my last year, as well as the funding of STFC for my PhD project.

I'd like to thank all my CfAI colleagues who have helped me through an incredibly interesting and fulfilling four years. Special thanks go to my previous and current office mates: Daniel, Saavi, Nico, David, Penny, Zhentao, Wenfeng and Wei for creating such a warm and friendly environment to make my PhD life much easier and fun. Thanks to those who also joined the PhD journey: Amrit, Mark, Abi, Dougie, Vlad, Ollie and Xuewen. Thanks also to many others who have provided their advice or their time in helping with my project: Tim Morris, James, Ali Basden, Eddy, Deli, Gorden Love, etc. Especially thanks Andrew and Matt who created the wonderful simulation tool *Soapy*, rescued me from suffering writing thousands of codes. I'd like to thank all my collaborators outside CfAI: David Buscher, Aglae Kellerer, especially Carlos and Javier from Oviedo University for creating a powerful artificial Neural Network, and Craig Smith, James Webb and Mark Blundel from EOS space systems Ltd. for offering us the opportunity to "see" a 760 W laser on-sky, as well as bunches of kangaroos.

I 'd like to thank all my friends from all over the world during these unforgettable four years to make me almost forget my hometown: Rongjuan, Xiangwen, Jiayun, Helen, Yeling, Yangmei, Mengrong, Chi, Ning, Ningning, Junjie, Jianxin,

Bitao, Keying, Xiaotao, Zhengkun, Jin, Fei, Jipeng, Zhao, Tom, Laurence, Duo Amy, Peng and the lovely little girl An. Special thanks to Yonghui for her valuable advice and encouragement. Most importantly, none of this could have happened without my family. Thanks my parents to be so understanding and supportive, and my husband to be so thoughtful and considerate, accompanying me through all the way till the end.

Finally I'd like to thank my supervisors, Ali Bharmal and Richard Myers, for steering me through the long journey of PPPP. And what they have taught me will always continue steering me...

Contents

Declaration

The work in this thesis is based on research carried out at the Centre for Advanced Instrumentation, Department of Physics, University of Durham, England. No part of this thesis has been submitted elsewhere for any other degree or qualification, and it is the sole work of the author unless referenced to the contrary in the text.

Some of the work presented in this thesis has been published in journals and conference proceedings - the relevant publications are listed below.

Publications (Journal Articles)

Chapter 2, 3 and 4:

Huizhe Yang, Nazim A Bharmal, Richard M Myers, *Projected Pupil Plane Pattern: an alternative LGS wavefront sensing technique*, Monthly Notices of the Royal Astronomical Society, Volume 477, Issue 4, July 2018, Pages 4443–4453.

Huizhe Yang, Carlos Gonzalez Gutierrez, Nazim A Bharmal, F J de Cos Juez, *Projected Pupil Plane Pattern (PPPP) with artificial Neural Networks*, Monthly Notices of the Royal Astronomical Society, stz1362 (22 May 2019).

Chapter 5:

Huizhe Yang, Nazim Bharmal, Richard Myers, Eddy Younger, *Laboratory demonstration of an alternative laser guide stars wavefront sensing technique: projected*

pupil plane pattern, J. Astron. Telesc. Instrum. Syst. 5(2) 029002 (7 May 2019).

Publications (Proceedings)

Huizhe Yang, Nazim Barmal, Richard Myers, David F. Buscher, Aglae Kellererc, Tim Morris, and Alastair Basden, *A novel laser guide star: Projected Pupil Plane Pattern*, Proc. AO4ELT5, Jan 2017.

Huizhe Yang, Alastiar Basden, David Buscher, Francisco Javier de Cos Juez, Aglae Kellerer, Tim Morris, Richard Myers, Eddy Younger, Nazim Bharmal, *LGS alternative wave-front sensing: Projected Pupil Plane Pattern (PPPP)*, Proc. SPIE 10703, July 2018.

Nazim A. Bharmal, Richard M. Myers, **Huizhe Yang**, *PPPP: an on-sky experiment for zero-cone effect LGS alternative*, Proc. SPIE 10703, July 2018.

List of Figures

List of Tables

Nomenclature

AO	Adaptive Optics
PPPP	Projected Pupil Plane Pattern
WFS	Wavefront Sensor
DM	Deformable Mirror
RTC	Real Time Control
LGS	Laser Guide Star
NGS	Natural Guide Star
SVD	Singular Value Decomposition
MVM	Matrix Vector Multiplication
WFE	Wavefront Error
SNR	Signal-to-Noise Ratio
SH	Shack-Hartmann
CCD	Charge-Coupled Device
RMS	Root Mean Square

FA	Focal Anisoplanatism
TIE	Transport-of-Intensity Equation
TWE	Transport-of-Wavefront Equation
PSD	Power Spectral Density
FOV	Field of View
FWHM	Full Width Half Maximum
PSF	Point Spread Function
OTF	Optical Transfer Function
SCAO	Single Conjugate AO
MCAO	Multiple Conjugate AO
GLAO	Ground Layer AO
MOAO	Multi-Object AO
LTAO	Laser Tomography AO
XAO	Extreme Adaptive Optics
SR	Strehl Ratio
APD	Avalanche Photo-Diodes
LIDAR	Light Detection And Ranging
ANN	Artificial Neural Network
CNN	Convolutional Neural Network
NN	Neural Network
ELT	Extremely Large Telescope

VLT	Very Large Telescope
LBT	Large Binocular Telescope
ESO	European Southern Observatory
GMT	Giant Magellan Telescope
TMT	Thirty Meter Telescope
E-ELT	ESO Extremely Large Telescope
WHT	William Herschel Telescope
EOS	Electro Optical Systems
DLR	Debris Laser Ranging

Symbols

C_N^2 refractive-index structure coefficient

r_0 Fried's coherence length

L_0 outer scale

l_0 inner scale

k wavenumber ($= 2\pi/\lambda$)

θ_0 isoplanatic angle

τ_0 atmospheric coherence time

η detector quantum efficiency

Z_j j-th Zernike mode

σ^2 wavefront error variance

D telescope diameter

T_0 the transmission of the optical components

T_A the one-way transmission of the atmosphere

Δh laser range gate

Chapter 1

Introduction

1.1 Thesis Aims

Modern astronomical telescopes are designed to observe ever fainter objects in ever greater detail. The size of a telescope primary mirror not only determines how many photons that a telescope can capture from a given source, but also increases the angular resolution with which an object can be imaged. As the size of telescopes increases, the correction for atmospheric turbulence using Adaptive Optics (AO) becomes more critical to achieve diffraction limited performance. Laser Guide Star (LGS) is commonly used to sense the distortion of an optical beam traveling in the Earth's atmosphere without the need for a bright, natural reference source in an AO system. However a main difficulty of LGS AO systems is that for high altitude turbulence layers, the patch of turbulence observed by the LGS will be smaller than that observed by the astronomical scientific target due to the finite LGS altitude. This so-called Focal Anisoplanatism (see Fig. 2.1) becomes more pronounced for larger telescope diameters, such as the proposed next-generation optical ground-based Extremely Large Telescope with primary mirror diameters of over 30 m.

Many approaches have been developed to mitigate the LGS Focal Anisoplanatism, among which Laser Tomography AO (LTAO) (see Fig. 2.5) has demonstrated to be the most successful and commonly-used method. For a LTAO system several

LGSs are generated simultaneously at different positions in the sky. Each LGS is associated with a dedicated Wavefront Sensor (WFS), and measurements from all WFSs are combined to estimate the 3D turbulence. However the LTAO complexity and expense scale with the number of LGSs used.

In this thesis we adopt an alternative LGS configuration proposed by Buscher, Love and Myers[1] called Projected Pupil Plane Pattern (PPPP) (see Fig. 2.13) and its associated wavefront sensing and reconstruction method. The key features of PPPP are that a parallel laser beam is projected from the full primary aperture and that sensing takes place on the upward path. The method relies on an observable modulation of the scattered intensity by turbulence-induced phase distortions during upward propagation of the laser beam. Compared to LTAO, PPPP does not require multiple LGSs. In addition, as a broad collimated laser beam is projected instead of a focused LGS, the safety hazards for aircraft and satellite are reduced significantly.

We have developed the PPPP concept into a sound theoretical framework, confirmed by numerical simulations, and then we designed an optical experiment in the laboratory. This experiment was built from scratch and developed into a successful demonstration with regards to simulation. A collaboration with an industrial partner, EOS, is intended to lead to the on-sky prototype stage.

1.2 Adaptive Optics architecture

Adaptive Optics systems are designed to correct wavefront distortions in light that has propagated through a turbulent medium, such as the Earth's atmosphere. Regardless of their application (such as astronomical imaging, retinal imaging and laser communication systems), all AO systems require an element to measure the wavefront distortions present (*i.e.* WFS), an adaptive optical element to correct them (wavefront corrector or Deformable Mirror (DM)), and finally a control system linking these two components together (Real Time Control (RTC)). As the

PPPP is proposed to reduce Focal Anisoplanatism for astronomical AO systems, we will discuss astronomical AO related topics in this section, including the atmospheric turbulence which is the cause of using AO systems, AO components such as WFS and LGS, and the calibration and reconstruction processes.

1.2.1 Atmospheric turbulence

The atmospheric turbulence is caused by the mixing of large air masses with different temperatures. These local temperature variations thus produce changes in the refractive index of air. The magnitude of the refractive index fluctuations depends on the air density as well as on the range of the temperature variations. Air density is greatest at sea level and decays exponentially with height. Optical effects of turbulence therefore generally decrease with altitude. The effect of atmospheric turbulence on the image of a point source is depicted in Fig. 1.1. If there is no turbulence (left side in Fig. 1.1), then the image at the focal plane of a telescope will be an Airy disk with $2.44\lambda/D$ width (where λ is the imaging wavelength and D is the telescope diameter). However with the presence of turbulence, the received wavefront at the pupil of the telescope will not be a plane wave, therefore the image becomes speckled for short exposure time, and smoothed but much wider for a long exposure with width equaling $2.44\lambda/r_0$ (right side in Fig. 1.1). The parameter r_0 is called Fried's coherence length, which is used to characterize the turbulence strength and will be discussed in section 1.2.1.2.

1.2.1.1 Kolmogorov power spectrum

In 1941 Kolmogorov[2] proposed a mathematical description of the statistical properties of the turbulence. In this model energy is added to the air over a large spatial scale, the "outer-scale" L_0, which breaks down to ever smaller scales, eventually reaching an "inner-scale" l_0 whereby the energy is dissipated as friction between molecules. Values of l_0 have been measured to be in the range of 1 mm to 10 mm[3].

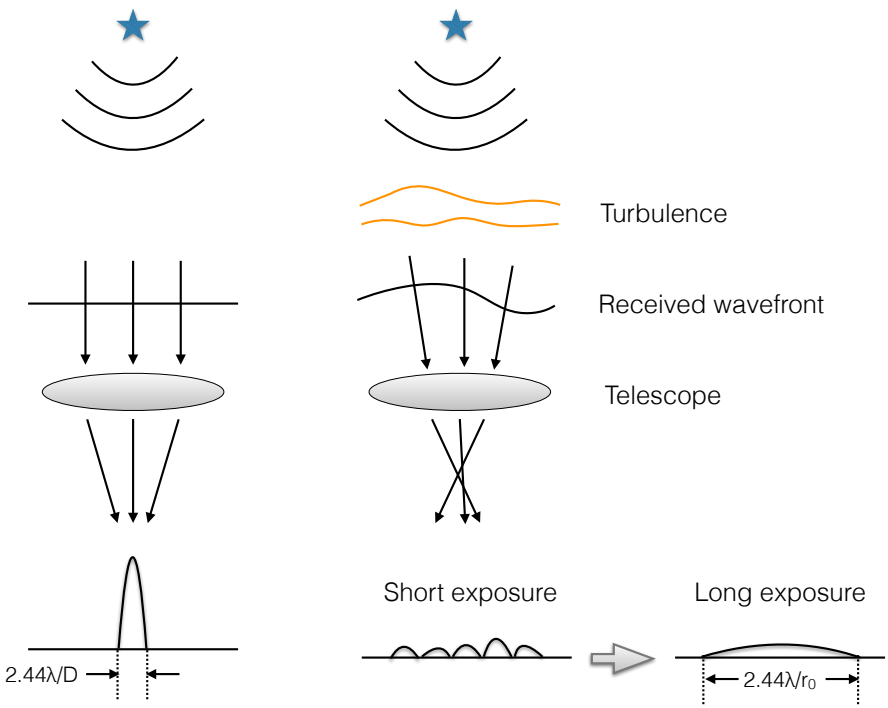

Figure 1.1: Effects of turbulence on the image of a star.

It is likely that L_0 varies greatly and has been measured to range from 10 m to 50 m and even up to 300 m[4].

Kolmogorov's mathematical model defines the power spectrum of the turbulence refractive index as

$$\Phi_N^K(\kappa) = 0.033 C_N^2 \kappa^{-11/3}, \tag{1.1}$$

where $\kappa = 2\pi/l$ and l is the scale size of the fluctuations, and C_N^2 is the refractive-index structure coefficient, a measure of the strength of turbulence. The Kolmogorov power spectrum (equation 1.1) is only valid for spatial separations between the inner scale and the outer scale. In the Kolmogorov valid regime, the power spectrum follows the $-11/3$ power law. Von Kármán[5] deduced another power spectrum of the turbulence, which accounts for both the inner and outer scales, termed modified von Kármán power spectrum

$$\Phi_N^{mvK}(\kappa) = 0.033 C_N^2 \frac{\exp\left(-\kappa^2/\kappa_m^2\right)}{(\kappa^2 + \kappa_0^2)^{11/6}}, \tag{1.2}$$

where $\kappa_m = 5.92/l_0$ and $\kappa_0 = 2\pi/L_0$[6].

1.2.1.2 Fried's coherence length

Fried[7] found that the maximum allowable diameter of a collector before atmospheric distortion seriously limits the telescope performance is r_0, thus it is called Fried's coherence length and defined as

$$r_0 = \left[0.423k^2 \sec(\beta) \int_0^L C_N^2(h)dh\right]^{-3/5}. \tag{1.3}$$

In this expression, the wavenumber $k = 2\pi/\lambda$, L is the path length, β is the zenith angle and C_N^2 can vary with altitude h. It is clear that r_0 decreases with integrated C_N^2 and zenith angle, and increases with wavelength. Average values of r_0 are generally in the range of 7 to 12 cm at a wavelength of 500 nm[8].

The significance of r_0 is that it defines an aperture size over which the mean-square wavefront error is 1 rad^2. The image spread due to atmospheric turbulence for long exposures is given by $2.44\lambda/r_0$ (shown in Fig. 1.1).

From r_0, the turbulence coherence time τ_0, which defines how fast an AO system needs to be, can be defined as

$$\tau_0 = 0.314\frac{r_0}{\bar{v}}, \tag{1.4}$$

where $\bar{v}$ is the wind velocity averaged over the altitude.

The angular anisoplanatism[8], produced by the angular separation of two optical paths in the atmosphere, can also be expressed as a function of r_0

$$\theta_0 = 0.314(\cos\beta)\frac{r_0}{\bar{h}}, \tag{1.5}$$

where θ_0 is known as the "isoplanatic angle" over which there is 1 rad^2 of wavefront error variance, and $\bar{h}$ is the average height of the height-weighted turbulence layers, equaling

$$\bar{h} = \left(\frac{\int_0^\infty C_N^2(h)h^{5/3}dh}{\int_0^\infty C_N^2(h)dh}\right)^{3/5}. \tag{1.6}$$

1.2.2 Adaptive Optics operation

Astronomical Adaptive Optics is designed to remove aberrations caused by the atmospheric turbulence from the optical path between a celestial object and the imaging device. When this is fully achieved, the quality of the image should be limited only by the size of the telescope aperture and achieve the diffraction limited resolution $2.44\lambda/D$. A typical astronomical AO system is shown in Fig. 1.2. Light from a distant reference source, initially undistorted, passes through the turbulent atmosphere and is collected by the telescope (not shown in Fig. 1.2). The distorted optical beam then passes via the DM and is split by the beamsplitter into two parts. One goes into the WFS, where the residual uncorrected wavefront is measured. The other part goes into the scientific instrument to image the distant science target. The control system provides the voltage commands to the DM to generate a replica residual wavefront measured from the WFS. If the light from the celestial object is insufficient for determining the wavefront, supplemental sources, such as nearby Natural Guide Star (NGS) or artificial LGS, are then used. This configuration is termed closed loop AO system.

In contrast, an open loop AO system is shown in Fig. 1.3. Here the WFS does not observe any DM correction and sees the whole turbulence. The open loop mode of operation provides challenges for the design of a WFS as large dynamic range is required. For the closed loop mode, errors in the output voltages to the DM can be corrected for as information on the DM is observed by the WFS. They can, however, affect the open loop performance of the system as aberrations due to DM control errors cannot be seen and corrected. For this reason open loop systems are only used when the alternative closed loop configuration is not feasible, such as in a Multi-Object AO (MOAO) system.

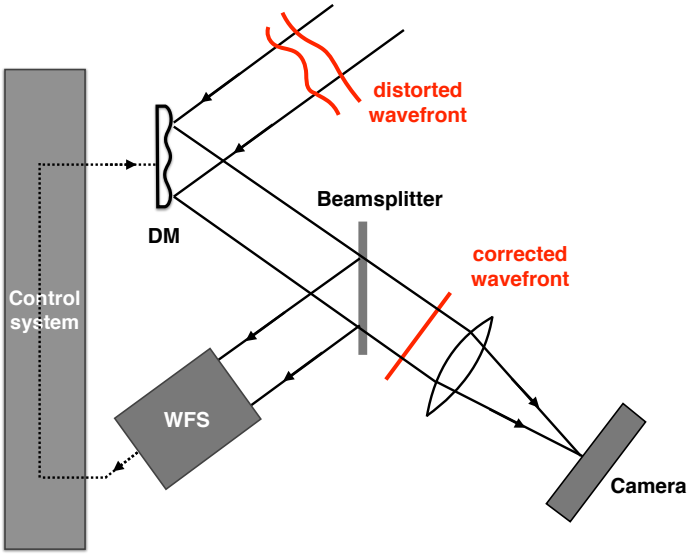

Figure 1.2: Schematic overview of closed loop adaptive optics.

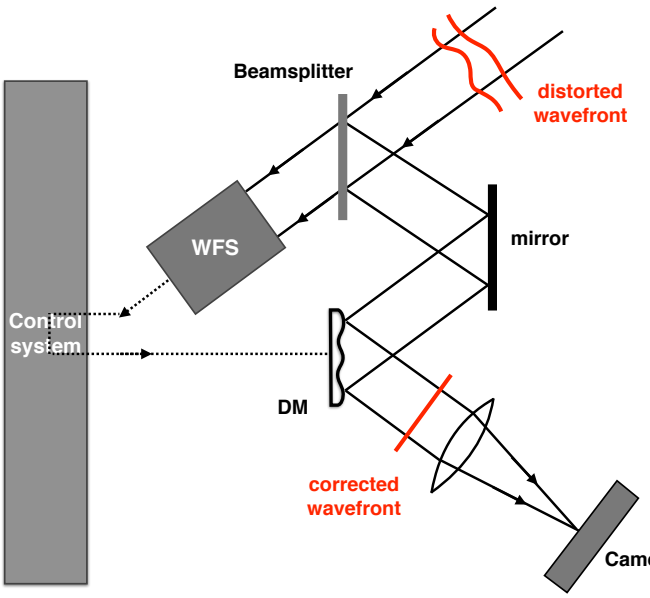

Figure 1.3: Schematic overview of open loop adaptive optics.

1.2.3 Wavefront Sensor

The problem of measuring wavefront distortions is common to optics systems (*e.g.* in the fabrication and control of telescope mirrors), and typically is solved by using interferometers. However it is seldom used in AO systems due to the following reasons[8]:

- an AO system must use the light of stars (or scattered light from the LGSs) passing through the turbulent atmosphere to measure the distorted wavefronts, and hence use incoherent (and sometimes non-point) sources;
- the interference fringes generated by interferometers are chromatic. A WFS must use the photons very efficiently and filtering the stellar light to narrow wavelength bandwidth is not a good option;
- interferometers have an intrinsic phase ambiguity of 2π, whereas atmospheric phase distortions exceed 2π, typically. A WFS must be linear over the full range of atmospheric distortions. There are algorithms to "unwrap" the phase and to remove this ambiguity, but they are slow. Atmospheric turbulence evolves fast, on a millisecond time scale, therefore a WFS must be fast.

The solution to the problem of wavefront sensing in astronomical AO is to measure the direction of propagation of the optical wavefront rather than its optical phase. This is done by measuring the wavefront gradients or curvature within an array of zones covering the telescope aperture. The most frequently used type of WFSs is the Shack-Hartmann (SH) WFS (see section 1.2.3.1), and there are other types of WFSs such as curvature WFS (see section 1.2.3.2), pyramid WFS and shearing interferometers. Here we only discuss the first two types due to their relevance to this thesis's topic.

1.2.3.1 Shack-Hartmann WFS

The basic operation of a SH WFS is illustrated in Fig. 1.4. An image of the exit pupil is projected onto a lenslet array (a collection of small identical lenses). Each lens takes a small part of the aperture, called a sub-aperture, and forms an image of the source. All images are formed on the same detector, typically a Charge-Coupled Device (CCD). When an incoming wavefront is planar, all images are located in a regular grid defined by the lenslet array geometry. As soon as the wavefront is distorted, the images become displaced from their normal positions. Displacements of image centroids in two orthogonal directions x, y are proportional to the average wavefront slopes in x, y over the sub-apertures. Thus, a SH WFS measures the wavefront slopes. The wavefront itself can be reconstructed from the arrays of measured slopes, up to a "piston" constant which is of no importance for imaging. The spatial resolution of a SH WFS is equal to the sub-aperture size. A good feature of the SH WFS is that as it is completely achromatic, the slopes do not depend on the wavelength. It can also work on non-point (extended) sources.

1.2.3.2 Curvature WFS

The curvature WFS was developed by Roddier[9] since 1988. A simple curvature WFS employs two detector arrays located at the near and far sides of the focal plane as shown in Fig. 1.5. Local wavefront curvature causes differences in the intensity at corresponding detector locations at these two planes, producing signals proportional to the wavefront curvature. These two images at the near and far sides of the focal plane are defocused pupil images but blurred and scaled. To limit the blurring to less than the projected size of a sub-aperture (typically r_0), the defocusing length l should satisfy[9][8]

$$l \geq \frac{\lambda f^2}{\lambda f + r_0^2}, \tag{1.7}$$

where f is the focal length of the telescope. Larger defocusing length l is needed to measure the wavefront with higher resolution from equation 1.7. But the sens-

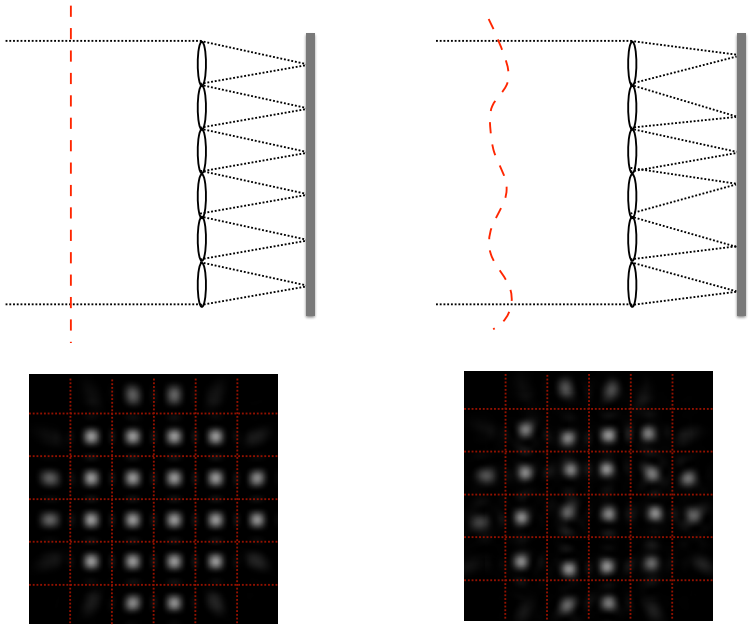

Figure 1.4: An illustration of the SH WFS. Sub-aperture boundaries are denoted by red dotted grids and the distortions of some spots on the edge is caused by their partial illumination through the corresponding edge sub-apertures.

itivity of a curvature WFS decreases with l[9], thus the sensitivity will be reduced accordingly with larger l. This means that a curvature WFS has problems for sensing high-order aberrations.

The curvature WFSs that actually work in astronomical AO systems (*e.g.* the Hokupa'a system[10]) use the Avalanche Photo-Diodes (APD)[11] as light detectors. They are single-pixel devices, like photo-multipliers. The individual photons are detected and converted to electrical pulses with no readout noise and small dark current. Individual segments of the pupil are isolated by a lenslet array, then the light from each segment is focused and transmitted to the corresponding APD via an optical fiber. The number of APDs is equal to the number of segments. Outer segments sample the edge of the aperture, and their signals are proportional to the wavefront gradients along the normal.

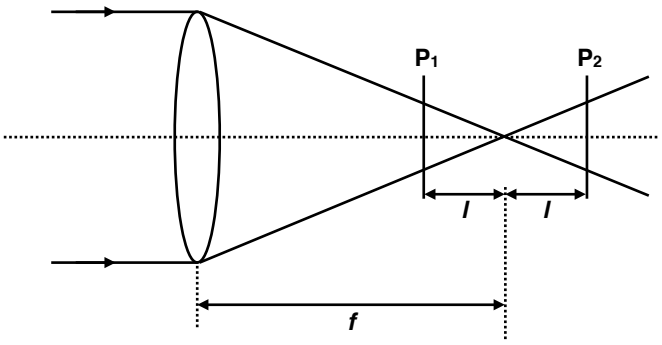

Figure 1.5: Curvature WFS using displaced focal planes.

1.2.4 Laser Guide Stars

1.2.4.1 Sky coverage

AO systems based on NGSs are only effective within an isoplanatic distance of a suitable guide source, and this guide source should be bright enough to feed the WFS. "Sky coverage" is an expression of the percentage of the sky which includes such a NGS available for correction. This probability can be estimated from star counts (see for instance Bahcall and Soneira 1981[12], which is shown in Fig. 1.6). The sky coverage value is hugely dependent upon the particular AO system and the requirements of the AO instrument to fulfill its science cases. Following Roddier[13] here we limit ourselves to a general discussion of the effect of WFS noise on the residual Wavefront Error (WFE), and establish a minimum requirement of the star brightness. To do this, we will use the criterion that the Wavefront Error due to WFS noise should not exceed the error due to the uncompensated wave-front modes. The WFE variance caused by limited photon number $< \sigma^2_{\text{photon}} >$ can be expressed as[12]

$$\langle \sigma^2_{\text{photon}} \rangle \approx \frac{4\pi^2 d^2}{P r_0^2}, \tag{1.8}$$

where d is the size of the sub-aperture, and P represents the number of photons per sub-aperture. To apply useful correction, $< \sigma^2_{\text{photon}} >$ should not exceed the

order of AO correction. According to Noll[14], the residual WFE variance (in rad^2) after removal of the first j Zernike modes (see section 1.2.5.1) are

$$\begin{aligned}
&\Delta_1 = 1.0299(D/r_0)^{5/3}, \quad \Delta_2 = 0.582(D/r_0)^{5/3}, \\
&\Delta_3 = 0.134(D/r_0)^{5/3}, \quad \Delta_4 = 0.111(D/r_0)^{5/3}, \\
&\Delta_j \approx 0.2944 j^{-\sqrt{3}/2}(D/r_0)^{5/3}, \quad \text{for large } j.
\end{aligned} \tag{1.9}$$

If the NGS is used to provide correction of the first j Zernike modes, then we have

$$\begin{aligned}
\frac{4\pi^2 d^2}{P r_0^2} &\leq 0.2944 j^{-\sqrt{3}/2}(D/r_0)^{5/3}, \quad \text{or} \\
P &\geq \frac{4\pi^2 d^2}{0.2944} j^{\sqrt{3}/2} r_0^{-1/3} D^{-5/3}.
\end{aligned} \tag{1.10}$$

Astronomers express the brightness of a star in stellar magnitudes m and for $\lambda = 0.63\,\mu$m, the photon flux per second per cm^2 per μm for a magnitude m star according to Roddier[13] is

$$p = 8 \times 10^6 \times 10^{-0.4m} \quad \text{photons } /(\text{s} \times \text{ cm}^2 \times \ \mu\text{m}). \tag{1.11}$$

The number of photons detected per sub-aperture then can be expressed as

$$P = 8 \times 10^{10-0.4m} d^2 \tau T \int \eta(\lambda) d\lambda, \tag{1.12}$$

where τ is the integration time (s), T is the transmission of the system, and $\eta(\lambda)$ is the detector quantum efficiency (λ is expressed in micrometers). Note that the unit of d is meters instead of centimeters. Combining equation 1.10, 1.11 and 1.12, we know that

$$m \leq \left\{ 10 - \log_{10} \left[\frac{\frac{4\pi^2 d^2}{0.2944} j^{\sqrt{3}/2} r_0^{-1/3} D^{-5/3}}{8 d^2 \tau T \int \eta(\lambda) d\lambda} \right] \right\} /0.4. \tag{1.13}$$

Assume that $T = 0.4$, $\int \eta(\lambda) d\lambda = 0.3\,\mu$m, $\tau = 2.5$ ms, and $r_0 = 0.1$ m at $0.63\,\mu$m for a $D = 4$ m telescope, then it is easy to compute that the star magnitude $m \leq 10.71$ when $j = 78$ at $0.63\,\mu$m, and $m \leq 13.95$ if the NGS is only used for tip/tilt correction.

Another key point for the sky coverage is the maximum distance between the

NGS and the scientific target. Again we will use the criterion that the Wavefront Error due to the angular anisoplanatism should not exceed the error due to the uncompensated wave-front modes. The angular anisoplanatic error is described as[8]

$$\sigma_\theta^2 = \left(\frac{\theta}{\theta_0}\right)^{5/3}, \tag{1.14}$$

where θ_0 is given by equation 1.5. Assume the average weighted turbulence height $\bar{h}$ is 1 km, then we know that $\theta_0 = 6.47$ arcsec for $r_0 = 0.1$ m at 630 nm. Again σ_θ^2 should not exceed the j-th order of correction, which is shown in equation 1.9, therefore we can calculate that the offset angle θ between the NGS and target should be $\theta \leq 12.9$ acrsec when $j = 78$, and $\theta \leq 77.6$ arcsec if used only for tip/tilt correction.

Combining the requirement for the maximum star magnitude and maximum distance, it gives a $\sim 10^{-4}$ sky coverage for 78 Zernike order of AO correction ($m \leq 10.71$ and $\theta \leq 12.9$ acrsec), but more than 1% sky coverage for a NGS tip/tilt system ($m \leq 13.95$ and $\theta \leq 77.6$ arcsec) according to Fig. 1.6. If we increase the wavelength to J, H and K band (with the central wavelength equaling 1.22, 1.65 and 2.2 μm respectively), then the maximum star magnitude for NGS tip/tilt system can be pushed to $m \approx 14.3$, and the maximum distance can be increased to 171.4, 246.3, 347.8 arcsec. Therefore the corresponding sky coverage becomes approximately 10%, 50% and full sky.

1.2.4.2 Rayleigh and Sodium LGSs

To increase the sky coverage two types of Laser Guide Stars are created (Rayleigh and sodium). A Rayleigh LGS is created by propagating a beam into the atmosphere and observing the light backscattered from molecules in the atmosphere. As the atmospheric air pressure decreases with altitude, the scattered return also decreases, which limits the altitude of Rayleigh LGS to around 20-25 km[15]. The lasers should be pulsed so that backscattered light from low altitudes can be eliminated by range gating, therefore a fast shuttering mechanism synchronised with the

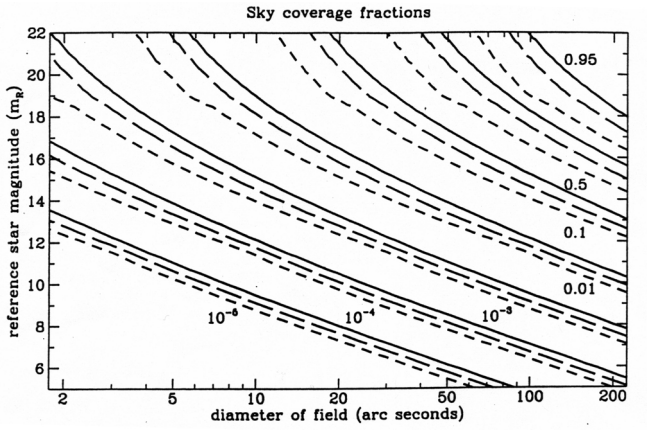

Figure 1.6: Sky coverage (credit to Bahcall and Soneira 1981[12]). Full, long and short dash lines refer to the Galactic plane, middle latitude and Galactic pole)

pulsed laser is required. More commonly, LGSs are created using a sodium laser which is used to excite sodium atoms in the mesospheric sodium layer (around 90 km) causing them to emit light at 589 nm[16].

1.2.4.3 Problems with LGSs

LGSs have been successfully used as an alternative to NGSs to increase the sky coverage[17], but there exist particular problems when using LGS AO systems:

- Tip/tilt indeterminacy;
- Focal Anisoplanatism.

Tip/tilt indeterminacy is caused by the fact that the position of a laser beam projected from the ground is randomly perturbed by the atmospheric turbulence. Therefore the displacement of the laser beam measured by the WFS combines the tip/tilt information from both the upward and downward propagation of the laser beam, whereas only the downward part can provide usable tip/tilt. Take the worst case, if a laser beam is projected on-axis through a telescope, the backscattered light will always appear to be on-axis when viewed through the same telescope, irrespective of any wavefront distortion. Therefore the overall tip/tilt provided by

the LGSs can not be used to determine the turbulence tip/tilt information. It is necessary to use a separate NGS for the tip/tilt measurement for LGS AO systems. Focal Anisoplanatism is another error source when using LGSs, because the patch of turbulence observed by the LGS will be smaller than that observed by the astronomical scientific target due to the finite LGS altitude (see Fig. 2.1). This so-called Focal Anisoplanatism becomes more pronounced for larger telescope diameters, such as the proposed next-generation optical ground-based Extremely Large Telescope (ELT) with primary mirror diameters of over 30 m. The WFE caused by Focal Anisoplanatism can reach ∼155 nm Root Mean Square (RMS) on the 10-m Keck telescope, Hawaii, US[18], and over 300 nm RMS for ELTs. A detailed description regarding Focal Anisoplanatism is presented in section 2.1.

1.2.5 Calibration and Reconstruction

1.2.5.1 Zonal and modal operation

There are two methods of specifying AO calibration and reconstruction: zonal and modal. In the zonal approach, the aperture is divided into an array of independent sub-apertures or zones. Modal analysis treats wavefront as the sum of whole-aperture functions of increasing complexity. The most familiar modal functions in optics are the Zernike polynomials for a circular aperture.

Zernike polynomials are defined in polar coordinates on a unit circle as functions of both azimuthal and radial frequency, denoted by m and n respectively. Noll[14] defined a numbering scheme that is commonly used when describing atmospheric turbulence with Zernike polynomials. The set of Zernike polynomials is defined as

$$\begin{aligned} Z_{\text{even},j} &= \sqrt{n+1}R_n^m(r)\sqrt{2}\cos(m\theta), \\ Z_{\text{odd},j} &= \sqrt{n+1}R_n^m(r)\sqrt{2}\sin(m\theta), \\ Z_j &= \sqrt{n+1}R_n^0(r), \quad m=0, \end{aligned} \tag{1.15}$$

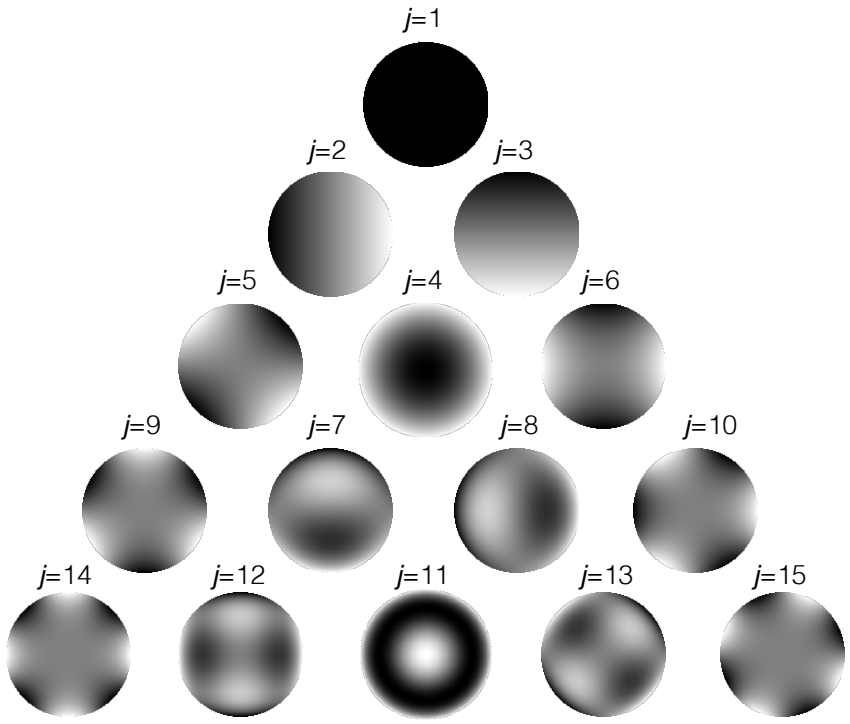

Figure 1.7: The first 15 Zernike polynomials.

where

$$R_n^m(r) = \sum_{S=0}^{(n-m)/2} \frac{(-1)^S (n-S)! r^{n-2S}}{S!\,[(n+m)/2-S]!\,[(n-m)/2-S)]!}. \tag{1.16}$$

In this expression r and θ are polar coordinates and the j value is the order of the Zernike numbering system. Low-order Zernike polynomials correspond to familiar wavefront aberrations, such as tip/tilt, defocus, astigmatism and coma. The first 15 Zernike polynomials are shown in Fig. 1.7.

1.2.5.2 Calibration and reconstruction

AO reconstruction is employed to convert the measured WFS data $\vec{s}$ to DM commands $\vec{d}$ to be sent to the DM. The most commonly used approach is to measure and invert the system "interaction matrix" $\mathbf{M}$, which can be obtained by activating each DM actuator (zonal) or generating individual Zernike modes on the DM (modal), and recording the corresponding measurements from the WFSs. This

calibration process can be expressed as

$$\vec{s} = \mathbf{M}\vec{d}. \tag{1.17}$$

The "interaction matrix" $\mathbf{M}$ is of a size given by the number of WFS measurements times number of DM actuators. Once $\mathbf{M}$ is obtained, it is necessary to invert it, and in this way we can estimate the required DM commands $\vec{d}_{\text{est}}$ from the WFS measurement $\vec{s}$ according to

$$\vec{d}_{\text{est}} = \mathbf{W}\vec{s}, \tag{1.18}$$

where $\mathbf{W}$ is called the control matrix, or command matrix, and $\mathbf{WM} \approx \mathbf{I}$ (the identity matrix). The control matrix will be of size (number of DM actuators times number of WFS measurements). This operation is termed Matrix Vector Multiplication (MVM). The advantage of MVM is that misalignments, rotations and offsets between the DM and WFS in the system are encoded within the interaction and subsequent control matrices.

1.2.6 AO performance

The residual WFE variance σ^2 (in rad^2) after AO correction is the most straightforward method to estimate the performance of an AO system. From the WFE, the Strehl Ratio (SR)[19] representing the normalized peak intensity of a point source can be computed from the relation[20]

$$S = \exp(-\sigma^2). \tag{1.19}$$

This approximation holds true for the case of low WFE variance, less than 1 rad^2, but begins to break down as the error becomes larger than that.

1.3 Review of Adaptive Optics systems

The idea of AO was proposed by Babcock[21], and the first AO systems were developed in the late 1960s for laser beam control. The real-time atmospheric compensator (RTAC) developed by the Advanced Research Projects Agency (ARPA)

was the first success with AO imaging[8], including a 21-actuator AO system. Since then several scientific organizations started developing astronomical AO systems in the mid-1980s, such as the National Optical Astronomy Observatory (NOAO) and the European Southern Observatory (ESO). After 1992 much of the AO development funded by the U.S. government was made available to the scientific community, and there has been a rush to equip the leading observatories with the most advanced AO systems. According to the timeline of AO development, it can be divided into NGS AO systems, LGS AO systems, tomography AO systems for wide field and the next generation Extremely Large Telescopes under planning. It is useful to have a knowledge of the state of the art technologies: current and future. In this section we summarize the prominent AO systems in terms of NGS AO systems, LGS AO systems, tomography AO systems and future ELT AO systems.

1.3.1 NGS AO systems

NGS AO systems are in common use at many observatories around the world. The Keck telescopes were the first of the 8-m class observatories to be equipped with AO[22], followed by others such as Subaru[23], Gemini[24][25] and the Very Large Telescope (VLT)[26]. Recently, Extreme Adaptive Optics (XAO) systems have received much attention for exoplanet studies where very high Strehl Ratio is required. Palm 3000, SPHERE Adaptive Optics for exoplanet observation (SAXO)[27] and the Gemini Planet Imager (GPI)[24] are examples of such systems. A selection of NGS AO sytsems are listed in Table 1.1.

1.3.2 LGS AO systems

To increase the sky coverage (see section 1.2.4.1), a number of LGS AO systems have been built, and current prominent LGS AO systems are listed in Table 1.2.

AO system	**Telescope (m)**	**WFS**	**DM**	**First light**
PUEO[13]	Canada-France-Hawaii Telescope (3.6)	19 subap curvature	Bimorph DM	1996
Keck AO Facility[22]	Keck (10)	20×20 SH	Xinetics 349 actuators	1999
Cassegrain AO system[23]	Subaru (8.2)	36 subap curvature	CILAS 36 actuators	2000
NAOS[26]	VLT UT4(8)	14×14 or 7×7 SH	CILAS 185 actuators	2001
ALTAR[25]	Gemini north (8.1)	12×12 SH	Xinetics 177 actuators	2002
NAOMI[28]	William Hershel Telescope (4.2)	8×8 SH	Trex Enterprises 76 segments	2003
PALM-3000[29] (XAO)	Palomar (5.1)	64×64 SH	Xinetics 349 and 3368 actuators	2011
SAXO[27] (XAO)	VLT UT3 (8)	40×40 SH	CILAS 41×41 actuators	2014
GPI[24] (XAO)	Gemini South (8.1)	43×43 SH	CILAS 9×9 and Boston 4096 actuators	2014

Table 1.1: A selection of currently operating NGS AO sytems.

As shown in Table 1.2, most of the LGS AO systems use sodium LGSs, located at $\sim 90\,\mathrm{km}$, to reduce the Focal Anisoplanatism.

1.3.3 Tomography AO systems

Until now all the AO systems described have used only one single guide star (either NGS or LGS) paired with one DM. Such a system is termed Single Conjugate AO (SCAO) since the DM is conjugate to a single plane, normally the telescope pupil. To increase the Field of View (FOV), it is necessary to measure the turbulence at more than one position in the field. By using multiple guide stars together with multiple associated WFSs, tomography AO systems can significantly improve the FOV from several arcseconds to a few arcminutes. There are three tomography modes: Multiple Conjugate AO (MCAO), Ground Layer AO (GLAO) and Multi-Object AO (shown in Fig. 1.8). Their commonality is that several guide stars are placed at different positions in the field to sample the turbulent volume and thereby increase the FOV, and their differences are as follows:

- **MCAO**: using a number of DMs, conjugate to different altitudes, in order to compensate the turbulence by layers and thus extend the FOV; good compensation within a large FOV;
- **GLAO**: only one DM is used, to correct the ground layer of turbulence; moderate compensation within a large FOV;
- **MOAO**: one DM is placed (conjugate to the telescope pupil) in order to correct all turbulence along each specific direction; good compensation for each chosen direction.

Laser Tomography AO (LTAO) is another AO mode using multiple LGSs, but only for a narrow FOV. The main goal of LTAO system is to reduce the Focal Anisoplanatism. Several LGSs are therefore placed in a narrow field, using tomo-

AO system	**Telescope (m)**	**Laser**	**WFS**	**DM**	**First light**
Starfire Optical Range[30]	(1.5)	75 or 200 W Rayleigh pulsed LGS (Copper vapor)	124 or 208 subap SH	Itek 149 or 241 actuators	1994
Lick AO system[16]	Shane Telescope (3)	18 W sodium pulsed dye laser	37 subap SH	127 actuators (61 active)	1996
Keck LGS AO system[31]	Keck (10)	12 W sodium Nd:YAG CW	20×20 SH	Xinetics 349 actuators	2004
ALTAIR[32]	Gemini notrh (8.1)	12 W CW sodium	12×12 SH	Xinetics 177 actuators	2006
Subaru LGS AO system[33]	Subaru (8.2)	4 W CW sodium	36 subap curverture	CILAS 36 actuators	2006
ESO LGS facility[34]	VLT UT4 (8)	13 W CW sodium dye laser			2006
UnISIS[35]	Mount Wilson (2.5)	20 W Rayleigh UV pulsed LGS	12×12 SH	Xinetics 177 actuators	2009
RoboAO[36]	Palomar (1.5)	10 W Rayleigh UV pulsed LGS	11×11 SH	Boston MEMS DM 120 actuators	2012

Table 1.2: A selection of currently operating LGS AO sytems.

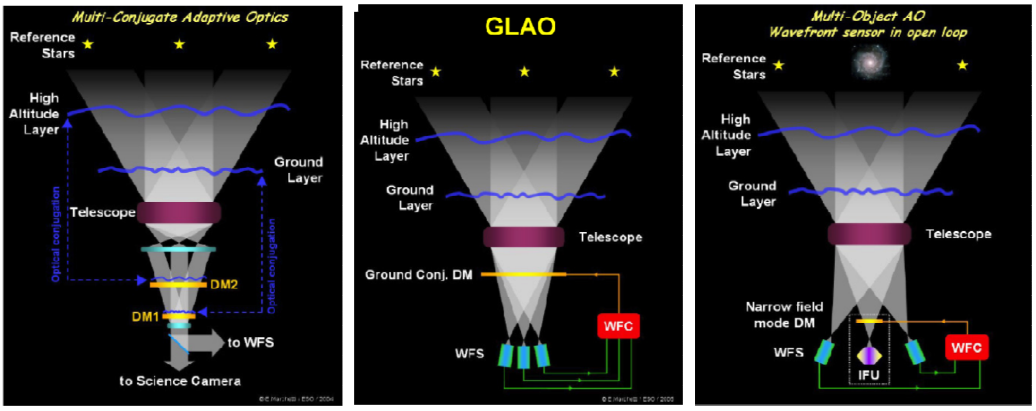

Figure 1.8: Wide field AO systems: MCAO, GLAO and MOAO. Credit to ESO.

graphic reconstruction technique to compute the whole volume of the turbulence. Examples of MCAO, GLAO, MOAO and LTAO systems are listed in Table 1.3.

1.3.4 Future Extremely Large Telescope AO systems

Increasing the telescope aperture can significantly improve the light-collecting power, as well as increase the diffraction limited resolution. A few extremely large telescopes with the primary mirror diameter approximately 30 m are under design. The major ELTs include the Giant Magellan Telescope (GMT), Thirty Meter Telescope (TMT) and ESO Extremely Large Telescope (E-ELT). One of the major challenges that face the future ELTs is their associated AO systems[44]. A summary of the AO system and telescope instruments for GMT, TMT and E-ELT is listed in Table 1.4.

1.4 Error budget in AO

The error budget in AO is a very useful tool for performance estimation when designing an AO system. It consists of an evaluation of all error sources that would degrade the final level of correction an AO system is able to achieve. These error sources are quantified using analytic expressions and/or the result of realistic simulations. The error sources in an AO system are summarized in Fig. 1.9,

AO system	**Telescope (m)**	**guide stars**	**FOV**	**First light**
CANARY[37][38][39] (MOAO) open loop	William Hershel Telescope (4.2)	3 NGSs plus 4 Rayleigh LGSs		2015
GeMS[40] (MCAO) 2 DMs (conj. to 0 and 9 km)	Gemini south (8.1)	5 sodium LGSs in 1 arcmin	85 arcsec	2011
ARGOS[41] (GLAO)	Large Binocular Telescope (8.4)	6 Rayleigh LGSs (3 per LBT side)	4 arcmin	2015
AOF GALACSI [42] (LTAO)	VLT UT4 (8)	4 sodium LGSs in 10 arcsec	7.5 arcsec	2018

Table 1.3: A selection of currently operating tomography AO sytems. LBT features two 8-m telescopes side by side, each one equipped with one AO system, as well as a secondary Deformable Mirror. ARGOS provides a factor of 2-3 times improvement compared to natural seeing, *i.e.* no AO. GeMS MCAO system gave a typical performance of SR $\approx$ 18%, 10% and 4% in K, H and J bands respectively. Canary MOAO system showed a 30.1%, 21.4% and 17.1% H band SR in SCAO, MOAO and GLAO mode respectively. Also the tomography error is $\sim$200 nm[43].

Telescope (m) and instrument	**E-ELT (39.3)**	**GMT (24.5)**	**TMT (30)**
SCAO (NGS)	METIS HARMONI MICADO	GMTNIRS	NFIRAOS+IRIS
MCAO (NGS+LGS)	MICADO-MAORY		NFIRAOS +IRIS/IRMS
LTAO (LGS)	HARMONI	GMTIFS GMTNIRS	
GLAO (NGS)		G-CLEF GMACS	WFOS
MOAO (NGS+LGS)	MOSAIC		TMT-AGE

Table 1.4: AO systems and telescope instruments for TMT, GMT and E-ELT. HARMONI[45]: High angular resolution monolithic optical and near-infrared integral field spectrograph; MAORY[46]: multi-conjugate AO relay; METIS[47]: mid-infrared ELT thermal imager and spectrograph; MICADO[48]: multi-adaptive optics imaging camera for deep observations; MOSAIC[49]: multi-object spectrograph for Astrophysics, inter galactic medium, and cosmology. G-CLEF[50]: GMT consortium large earth finder; GMTIFS[51]: GMT integral-field spectrograph; GMACS[52]: GMT multi-object astronomical and cosmological spectrograph; GMTNIRS[53]: GMT near-infrared spectrograph. NFIRAOS[54]: narrow-field infrared AO system; IRIS[55]:infrared imager and spectrograph; IRMS[56]:infrared multi-object spectrograph; TMT-AGE[57]: TMT analyzer for galaxies in the early universe; WFOS: wide-field optical spectrometer.

where the links between the error sources with the external conditions and the AO instrument characteristics are shown as well. The external factors include the structure and dynamics of the atmosphere and the characteristics of the guide star. Example parameters relating to the external factors and the AO instrument system are as follows:

- $r_0 = 0.1\,\mathrm{m}$ at $500\,\mathrm{nm}$; the average wind velocity is $10\,\mathrm{m/s}$; offset angle $\theta = 2$ arcsec; the total photon number is 10^4;
- telescope diameter $D = 4\,\mathrm{m}$; 10×10 sub-aperture SH WFS (4×4 pixels for each sub-aperture); 11×11 actuators DM; $1\,\mathrm{ms}$ delay time; a sodium LGS at $90\,\mathrm{km}$.

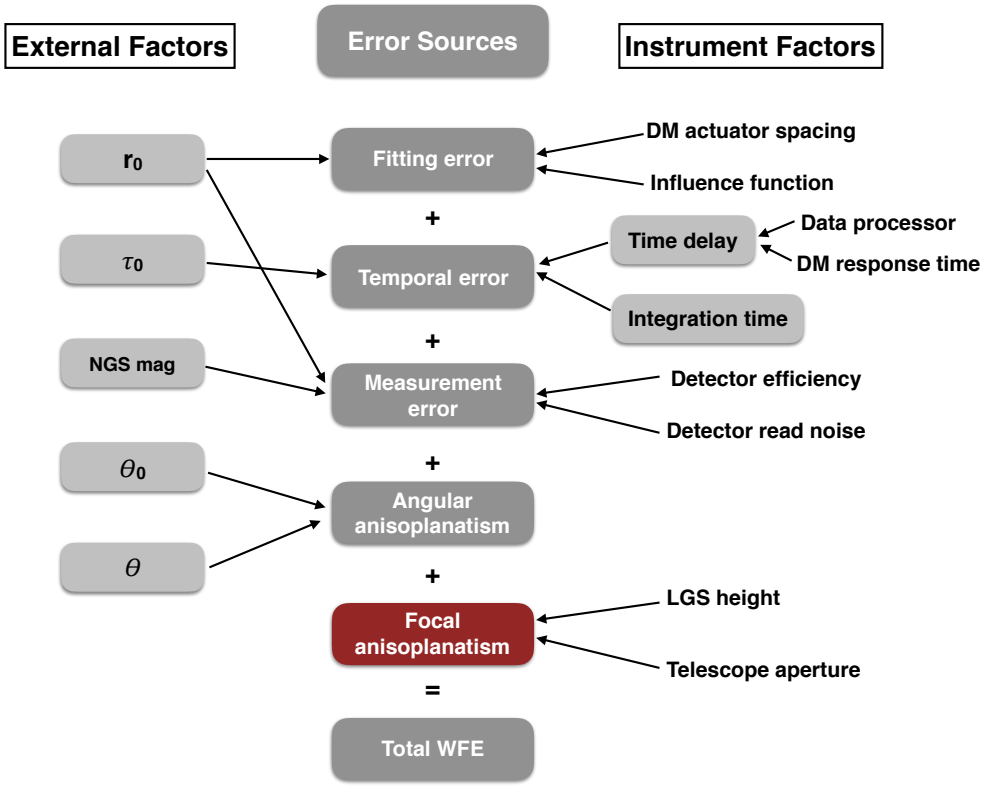

Figure 1.9: Main error sources in AO systems. θ_0 is the isoplanatic angle and θ is the offset angle of the guide star from the target.

1.4.1 Wavefront & tip/tilt measurement error

The wavefront measurement error depends on two characteristics of the guide stars: its brightness (determining the Signal-to-Noise Ratio (SNR)) and its angular size. Tyson[58] gave the analytical expression of the wavefront measurement error for a SH WFS (using 4×4 pixels per sub-aperture) as

$$\begin{aligned} \sigma^2_{\mathrm{WFS}} &= \left[\frac{\pi^2 K_q}{4 \times \mathrm{SNR}}\right]^2 \left[(1.5)^2 + \left(s\frac{d}{\lambda}\right)^2\right] \quad d < r_0, \\ &= \left[\frac{\pi^2 K_q}{4 \times \mathrm{SNR}}\right]^2 \left[\left(1.5\frac{d}{r_0}\right)^2 + \left(s\frac{d}{\lambda}\right)^2\right] \quad d > r_0, \end{aligned} \tag{1.20}$$

where K_q is the loss factor due to the gap between the detector elements (= 1.3 - 1.5), and s is the size of the source (in radian). For a NGS or an object at infinity,

$s = 0$. The SNR for the SH WFS is

$$\mathrm{SNR} = \frac{n_p}{\left[n_p + N_{\mathrm{pixel}}\sigma^2_{\mathrm{noise}}\right]^{1/2}}. \tag{1.21}$$

In this expression, n_p is the number of signal electrons in each sub-aperture, σ_{noise} is the noise electron RMS and N_{pixel} represents the number of pixels in each sub-aperture (equaling $4 \times 4 = 16$). Assume $n_p = 100$, $N_{\mathrm{pixel}} = 16$ and $\sigma_{\mathrm{noise}} = 3$, the corresponding SNR is 6.4. Assume K_q is 1.4, $d = D/10 = 0.4\,\mathrm{m}$ (a 10×10 SH WFS is used) and $r_0 = 0.1\,\mathrm{m}$ at 500 nm, the WFE variance caused by the measurement error becomes 1.73 rad^2 (equivalent to **221** nm RMS at $\lambda = 1.06\,\mu$m).

For tip/tilt SH WFS (2×2 sub-aperture), the WFE variance in rad^2 is

$$\begin{aligned} \sigma^2_{\mathrm{TT}} &= \left(\frac{3\pi K_q \lambda}{16 r_0 \times \mathrm{SNR}}\right)^2 \quad r_0 < D/2, \\ &= \left(\frac{3\pi K_q \lambda}{8 D \times \mathrm{SNR}}\right)^2 \quad r_0 > D/2, \end{aligned} \tag{1.22}$$

where D is the telescope diameter. Normally it is the case that $r_0 < D/2$. If the same NGS is used, the SNR for tip/tilt WFS should be around $\sqrt{10^2/2^2} \approx 5$ times that of the high-order WFS, equaling 48.6. Again K_q is 1.4 and $r_0 = 0.1\,\mathrm{m}$ at 500 nm, thus the tip/tilt measurement error is 1.2×10^{-5} nm RMS at $1.06\,\mu$m when $r_0 < D/2$.

1.4.2 Temporal error

Temporal error is caused by the atmosphere turbulence changes between the WFS measurement and DM correction. The variance of the temporal error can be expressed as[8]

$$\sigma^2_{\mathrm{temp}} = \left(\frac{\tau_s}{\tau_0}\right)^{5/3}, \tag{1.23}$$

where τ_0 ($=0.314 r_0/\bar{v}$) is the atmospheric coherence time and τ_s is the delay between the measurement and correction.

Assume $\bar{v} = 10\,\mathrm{m/s}$ and $r_0 = 0.1\,\mathrm{m}$ at 500 nm, and then we have $\tau_0 = 7.73\,\mathrm{ms}$ at $1.06\,\mu$m. Assume the system delay time $\tau_s = 1\,\mathrm{ms}$. The temporal error is then 0.033 rad^2 (equivalent to **31** nm RMS at $1.06\,\mu$m).

1.4.3 Fitting error

Fitting error is caused by the finite correction resolution of the DM. Hudgin[59] deduced the general expression of the fitting error as

$$\sigma_F^2 = a_F \left(\frac{d}{r_0}\right)^{5/3}, \tag{1.24}$$

where d is the sub-aperture size and a_F is the fitting error coefficient, dependent on the influence function of the DM. For a Gaussian influence function $a_F = 0.24$ rad^2[8]. Again for a 10×10 SH WFS, d should be $D/10$ equaling 0.4 m for a 4-m telescope. Therefore $\sigma_F^2 = 0.54$ rad^2 (equivalent to **124** nm RMS at 1.06 μm) if $r_0 = 0.1$ m at 500 nm.

1.4.4 Angular anisoplanatism

As described in section 1.2.1.2, the "isoplanatic angle" θ_0 (equation 1.5) is a very important parameter when computing the angular anisoplanatism, which is caused by the difference between the directions of the guide starts and the scientific target. In Hardy's book[8] it shows that the WFE variance due to angular anisoplanatism is

$$\sigma_A^2 = \left(\frac{\theta}{\theta_0}\right)^{5/3}. \tag{1.25}$$

If $\bar{h} = 1$ km and $r_0 = 0.1$ m at 500 nm, then $\theta_0 = 15.96$ arcsec. If the offset angle θ is 2 arcsec, we can calculate that $\sigma_A^2 = 0.03$ rad^2 (equivalent to **29.9** nm RMS at 1.06 μm).

In terms of tip/tilt, the anisoplanatic error for a small separation angle θ is[8]

$$\sigma_{TA}^2 = \left(\frac{\theta}{\theta_{TA}}\right)^2, \tag{1.26}$$

where θ_{TA} can be written as

$$\theta_{TA} = \left[0.668k^2 \sec^3(\beta) D^{-1/3} \int C_N^2(h) h^2 dh\right]^{-1/2}. \tag{1.27}$$

To be consistent with the previous error budget analysis, here we use one-layer turbulence profile with $C_N^2(1\text{km}) = 6.9 \times 10^{-16}\,\text{m}^{-2/3}$ (therefore the integrated r_0

equals 0.1 m at 500 nm and $\bar{h} = 1$ km). In this way $\theta_{TA} = 63$ arcsec and thus the tip/tilt angular anisoplanatic error is 5.3 nm RMS at 1.06 μm.

1.4.5 Focal Anisoplanatism

Focal Anisoplanatism error only exists in LGS AO systems, and is caused by the finite LGS height (10-25 km for Rayleigh LGS and 90 km for sodium LGS). The main purpose of this thesis is to eliminate the Focal Anisoplanatism by using an alternative LGS technique. Detailed description of Focal Anisoplanatism is shown in section 2.1. If $C_N^2(1\text{km}) = 6.9 \times 10^{-16}\,\text{m}^{-2/3}$ is used again as in section 1.4.4, also a sodium LGS located at 90 km is used, then the Focal Anisoplanatism error is **39.2** nm RMS at 1.06 μm.

1.4.6 AO performance estimation

The error budget from the above analysis is summarized in Table 1.5. In this example we assumed a fixed flux amount for both NGS and LGS. But it is generally true that the LGS can generate more light than the NGS, therefore the high-order wavefront measurement error for NGS AO system is normally larger than that caused by the LGS AO system. From Table 1.5 it suggests that for this specific example, the wavefront measurement error and fitting error are the two major error sources. The wavefront measurement error can be reduced by increasing the guide star brightness, as well as reducing the detector noise. The fitting error decreases with the number of degrees of freedom in the DM, and in most cases it is built into the hardware design and is not easily changed. Although for this specific example the WFE caused by Focal Anisoplanatism is relatively small, but it can be fatal if a 10-m class or even larger telescope, or other turbulence profiles with more high-altitude layers are used (section 2.1). The emphasis of this thesis is to reduce the

	NGS AO system	LGS AO system
Tip/tilt measurement	NGS	NGS
high-order wavefront	NGS	LGS
Error sources		
tip/tilt		
tip/tilt measurement error	~ 0	~ 0
temporal error	31	31
angular anisoplanatism error	5.3	5.3
high-order wavefront		
wavefront measurement error	221	221
temporal error	31	31
Fitting error	124	124
angular anisoplanatism error	29.9	29.9
focus anioplanatism error		39.2

Table 1.5: WFE RMS (nm) from each error source for a 4-m telescope.

Focal Anisoplanatism using an alternative LGS wavefront sensing technique (see chapter 2).

1.5 Summary

In this chapter we gave a brief introduction to AO architecture, a review of past, current and future AO systems, and an analysis of an example error budget in AO. Major AO theories and techniques are described in section 1.2. Section 1.3 summarizes prominent AO systems including NGS AO systems, LGS AO systems, tomography AO systems and future ELTs. The analytic expressions for error sources of measurement error, temporal error, fitting error and angular and Focal Anisoplanatism error are illustrated in section 1.4, with a performance estimation showing the WFE value from each error source given some typical parameters in an AO system.

Chapter 2

Focal Anisoplanatism: the problem and the solution

2.1 Focal Anisoplanatism

The creation of a LGS within the atmosphere necessitates a finite altitude beacon and light therefore travels back from the LGS to the telescope through a cone (see Fig. 2.1). This is not a problem if the object one is trying to observe lies within the

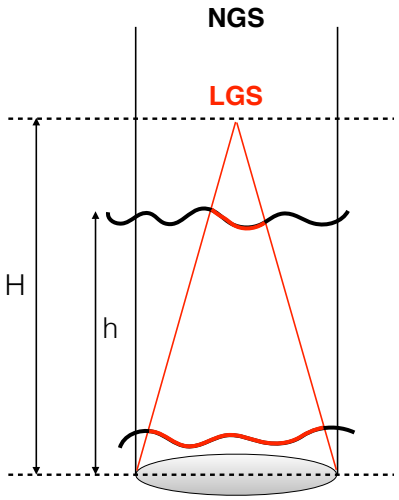

Figure 2.1: An illustration of Focal Anisoplanatism. The turbulence probed by the NGS is a black cylinder, while it is a red cone for the LGS due to the finite altitude of the LGS. The difference between the cylinder and the cone leads to wavefront error measured by the LGS.

atmosphere, but for astronomical AO where the object of interest always lies outside the atmosphere, the volume of turbulence probed by the LGS will be different to that probed by the astronomical science target. Specifically the measurement of the accumulated wavefronts that is afforded by a LGS neglects turbulence above the LGS and includes incorrectly sampled turbulence below the LGS. This form of error is referred to as Focal Anisoplanatism, or the "cone effect", and is illustrated in Fig. 2.1. There are three distinct effects due to the Focal Anisoplanatism:

- The turbulence above H is not sensed by the LGS;
- The outer portions of the NGS wavefront below H are not sensed;
- The LGS wavefront (shown as the red cone) and NGS wavefront (shown as the black cylinder) below H are scaled differently: the laser meta-pupil diameter is reduced by $(1 - h/H)$. Hence, there is a differential "stretching" between the LGS and NGS wavefronts.

The variance in the difference of the integrated wavefronts between the LGS and NGS is dependent on the vertical distribution of turbulence, given by the turbulence profile. The wavefront variance due to Focal Anisoplanatism is given by

$$\sigma^2_{\mathrm{FA}} = \left(\frac{D}{d_0}\right)^{5/3}, \tag{2.1}$$

according to Fried[60], where D is the telescope diameter and the value of d_0, which is wavelength dependent, is derived as

$$d_0 = \left\{ k^2 \left[0.057\mu_0^+(H) + 0.5\frac{\mu_{5/3}^-(H)}{H^{5/3}} - 0.452\frac{\mu_2^-(H)}{H^2} \right] \right\}^{-3/5}, \tag{2.2}$$

where H is the altitude of the LGS, k is the wavenumber, and μ_0^+, $\mu_{5/3}^-$ and μ_2^- are partial turbulence moments, defined as

$$\begin{aligned} \mu_m^+ &= \int_H^\infty C_n^2(h) h^m dh, \\ \mu_m^- &= \int_0^H C_n^2(h) h^m dh. \end{aligned} \tag{2.3}$$

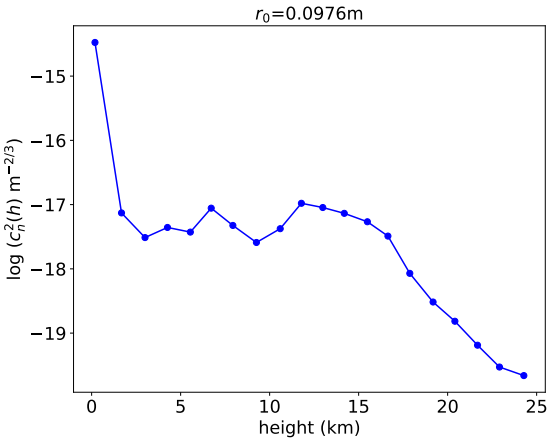

Figure 2.2: One representative optical turbulence profile from ESO Paranal[61] with r_0 equaling 0.0976 m at 500 nm. It is a 20-layers turbulence measurement. The x-axis height is above the observatory.

The first term in equation 2.2 ($0.057\mu_0^+(H)$) is associated with the unsensed turbulence above the LGS. The terms with μ^- represent the difference between the parallel rays from the NGS and the rays originating from the LGS traveling between the LGS altitude and the ground. From equation 2.1, 2.2 and 2.3, we can estimate σ^2_{FA} given the LGS altitude H, telescope diameter D and the turbulence profile. From one representative optical turbulence profile measured at ESO Paranal[61] with r_0 equaling 0.0976 m at 500 nm (see Fig. 2.2), Fig. 2.3 shows σ^2_{FA} in terms of D and H. Fig 2.3 shows that Focal Anisoplanatism becomes more pronounced for larger telescope, so though single sodium laser (around 90 km) systems can provide acceptable performance for current 10-m class telescopes at near infrared science wavelengths, a single LGS is not adequate for next generation ELT scale systems with the primary mirror larger than 30 m (and observational wavelengths in the near infrared or optical). Focal Anisoplanatism also decreases with the altitude of the LGS, hence a single Rayleigh LGS is rarely used for AO systems on current large telescopes.

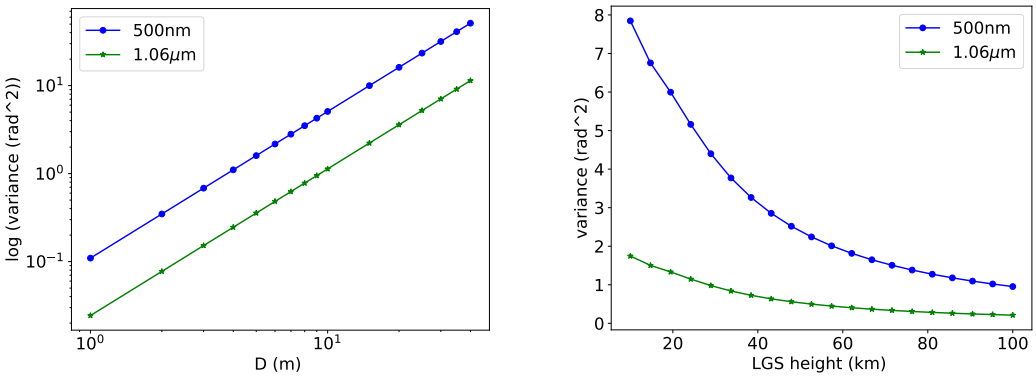

(a) σ^2_{FA} with D (b) σ^2_{FA} with H

Figure 2.3: The wavefront error variance due to focal anisoplanatism σ^2_{FA} in terms of different telescope diameter D and the LGS height H. We have used two laser wavelengths (500 nm and 1.06 μm) as examples to show the effect of the wavelength. It is obvious that the Focal Anisoplanatism decreases with the LGS wavelength. $H = 90\,\mathrm{km}$ is used for Fig. 2.3a and $D = 4\,\mathrm{m}$ is used for Fig. 2.3b.

2.2 Solutions to Focal Anisoplanatism

2.2.1 Stitching

Since the error resulting from Focal Anisoplanatism has been shown to have a $D^{5/3}$ dependence, Parenti[62] proposed the deployment of multiple LGSs, with each of them devoted to correcting one section of the complete telescope aperture (see Fig. 2.4). By using multiple LGSs, the aperture area serviced by each LGS is reduced to a dimension comparable to d_0 (equation 2.1). Conceptually the WFE variance due to Focal Anisoplanatism σ^2_{FA} can be reduced to $N_{\mathrm{LGS}}^{-5/6}\sigma^2_{\mathrm{FA}}$ since the effective collection aperture for each LGS would be $D/N_{\mathrm{LGS}}^{1/2}$. The wavefront measurements made with each LGS must then be combined or "stitched" together to obtain the best estimated overall wavefront.

However this approach will introduce error sources caused by the sub-aperture tip/tilt due to the upward LGS propagation. For a single LGS the overall tip/tilt is discarded because it must be provided by a NGS. Overall tip/tilt measurement errors associated with a single LGS are therefore irrelevant. This is not the case

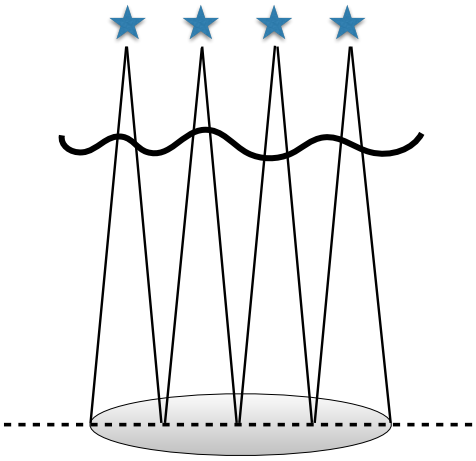

Figure 2.4: Multiple LGSs sampling geometry, where each of the LGSs lies directly above the center of its respective section.

when multiple LGSs are used, because the tip/tilt belonging to each LGS represents higher order wavefront components across the whole telescope pupil, and therefore must be determined and corrected accurately. It has been demonstrated that these sub-aperture tip/tilt errors can be as significant as the Focal Anisoplanatism[8], thus "stitching" has never been implemented or tested on-sky (except a simulation study carried out by Viard[63]). Instead the common solution to the Focal Anisoplanatism is to use multiple laser beams for reconstructing the 3D turbulence perturbations (this is called tomography, see section 2.2.2).

2.2.2 Laser Tomography AO

Laser Tomography AO is a common solution to Focal Anisoplanatism, by attempting to fully illuminate the cylinder of the turbulence sampled by the NGS, with multiple LGSs whose individual wavefronts are analyzed tomographically (see Fig. 2.5). A tomographic reconstructor is achieved by accepting measurements from multiple WFSs (associated with the dedicated LGSs) observing in various dir-

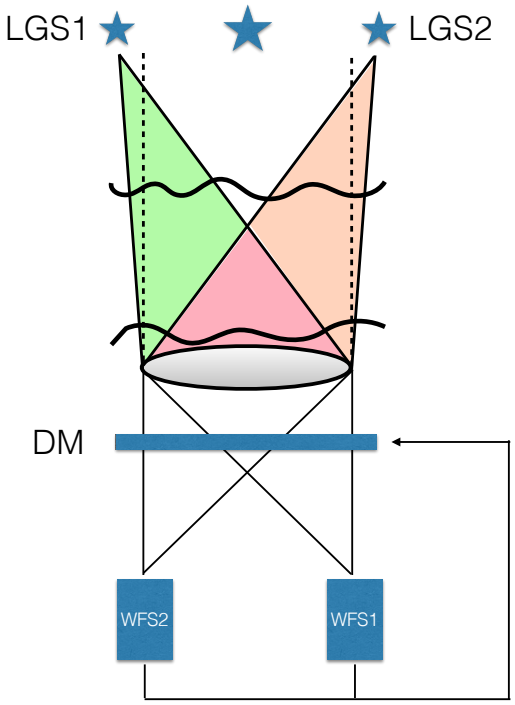

Figure 2.5: An illustration of a LTAO system. Multiple LGSs are used (two in the diagram as an example in one direction), with each one associated with one WFS, forming an asterism around the target science object. By combining the WFS information from the overlapping cones of turbulence probed by the LGSs, the Focal Anisoplanatism is mitigated. The DM is conjugate to the ground, as in most cases.

ections and converting these measurements to DM commands to correct in the direction of one or more science targets. The Focal Anisoplanatism error is then replaced by the tomographic error, which is the error in estimating the 3D volume of turbulence with only a finite number of LGSs. Tallon[64] proposed a zonal tomographic reconstruction method in 1999, and Ragazzoni[65] developed a modal method based on the Zernike polynomials, which has been tested successfully on-sky in 2000[66].

2.2.2.1 Modal tomography

Now we briefly describe the modal tomographic reconstruction method according to Ragazzoni[65]. Fig. 2.6 shows the top view of Fig. 2.5 at a certain height. To be

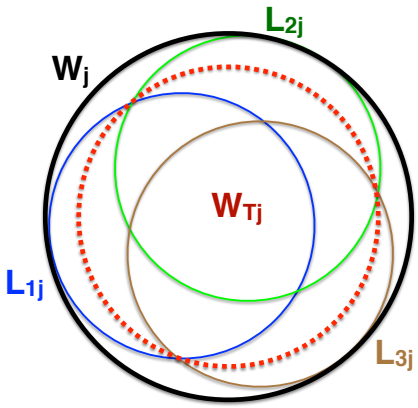

Figure 2.6: LGS footprint and meta-pupil. Three LGSs are shown as an example in this diagram. Here L_{ij} is the footprint of the i-th LGS at j-th layer, and W_j is called the meta-pupil at the j-th layer, meaning a dummy outer circular region encompassing all of the LGSs beams.

general we assume in the following that N different LGSs are projected on the sky and the wavefronts relative to each LGS are sensed through the telescope pupil by N different WFSs (use i as the running index from 1 to N). We also assume that the incoming wavefront is aberrated essentially by M layers of turbulence, located at M different altitudes (using j as the running index from 1 to M). For the i-th LGS, the wavefront can be expanded into a sum of $(N_Z - 3)$ Zernike polynomials as

$$L_i = [a_4, a_5, ..., a_{N_Z}], \tag{2.4}$$

where $\vec{a}$ represents the Zernike coefficients. Note that the first three modes (piston, tip and tilt) are removed due to the uncertainty of the overall LGS position (see section 1.2.4.3). Also we have

$$L_i = \sum_{j=1}^{M} L_{ij}. \tag{2.5}$$

Given the known geometry (the LGS positions and the turbulence layer altitudes) between these circular regions, we can define a set of matrices A_{ij} with size $(N_Z - 3) \times (N_Z - 3)$

$$L_{ij} = A_{ij} W_j. \tag{2.6}$$

Combining equation 2.5 and 2.6, it can be written as

$$\begin{aligned} L_i &= \sum_{j=1}^{M} A_{ij} W_j, \\ \mathbf{L} &= \mathbf{A}\mathbf{W}. \end{aligned} \tag{2.7}$$

The straightforward approach to calculate A_{ij} is to generate individual Zernike modes on a portion of the j-th meta-pupil, *i.e.* L_{ij}, and then to decompose it on the meta-pupil W_j. Thus, matrix $\mathbf{A}$ can be constructed row by row by generating all the Zernike modes. In this fashion, the wavefront expansion W_j from the meta-pupil can be projected onto the on-axis region (the dotted red circle in Fig. 2.6) by the Zernike expansion W_{Tj} with another geometric matrix $\mathbf{T}$ as

$$\begin{aligned} W_{Tj} &= T_j W_j, \\ \mathbf{W}_T &= \mathbf{T}\mathbf{W}. \end{aligned} \tag{2.8}$$

According to equation 2.7 and 2.8, one can easily retrieve the desired wavefront of the on-axis science target with

$$\mathbf{W}_T = \mathbf{T}\mathbf{A}^{+}\mathbf{L}, \tag{2.9}$$

where $\mathbf{L}$ is the WFS measurements with size $N \times (N_Z - 3)$ elements; $\mathbf{T}$ is with size $(N_Z - 3)$ rows and $M \times (N_Z - 3)$ columns; and $\mathbf{A}$ is with size $N \times (N_Z - 3)$ rows and $M \times (N_Z - 3)$ columns. $\mathbf{T}$ and $\mathbf{A}$ are a collection of numerical coefficients derived from the geometry of the LGS system.

For a 4-m telescope, if three LGSs ($N = 3$) with associated LGS constellation shown in Fig. 2.7, and 3 turbulence layers $M = 3$ located at (0, 5 and 10) km with equal strength, and $N_Z = 78$ (*i.e.* 75 Zernike modes are used); then we can get the corresponding geometrical matrix $\mathbf{A}$, $\mathbf{A}^{+}$ and $\mathbf{T}$ (see Fig. 2.8).

2.2.2.2 LTAO performance

From the modal tomographic reconstructor, we can model a LTAO system and reconstruct the wavefront of the on-axis scientific target. To estimate the performance of a simple LTAO system, we have used 3 or 6 LGSs (both Rayleigh

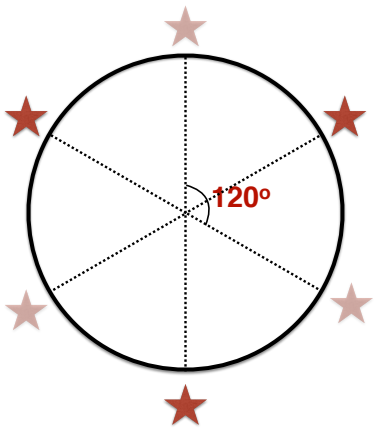

Figure 2.7: LTAO LGS constellation. Either 3 or 6 LGSs are used and the total FOV is 20 arcsec.

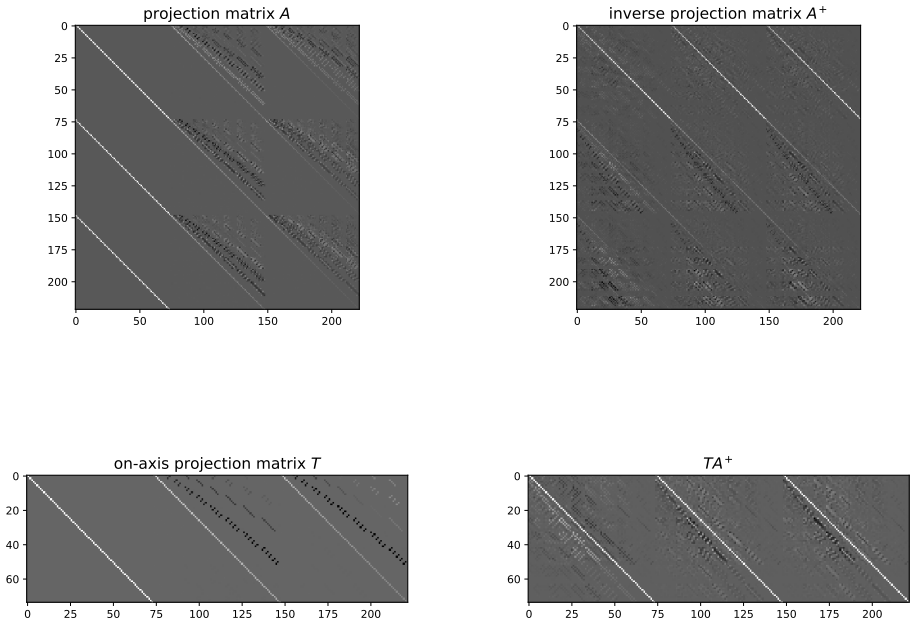

Figure 2.8: Modal tomography geometrical matrix. Singular value decomposition (SVD) is used to compute $\mathbf{A}^{+}$ from $\mathbf{A}$ rejecting singular values smaller than 0.5 to reduce the noise propagation.

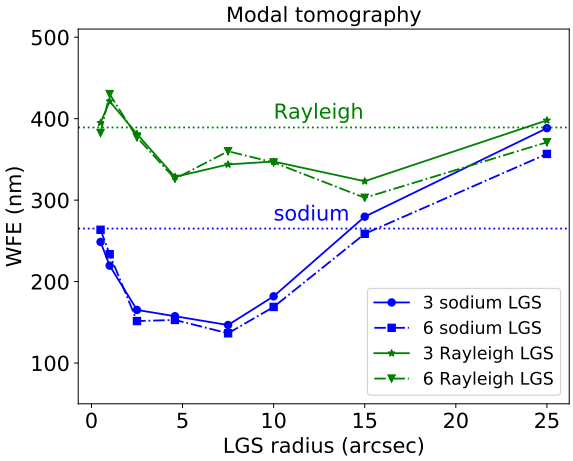

Figure 2.9: LTAO performance for a 4-m telescope. The sodium LGS is at 90 km and the Rayleigh LGS is at 20 km. The dotted horizontal lines represent the wavefront error RMS introduced by the Focal Anisoplanatism, which are obtained by using only one on-axis LGS. Each point on the plots is an average of 50 random turbulence realizations when $r_0 = 0.1$ m at 500 nm.

and sodium). Three turbulence layers are located at 0, 5 and 10 km with equal strength. The LTAO results are shown in Fig. 2.9. It is obvious that sodium LGSs perform better than Rayleigh LGSs, and 6 LGSs slightly outperform 3 LGSs. Also for the sodium LGSs radius between 1 and 15 arcsec, the tomography wavefront error is smaller than that caused by the Focal Anisoplanatism, and the optimal LGS radius is around 7.5 arcsec for sodium LGSs (where all LGSs lie along a circle with slightly bigger diameter than the 4-m telescope) (see Fig. 2.10). For Rayleigh LGSs, we have to push this optimal radius further away (say 15 arcsec) to get better sampling and performance.

2.2.3 Alternatives to LTAO

Apart from LTAO, a number of alternatives have been proposed to eliminate the Focal Anisoplanatism. Baharav *et al.*[67][68] proposed the creation of a periodic fringe pattern in the sodium layer and imaging it with a modified SH WFS. This approach conceptually can reconstruct two-layer turbulence profiles over a wide FOV, while it calls for a high power laser and a single large WFS. Ribak *et al.*[69]

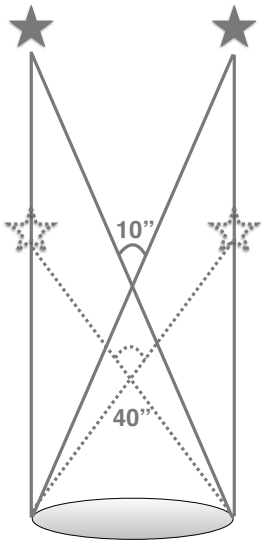

Figure 2.10: Illustration of the optimized FOV for sodium and Rayleigh LGS. The solid star represents sodium LGSs and the dotted stars are the Rayleigh LGSs located at 20 km.

proposed to use stellar scintillation to provide direct instantaneous information about the structure of the atmosphere. The scintillation pattern is created when stellar light is diffracted by high-altitude turbulence. However the measurement is limited by the intensity and the angular size of the reference star, by the height distribution of the atmospheric turbulence, and by the detector resolution and spectral response. Also Ribak[70] proposed an alternative guide star by using radio-created guide stars or fringes. Heating by intense radio beams can either modulate sodium illumination, or create and modify plasma at different altitudes. Fringes between intense radio beams can then create plasma fringes, which are also visible from the telescope. Different from one broad laser beam with large diameter, Lloyd-Hart *et al.*[71] proposed to produce a number of images of different planes in the atmosphere as the laser propagates through a focus. These images are then used in a phase diversity WFS. As an iterative algorithm was required to extract the phase structure from the recorded images, it is not suitable for real-time AO correcting. Kellner *et al.*[72] proposed using Bessel beams as pseudo-inverse guide stars (PIGS).

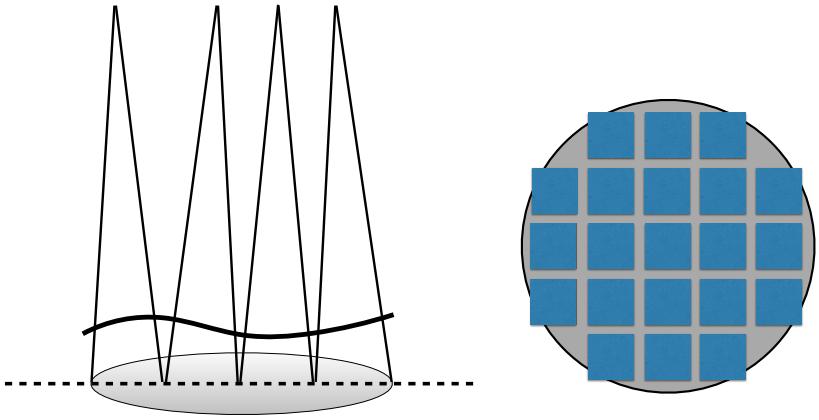

(a) SPLASH scheme

(b) SPLASH Focal Anisoplanatism

Figure 2.11: Concept of SPLASH. The upward paths are followed by the beams. Each beam samples the atmosphere above its own sub-aperture, and each beam is affected separately by Focal Anisoplanatism. In Fig. 2.11b the areas shaded grey are not sensed.

All these above approaches share the common characteristic with the conventional LGS system, that the aberrations are sensed during the return downward path of the laser. A new type of alternative LGS to determine wavefront distortions was proposed. The sensing concept has a number of different possible implementations, but they all share the common principle that the wavefront aberrations are sensed by the upward passage of the beam (see section 2.2.3.1 and 2.2.3.2).

2.2.3.1 Sky Projected Laser Array Shack Hartman

Sky Projected Laser Array Shack Hartman (SPLASH) was first presented by Love *et al.*[73] and further studied by Butterley *et al.*[74]. SPLASH requires the projection of an array of converging laser beams, each of size $\sim r_0$, from the primary mirror of the telescope to form an array of spots on the sky (see Fig. 2.11). The position of each spot on the sky depends on the local (sub-aperture) wavefront gradient. The spots are imaged through the full telescope aperture, so the position

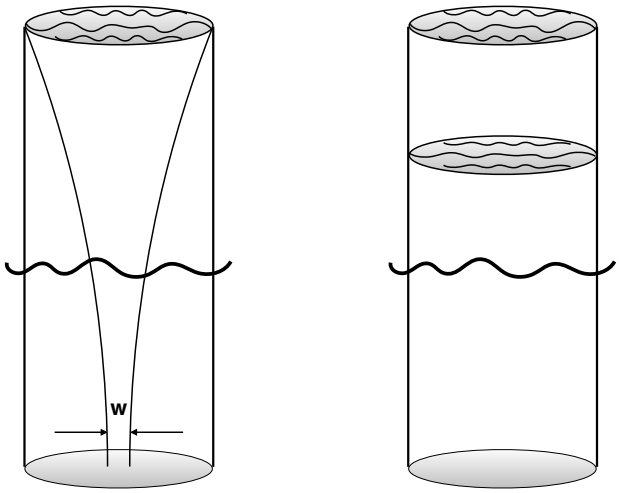

(a) Interferometric PPPP (b) Curvature PPPP

Figure 2.12: Two types of PPPP configurations.

of the final image of each spot will be altered by the global tip/tilt. Hence the position of each spot image gives a measure of the local tip/tilt minus the global tip/tilt – exactly the same quantity as is measured in a conventional SH WFS when used with a LGS. With SPLASH, each sub-aperture is projected onto a smaller square with increasing altitude as a result of Focal Anisoplanatism, but the spacing of the sub-apertures remains the same. So the system will still suffer from some Focal Anisoplanatism as shown in Fig. 2.11b.

2.2.3.2 Projected Pupil Plane Pattern (PPPP)

The PPPP method was proposed by Buscher *et al.*[1]. It senses the distortions produced during the outgoing path by forming an intensity pattern in the atmosphere that is then viewed from the ground. Two possible configurations were suggested by Buscher *et al.*, one was based on interferometric wavefront sensing (Fig. 2.12a) and the other was based on curvature wavefront sensing (see Fig. 2.12b).

For the interferometric PPPP, the laser beam is split into two parts. One part is a broad collimated beam with width equaling the telescope pupil, and the second part is projected as a narrow reference beam of width w. The narrow beam will diffract with a divergence angle of $2\lambda/w$, and when an appropriate value of w is

chosen, the collimated and diverging beams will overlap and be approximately the same diameter, forming interference fringes. At low altitudes the reference beam is narrow and thus is relatively unaffected by turbulence, but turbulence at altitudes above which the reference beam begins to diverge fast will suffer an aberration that is correlated with the aberration in the expanded beam. Thus, this arrangement does suffer from a version of the Focal Anisoplanatism, where the sensitivity to turbulence varies roughly linearly with height. Assume that the telescope diameter $D = 4\,\mathrm{m}$, the laser wavelength $\lambda = 1.06\,\mu\mathrm{m}$, and the propagation altitude $h = 20\,\mathrm{km}$, then the reference beam width w should be

$$\frac{2\lambda}{w}h \approx 4\mathrm{m} \quad \text{or} \quad w \approx 1\mathrm{cm}. \tag{2.10}$$

Due to the broad expansion of such a narrow beam, a large defocus term is formed during the propagation equaling $\pi(x^2 + y^2)/(\lambda h)$ (according to equation 3.7 in section 3.1.1). Thus to prevent the phase wrapping and limit the gap between the phase part of the reference beam after propagation to the range of $[-\pi, \pi]$, we have to guarantee $\Delta r \frac{\partial[\pi r^2/(\lambda h)]}{\partial r} \leq \pi$ (where $r = \sqrt{x^2 + y^2}$) (see section 3.1.1). We know that $\frac{\partial[\pi r^2/(\lambda h)]}{\partial r} = 2\pi r/(\lambda h)$ and the maximum value locates where $r = r_{\max} = D/2$. Thus we have

$$\frac{2\pi D}{2\lambda h} \cdot \Delta r = \frac{2\pi D}{2\lambda h} \cdot \frac{D}{N} = \frac{\pi D^2}{\lambda h N} \leq \pi, \tag{2.11}$$

which means that

$$N \geq \frac{D^2}{\lambda h}, \tag{2.12}$$

therefore 754×754 pixels are required to image the beam profile at 20 km without phase wrapping. However we know that the pupil resolution available is limited by the seeing itself. If $r_0 = 0.1\,\mathrm{m}$ at 500 nm, the maximum resolution equals $h\lambda/r_0 \approx 8.6\,\mathrm{cm}$, which means that the maximum pixel number across is $D/0.086 = 46$, much smaller than 754. On the contrary the curvature PPPP does not require high resolution when re-imaging the on-sky patterns. Thus from now on we only discuss the curvature PPPP and refer to it as simply PPPP.

2.3 PPPP theory

The Projected Pupil Plane Pattern concept is based on the Transport-of-Intensity Equation (TIE). Similar to a curvature WFS, PPPP uses two defocused images at two planes (on one side of focal plane in this case instead of the near and far sides of the focal plane in a curvature WFS). Then the intensity difference between the two images can be inverted to obtain the wavefront distortion with established methods[75].

2.3.1 TIE theory

Under the paraxial (Fresnel) condition, a slowly varying electromagnetic wave $u(r,h) = \sqrt{I(r,h)}\exp(j\phi)$ (where $I(r,h)$ is the intensity, ϕ is the phase and h is the propagation distance) satisfies

$$(2jk\partial_h + \nabla^2)u(r,h) = 0, \tag{2.13}$$

where $\partial_h = \partial/\partial_h$, $k = 2\pi/\lambda$, and $\nabla^2 = \partial_x^2 + \partial_y^2$. Equation 2.13 is equivalent to the following pair of equations[76],

$$k\partial_h I = -\nabla\cdot(I\nabla\phi), \tag{2.14}$$

$$2k\partial_h\phi = -|\nabla\phi|^2 + I^{-1/2}\nabla^2(I^{1/2}). \tag{2.15}$$

Equation 2.14 is the TIE and equation 2.15 is the Transport-of-Wavefront Equation (TWE). From the TIE, one can retrieve the phase from the derivative of the intensity $\partial_h I$.

Similar to a curvature WFS, the TIE can be approximated as[9],

$$k\frac{I_2 - I_1}{h_2 - h_1} = -\nabla\cdot(I_0\nabla\phi) = -\nabla I_0\cdot\nabla\phi - I_0\nabla^2\phi, \tag{2.16}$$

where I_0, I_1 and I_2 are the intensity patterns at the propagation distances 0, h_1 and h_2 correspondingly. Given I_0, I_1 and I_2, we can retrieve the phase ϕ (except

piston) according to equation 2.16. The method we used to reconstruct the phase ϕ is according to Gureyev[75]. For this reconstruction method, it requires that I_0 is slowly changing inside a finite illuminated aperture and smoothly approaching zero on the boundary (equation 3.32). The difference between PPPP and curvature WFS is that curvature WFS measures the curvature of the phase ϕ (corresponding to the second term at the right-hand side of equation 2.16) in the middle of the illuminated area and the gradient of the phase (corresponding to the first term at the right-hand side of equation 2.16) on the edge. While for PPPP both the gradient and the curvature of the phase are measured from the whole defocused images.

The basic concept of PPPP is illustrated in Fig. 2.13. A laser beam is expanded to fill the pupil of the telescope and propagates as a collimated beam upward through the atmosphere. When the laser pulse reaches an altitude of h_1, a snapshot of the Rayleigh backscattered radiation is taken with a camera conjugate at h_1, which will show a disk of illumination corresponding to the projected telescope pupil pattern (*i.e.* I_1). When the laser pulse reaches an altitude of h_2, a second snapshot is taken with a camera conjugate at h_2. With the obtained I_1 and I_2, we can retrieve the turbulence phase ϕ according to equation 2.16. To control the propagation distance, a pulsed laser and a fast shutter are required. Specifically, when the pulsed laser reaches $h_1 - \Delta h_1/2$ and is scattered back, the shutter is opened at time point $2 \times (h_1 - \Delta h_1/2)/c$ (c is the velocity of light, 3×10^8 m/s). When the laser beam continues propagating to $h_1 + \Delta h_1/2$ and is scattered back, the shutter is closed at time point $2 \times (h_1 + \Delta h_1/2)/c$. Δh_1 is the range gate depth for h_1. Similarly for h_2, we open the shutter at $2 \times (h_2 - \Delta h_2/2)/c$ and close it at time point $2 \times (h_2 + \Delta h_2/2)/c$. This shutter is controlled in this manner for each laser pulse. The length of the range gate relates to the scattered flux amount. The larger the range gate is, the more light can be returned. However increasing the range gate means adding images within this range all together. Therefore the combined

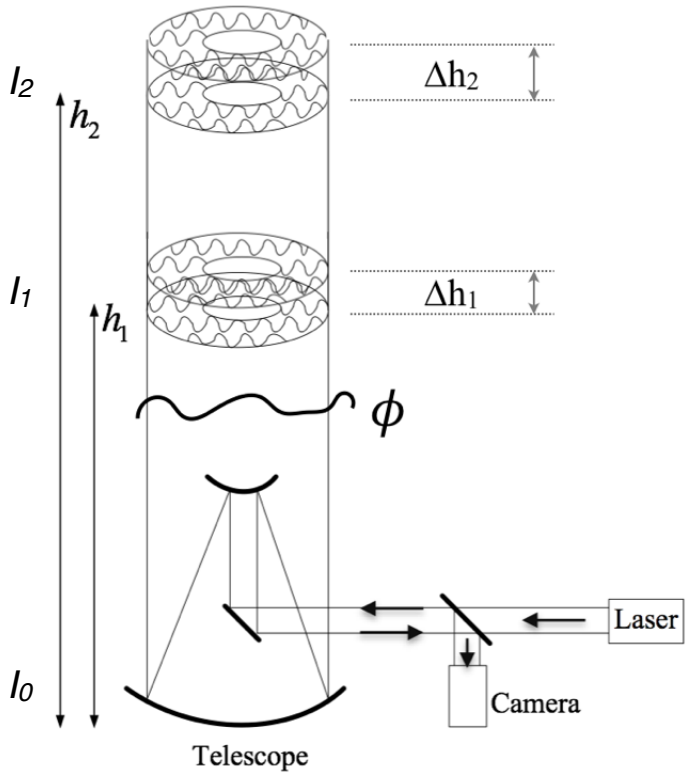

Figure 2.13: A schematic of how PPPP could be implemented. A collimated laser beam is propagated upward into the atmosphere from the whole telescope primary mirror, and encounters aberrations ϕ. Light is backscattered from an altitude, h, is recorded to form I_1 when h is in the range $h_1 \pm \Delta h_1/2$ and similarly I_2 when h is in the range $h_2 \pm \Delta h_2/2$.

image is not only from the center height, which will cause some inaccuracy of the intensity pattern therefore some inaccuracy of the retrieved phase. The maximum Δh has been demonstrated to be approximately 30 km if $r_0 = 0.1$ m (at 500 nm) for a laser beam wavelength equaling 1.06 μm in section 3.2.1, where the PPPP implementation should always meet this condition.

2.3.2 PPPP nonlinear effect

There are nonlinearities due to the approximation of the TIE (equation 2.16), as well as the fact that the wavefront is changing as the wave propagates according to the TWE. Milman[77] and van Dam[78] have provided a detailed analysis of

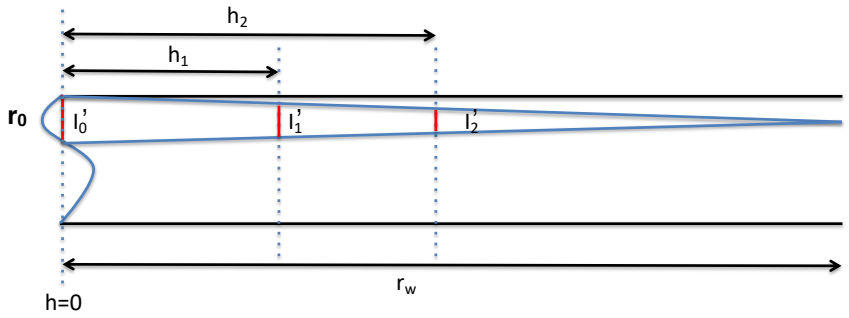

Figure 2.14: Schematic diagram of PPPP nonlinear effect.

the nonlinear effects for a curvature WFS. In this section we will focus on similar effects for PPPP and analyze the conditions under which the nonlinear effect, or high order effect, on PPPP can be neglected.

Let the turbulence wavefront at the ground have local curvature $C_w = 1/r_w$ where r_w is the local radius of curvature of the wavefront over a small area with illumination I'_0 (see Fig. 2.14). As the light propagates to h_1 and h_2, the illumination will become I'_1 and I'_2 and the signal from the equivalent small areas is $I'_2 - I'_1$. The following equations give expressions for I'_1, I'_2 and $I'_2 - I'_1$, which are

$$\begin{aligned} I'_1 \left(\frac{r_w - h_1}{r_w}\right)^2 &= I'_0, \\ I'_2 \left(\frac{r_w - h_2}{r_w}\right)^2 &= I'_0, \\ I'_2 - I'_1 &= I'_0 \left[\left(\frac{r_w}{r_w - h_2}\right)^2 - \left(\frac{r_w}{r_w - h_1}\right)^2\right]. \end{aligned} \tag{2.17}$$

We know that

$$(1-x)^n \approx 1 - nx + \frac{n(n-1)x^2}{2} + \dots \tag{2.18}$$

when x is a small value, similarly

$$\left(\frac{r_w}{r_w - h}\right)^2 = \left(1 - \frac{h}{r_w}\right)^{-2} \approx 1 + 2\left(\frac{h}{r_w}\right) + 3\left(\frac{h}{r_w}\right)^2 + \dots \tag{2.19}$$

when $r_w \gg h$, and this leads us to

$$I'_2 - I'_1 = I'_0 \times \left[2\left(\frac{h_2 - h_1}{r_w}\right) + 3\left(\frac{h_2^2 - h_1^2}{r_w^2}\right) + \dots\right], \tag{2.20}$$

when $r_w \gg h$. The first term in equation 2.20 corresponds to the curvature of the turbulence phase and the others cause the high order modes of the curvature. To limit the high order effect (here only the first and second terms are considered), we have the following criteria

$$3\left(\frac{h_2^2 - h_1^2}{r_w^2}\right) \ll 2\left(\frac{h_2 - h_1}{r_w}\right), \tag{2.21}$$

which can be simplified as

$$r_w \gg 1.5(h_1 + h_2). \tag{2.22}$$

From another point of view, the diffraction effect from I_1' to I_2' will be with size $2\lambda/r_0 \times (h_2 - h_1)$. To require the diffraction effect to be limited inside this area, we should have $2\lambda/r_0 \times (h_2 - h_1) \leq r_0$, which equals

$$(h_2 - h_1) \leq \frac{r_0^2}{2\lambda}. \tag{2.23}$$

Assume $r_0 = 0.1\,\mathrm{m}$ (at 500 nm) and $\lambda = 1.06\,\mu\mathrm{m}$, then $h_2 - h_1$ should be less than or equal to $\sim$30 km km, which should always meet the practical situation.

Equation 2.22 tells us $h_1 + h_2$ should be as small as possible to reduce the nonlinear effect, however the PPPP signal from equation 2.16 shows that $h_2 - h_1$ should be, on the contrary, as big as possible, but within the requirement of equation 2.23. Thus an optimal choice for h_1 and h_2 should be made. Due to the fact that the Rayleigh LGS can only be detected at an altitude where air density is still high, typically below 25 km, and the fact that the atmospheric turbulence between h_1 and h_2 can be only sensed by I_2 (see section 4.2), a good choice would be $h_1 = 10\,\mathrm{km}$ and $h_2 = 20\,\mathrm{km}$.

2.4 Summary

In this chapter we described the Focal Anisoplanatism in detail and listed the solutions to the Focal Anisoplanatism, including "stitching", LTAO and other alternatives. Specifically two types of alternatives are discussed: one is the Sky

Projected Laser Array Shack Hartman (SPLASH) and the other is the emphasis of this thesis, Projected Pupil Plane Pattern. The theory of PPPP is explained in section 2.3.1 and the PPPP nonlinear effect is analyzed in section 2.3.2, where we find that the nonlinear effect is proportional to $h_1 + h_2$, and the propagation distance can not exceed $\approx 30\,\text{km}$. Due to the fact that the Rayleigh LGS can only be detected at an altitude where air density is still high, typically below $25\,\text{km}$, therefore this nonlinear should not be a major problem for PPPP.

Chapter 3

PPPP simulation modeling

Projected Pupil Plane Pattern is a very novel idea and has not been studied except at a conceptual level[1]. Although a similar scheme – curvature WFS – has been successfully tested on sky, PPPP has its unique characteristics which remains unclear without a simulation study. Therefore a full simulation modeling is necessary for understanding the PPPP characteristics.

PPPP simulation can be divided into three steps: firstly to propagate a collimated beam upwards from the telescope pupil plane to several different altitudes (a minimum of two is required) - termed upward propagation; then to reimage the Rayleigh backscattered intensity patterns at those altitudes through the same telescope by cameras conjugate to the corresponding heights - termed return path; finally to retrieve the distorted phase using the subtraction of the images from these cameras - termed reconstruction. The images have to be scaled to the same flux to satisfy the conservation of energy according to equation 2.16.

The major difference between PPPP and conventional LGS wavefront sensing lies in the fact that the required signal for PPPP is generated by the upward propagation of the collimated laser beam. Meanwhile the return path can be treated simply as a reimaging process, *i.e.* a convolution of the atmospheric downward PSF with the backscattered patterns, which may degrade the backscattered intensity patterns depending on the strength of the turbulence. However for conventional LGS SH wavefront sensing, the return path is responsible for producing slope measurement

while the upward propagation of the focused laser beam just introduces undesired LGS distortion.

For a conventional LGS AO system, a NGS is still required for the tip/tilt correction, since the LGS experiences the same turbulence during the upward and downward propagation, therefore it is blind to the atmospheric tip/tilt due to the reciprocity of light travel paths (see section 1.2.4.3). PPPP experiences a similar problem, where the tip/tilt signal generated from the upward propagation (which is a global movement of the intensity pattern) will be canceled out by the return path, therefore it is also necessary to use a NGS to provide the tip/tilt information. Due to this reason from now on we only consider the atmospheric aberrations with tip/tilt removed.

Another unique phenomenon for PPPP is that the telescope primary mirror, which has been used to launch the broad laser beam, is also used to collect the scattered light from the sky, as well as the light from the scientific object. Thus if we use a short-wavelength laser, say 589 nm (typical for sodium LGS), and an infrared scientific camera, the fluorescence from the telescope optics, and any contaminating dust could cause interference for the science instrument[79]. In general, the emitted fluorescence light has a longer wavelength and lower energy than the absorbed light. This phenomenon, known as Stokes shift, is due to energy loss between the time a photon is absorbed and when a new one is emitted. Therefore we have to use a pulsed laser with its wavelength longer than the imaging wavelength such as Nd:YAG at 1.06 μm and limit the science observations to a shorter wavelength. However to obtain diffraction limited images, one needs a residual WFE RMS of about 1/8 times the imaging wavelength or less, which is very challenging for PPPP since the imaging wavelength is restricted to be shorter than the launching laser wavelength. This difficulty applies to all visible AO systems though, and visible AO is of great interest for particular celestial objects and can provide higher resolution diffraction limited images.

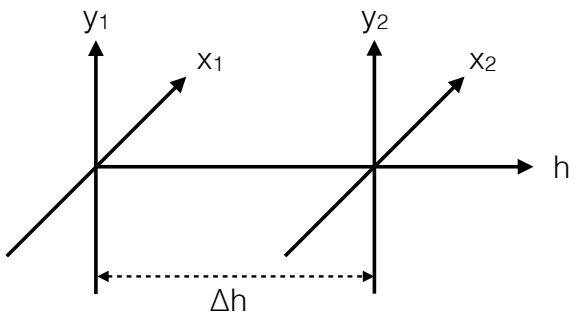

Figure 3.1: Fresnel propagation geometry.

3.1 Upward propagation

The upward propagation simulation includes two main aspects: one is the beam propagation in vacuum; and the other is the simulation of the atmospheric turbulence. Here the beam propagation is performed by a Fresnel diffraction integral, and Monte-Carlo random phase screens are generated to represent the atmospheric turbulence.

3.1.1 Fresnel diffraction

The Fresnel diffraction integral is

$$U(x_2, y_2) = \frac{e^{jk\Delta h}}{j\lambda\Delta h} \int\int_{-\infty}^{\infty} U(x_1, y_1) e^{j\frac{k}{2\Delta h}[(x_2-x_1)^2+(y_2-y_1)^2]} dx_1 dy_1, \tag{3.1}$$

where the source plane optical field is $U(x_1, y_1)$, the observation plane optical field is $U(x_2, y_2)$, and the distance in between is Δh (see Fig. 3.1). k is the wavenumber and λ is the beam wavelength. We want to use the Fresnel diffraction to compute the observation plane optical field from the knowledge of the source plane field.

Equation 3.1 can be rewritten into two forms for numerical evaluation, one of which is

$$\begin{aligned} U(x_2, y_2) =& \frac{e^{jk\Delta h}}{j\lambda\Delta h} e^{j\frac{k}{2\Delta h}(x_2^2+y_2^2)} \\ & \times \int\int_{-\infty}^{\infty} \left[U(x_1, y_1) e^{j\frac{k}{2\Delta h}(x_1^2+y_1^2)} \right] e^{-j\frac{k}{\Delta h}(x_1x_2+y_1y_2)} dx_1 dy_1. \end{aligned} \tag{3.2}$$

In the solution to equation 3.2, two methods of implementing the Fresnel diffraction are used, termed "one-step propagation" and "two-steps propagation"[6][80]. The "one-step propagation" evaluates the Fresnel diffraction integral once as a single Fourier Transform, which is the most straightforward and computational efficient. The "two-steps propagation" gives some flexibility in choosing the grid spacing in the observation plane at the cost of performing a second Fourier Transform.

The second form derived from equation 3.1 is

$$U(x_2, y_2) = U(x_1, y_1) \otimes \left[\frac{e^{jk\Delta h}}{j\lambda\Delta h} e^{j\frac{k}{2\Delta h}(x_1^2+y_1^2)} \right], \tag{3.3}$$

which involves two Fourier Transforms using the convolution theorem. Furthermore, equation 3.3 can also be written in two ways: one using the Transfer Function (equation 3.6) termed "TF" and the other using the impulse response (equation 3.7) termed "IR",

$$U(x_2, y_2) = \mathcal{F}^{-1}\left\{ H(f_{x_1}, f_{y_1}) \times \mathcal{F}[U(x_1, y_1)] \right\}, \tag{3.4}$$

$$U(x_2, y_2) = \mathcal{F}^{-1}\left\{ \mathcal{F}[h(x_1, y_1)] \times \mathcal{F}[U(x_1, y_1)] \right\}, \tag{3.5}$$

where $H(f_{x_1}, f_{y_1})$ is the Transfer Function of free-space propagation and equals

$$H(f_x, f_y) = e^{jk\Delta h} e^{-j\pi\lambda\Delta h(f_x^2+f_y^2)}, \tag{3.6}$$

and $h(x_1, y_1)$ is the Impulse Response of free-space propagation and equals

$$h(x, y) = \frac{e^{jk\Delta h}}{j\lambda\Delta h} e^{j\frac{k}{2\Delta h}(x^2+y^2)}. \tag{3.7}$$

Although all these four methods ("one-step", "two-steps", "TF" and "IR") are equal in theory to evaluate the Fresnel diffraction integral (equation 3.1), there exist differences when different methods are used in terms of different propagation distances in simulation.

According to the Gureyev linear reconstruction[75], I_0 is slowly changing inside a finite illuminated aperture and smoothly approaching zero on the boundary. To

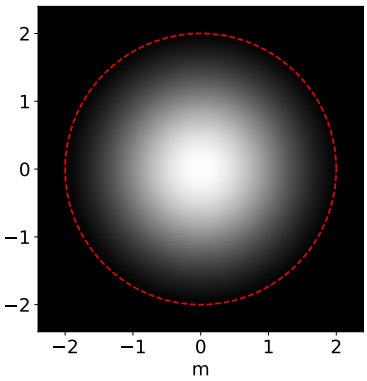

Figure 3.2: Gaussian-like beam I_0. This is for a 4-m telescope (pupil circumference is shown as the red circle).

satisfy this requirement, here we utilize a Gaussian-like laser beam as I_0 (see Fig. 3.2), expressed as

$$I_0 = a + \exp\left[-r^2/(2\sigma^2)\right], \tag{3.8}$$

where $a = -0.1297$ and $\sigma = 1\,\mathrm{m}$. Based on this Gaussian-like I_0, Fig. 3.3 and Fig. 3.4 show the intensity patterns with the propagation distances of 10 and 141 km, using these four different methods respectively with the related simulation parameters listed in Table 3.1. From Fig. 3.3 and Fig. 3.4 we can see that "two-steps" and "TF" show similar intensities at the observation plane, thus we only use "TF" instead of the "two-steps". The "one-step" method is with a fixed grid spacing and there is no control over the spacing in the observation plane, thus we ignore it as well. So only "TF" and "IR" methods are considered from now on. It is worth mentioning that the irregular patterns in Fig. 3.3 are due to the insufficient sampling. If we increase the pixel number to 1024×1024, then we should obtain very similar results as shown in Fig. 3.4.

According to equation 3.6 and equation 3.7, which are involved in "TF" and "IR" propagation methods respectively, there exists a quadratic function inside the exponential term, where the absolute value increases with the square of the frequency (termed chirp function). We can derive the sampling requirement from these chirp functions[80]. Firstly consider the "TF" chirp function, which is the phase of the

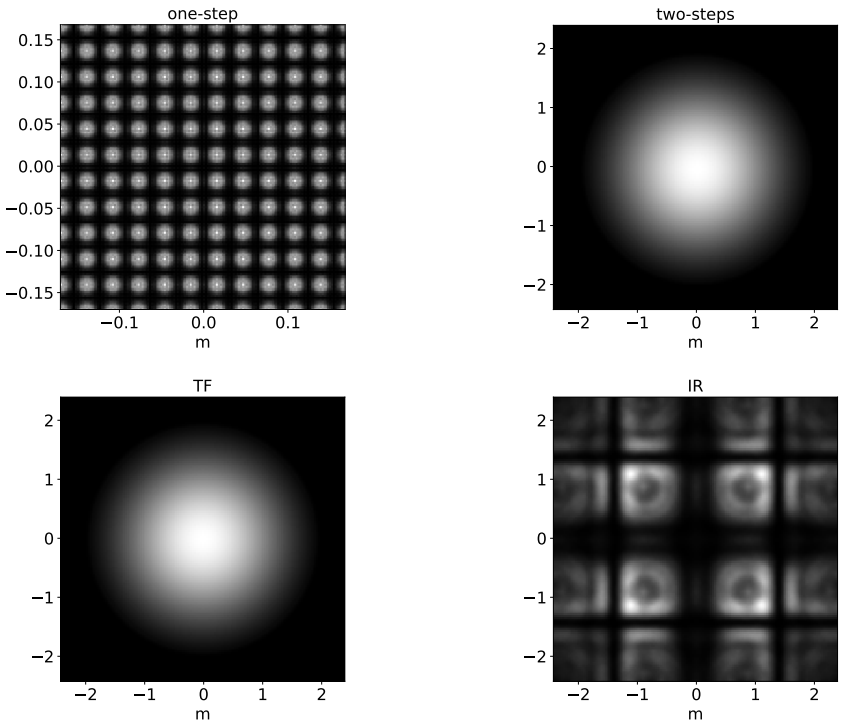

Figure 3.3: Intensities at $h = 10\,\mathrm{km}$ for the Gaussian-like beam. "one-step" and "IR" show irregular patterns as the sampling is insufficient.

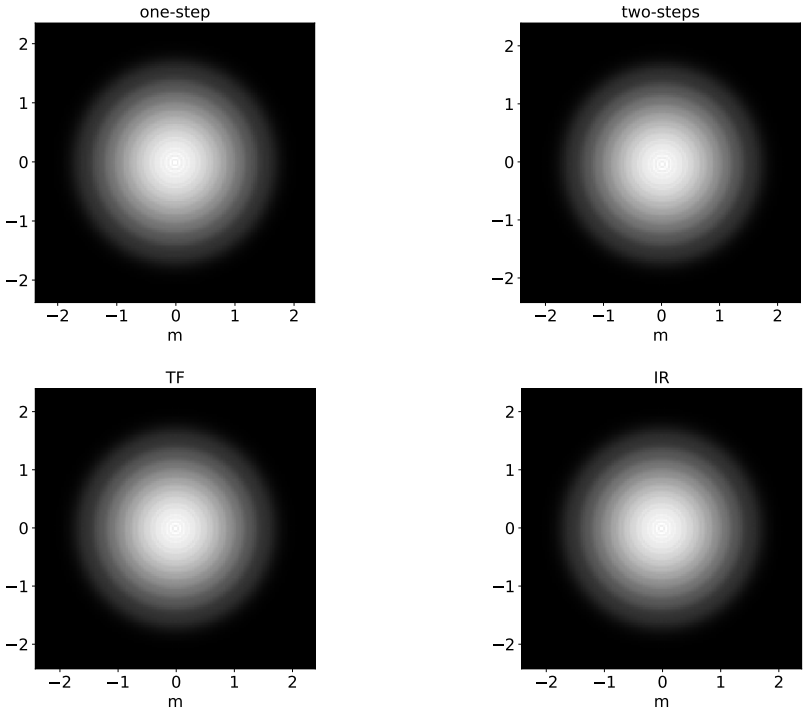

Figure 3.4: Intensities at $h = 141\,\mathrm{km}$ for the Gaussian-like beam.

Transfer Function $\varphi = -\pi\lambda\Delta h(f_x^2 + f_y^2)$ (equation 3.6). For a uniform sampling interval Δf, the criterion for an unambiguous representation of the phase when it is encoded in modulo 2π format, which is the case for a complex exponential term, can be written as $\Delta f|\frac{\partial\varphi}{\partial f}|_{\max} \leq \pi$. This expression states that the maximum change in the absolute phase must be no more than π between any two adjacent samples. If this constraint is violated, then aliased phase values occur. The derivative is found to be $\frac{\partial\varphi}{\partial f} = -2\pi\lambda\Delta h f$ and $|\frac{\partial\varphi}{\partial f}|_{\max} = 2\pi\lambda\Delta h f_{\max}$. We know that $f_{\max} = 1/2d_1$ and $\Delta f = 1/L = 1/(N_{\text{sim}}d_1)$. So the sampling criterion for "TF" is

$$N_{\text{sim}} \leq \frac{L^2}{\lambda\Delta h}, \tag{3.9}$$

or it can be written as a propagation distance requirement

$$\Delta h \leq \frac{L^2}{\lambda N_{\text{sim}}}. \tag{3.10}$$

Similarly the criterion for the "IR" method is $\Delta x|\frac{\partial\varphi}{\partial x}|_{\max} \leq \pi$ (where $\varphi = \frac{\pi}{\lambda\Delta h}(x^2 + y^2)$). The derivative $\frac{\partial\varphi}{\partial x}$ is $\frac{2\pi}{\lambda\Delta h}x$. Again $|\frac{\partial\varphi}{\partial x}|_{\max}$ happens at $x_{\max}$, which is $L/2$. Also we know that $\Delta x = d_1 = L/N_{\text{sim}}$. So the sampling for "IR" is

$$N_{\text{sim}} \geq \frac{L^2}{\lambda\Delta h}, \tag{3.11}$$

or it can be written as propagation distance requirement

$$\Delta h \geq \frac{L^2}{\lambda N_{\text{sim}}}. \tag{3.12}$$

From equation 3.10 and equation 3.12 we know that for a "short" propagation distance the "TF" method is more suitable, while for a "long" distance the "IR" is a better choice. The critical distance is $L^2/(\lambda N_{\text{sim}})$. In our case $L = 4 \times 1.2$, $N_{\text{sim}} = 128 \times 1.2 = 154$ and $\lambda = 1.06\,\mu$m, so $L^2/(\lambda N_{\text{sim}}) = 141\,$km. The propagation distance requirement can be verified by the simulation results shown in Fig. 3.3 and Fig. 3.4. Therefore for PPPP simulation, we choose the "TF" method to evaluate the Fresnel diffraction integral as our propagation distances will be much shorter than 141 km due to an upper limit of Rayleigh scattering (less than 25 km).

Table 3.1: Parameters for upward propagation simulation. D is the telescope diameter, L is the total size of the grid. N_{pupil} is the number of grid points across the pupil and N_{sim} is the number of grid points across L. The grid spacing in the source and observation plane are d_1 and d_2 respectively.

D=4 m	L=4.8 m	λ=1.06 μm
N_{pupil}=128	N_{sim}=154	
d_1=0.031 m	d_2=0.031 m	

Table 3.2: Beam width ($1/e^2$ width) from simulation ("TF" and "IR") and analytical results. Here a Gaussian beam instead of Gaussian-like beam (truncated) is used to be consistent with the analytical result. $N_{\text{pupil}} = 128$. The width of "IR" at $h = 10$ km can not be evaluated as the intensity is not a Gaussian shape due to insufficient sampling (see Fig. 3.3).

	h=10 km	h=141 km
"TF"	1.999 m	2.03 m
"IR"	N.A.	2.03 m
analytical	2 m	2 m

To verify the accuracy of the propagation simulation, we compare the beam width at the observation plane, using "TF" and "IR" methods with the analytical value for propagation distances equaling 10 and 141 km (see Table 3.2). The analytical width $w(h)$ for a Gaussian beam is

$$w(h) = w_0\sqrt{1 + \left(\frac{h}{h_R}\right)^2}, \tag{3.13}$$

where $h_R = \pi w_0^2/\lambda$ and $w_0 = 2$ m. From Table 3.2 it is shown that the simulated beam width (using "TF" and "IR" methods) are consistent with the analytical result.

3.1.2 Phase screen simulation

The refractive index variation of the atmosphere is a random process, and so is the optical path length through it. Consequently turbulence models give statistical averages, such as the Kolmogorov power spectrum of the refractive index variations[2]. The problem of creating an atmospheric turbulence is one of generating individual

realizations of a random process. The typical approximation used within simulations to model the atmospheric turbulence is to use a number of infinitesimally thin phase screens. Here the phase screens are generated using a method derived by Schmidt[6].

The turbulence-induced phase ϕ can be written in a Fourier-integral representation,

$$\phi(x,y) = \int\int_{-\infty}^{\infty} \Psi(f_x, f_y) e^{j2\pi(f_x x + f_y y)} df_x df_y, \tag{3.14}$$

where $\Psi(f_x, f_y)$ is the spatial-frequency-domain representation of the phase. To generate phase screens on a finite grid, equation 3.14 can be rewritten as a Fourier series

$$\phi(x,y) = \sum_{n=-\infty}^{\infty} \sum_{m=-\infty}^{\infty} c_{n,m} e^{j2\pi(f_{x_n} x + f_{y_m} y)}, \tag{3.15}$$

where $c_{n,m}$ are the Fourier-series coefficients, whose variance equals

$$\left\langle |c_{n,m}|^2 \right\rangle = \frac{1}{L^2} \Phi_\phi(f_{x_n}, f_{y_m}), \tag{3.16}$$

here Φ_ϕ is the modified Von Kármán power spectrum

$$\Phi_\phi^{mvK}(f) = 0.023 r_0^{-5/3} \frac{e^{(-f^2/f_m^2)}}{(f^2 + f_0^2)^{11/6}}, \tag{3.17}$$

where $f_m = 5.92/(2\pi l_0)$ and $f_0 = 1/L_0$ (l_0 and L_0 are the inner and outer scales). In simulation a random phase screen is generated as follows. Firstly we generate a Gaussian random number with zero mean and unit variance, then multiply by the square root of Φ_ϕ according to equation 3.17, to produce a random instance of $c_{n,m}$. Then the phase screen $\phi(x,y)$ can be computed by the inverse Fourier Transform of $c_{n,m}$. Unfortunately this method does not produce accurate phase screens in the low spatial frequencies. To compensate for this shortcoming we have adopted the subharmonic method proposed by Lane[81] and detailed description can be found from Schmidt[6]. Specifically after generating a phase screen using the above method already discussed, a low-frequency screen is generated by

$$\phi(x,y) = \sum_{p=1}^{N_p} \sum_{n=-1}^{1} \sum_{m=-1}^{1} c_{n,m} e^{j2\pi(f_{x_n} x, f_{y_m} y)}, \tag{3.18}$$

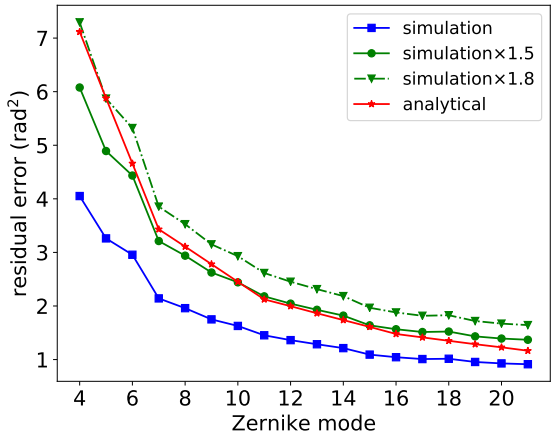

Figure 3.5: Averaged residual error variance of the phase screens when the certain of the lowest Zernike modes are removed. This is an average result from 500 random phase screens for $r_0 = 0.15\,\mathrm{m}$ (at $500\,\mathrm{nm}$).

where the sums over n and m are over discrete frequencies and each value of the index p corresponds to a different grid with the spatial frequency spacing equaling $1/(3^P L)$. In our implementation a 3×3 grid of frequencies $(n, m = -1, 0, 1)$ is used for each value of p and $N_p = 3$ different grids are used.

To verify the statistical characteristics of the generated random phase screens, we calculate the averaged residual variance of the phase screens when certain of the lowest Zernike modes are removed, and compare the results with the analytical values according to Noll[14]. The corresponding results are shown in Fig. 3.5. From Fig. 3.5 it is shown that the trend between the simulation and analytical results are consistent, but with a ($\sim \times 1.5$) when the first 6 or more Zernike modes are removed. But if only the first 4 or 5 modes are removed, then the scaling parameter is $\sim \times 1.8$.

3.1.3 Upward propagation through turbulence

Given the "TF" Fresnel propagation method and the generated random phase screens, we are able to simulate the upward wave optics propagation through turbulence. As shown in Fig. 3.6, there are several turbulence layers (*i.e.* phase

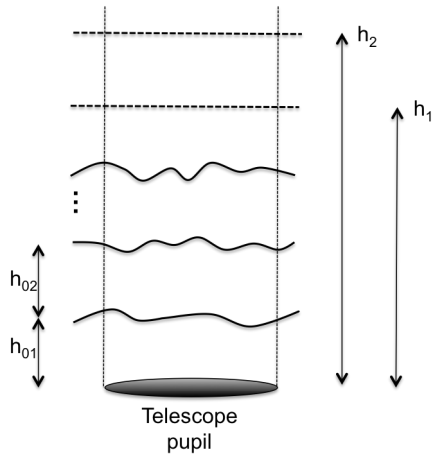

Figure 3.6: Schematic diagram of upward propagation through turbulence.

screens) located at different altitudes. Starting from the pupil plane, we propagate the optical field $U(x, y; h = 0)$ to the distance of the first phase screen h_{01} using the "TF" method, obtaining the optical field at h_{01}. Adding the phase screen ϕ to the optical field at h_{01}, we have $U(x, y; h = h_{01}) \times e^{j\phi}$ as the new source. We then propagate this new source with distance equaling h_{02}. This process is repeated until the beam reaches h_1 and h_2 respectively, we can then obtain the intensity patterns I_1 and I_2 at h_1 and h_2. To be realistic, we use $N_{\text{pupil}} = 128$ and $N_{\text{sim}} = 154$ (propagation distance limit using "TF" method is 141 km in this case). One example with three turbulence layers located at 0, 5 and 10 km with relative C_N^2 strengths 0.5, 0.3 and 0.2 is shown in Fig. 3.7.

3.2 Return path model

The return path simulation is used to reimage the Rayleigh backscattered intensity patterns on sky. Regarding the return path, two issues should be taken into consideration: 1) the amount of flux scattered back (relating to Signal-to-Noise Ratio), which can be calculated by the Light Detection And Ranging (LIDAR) equation[8] given the laser power, telescope diameter, etc.; 2) and the downward

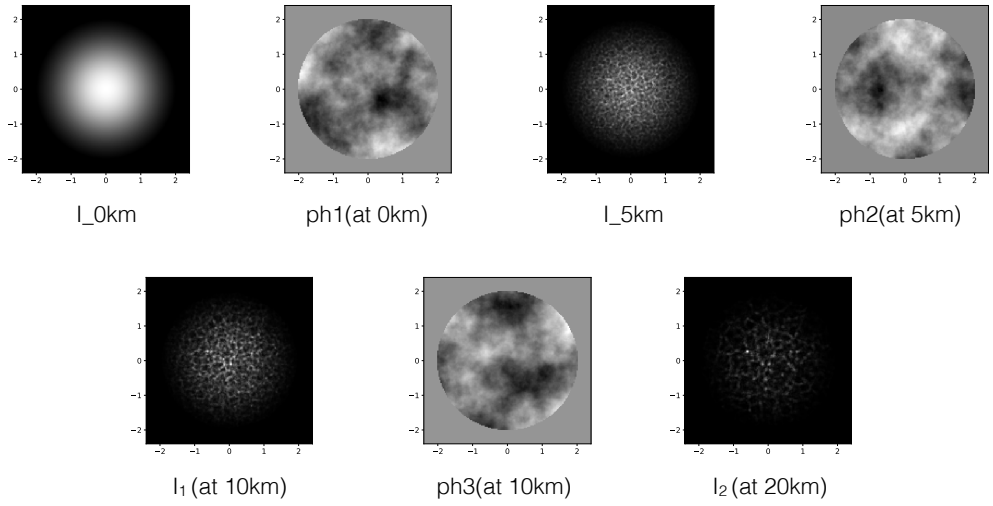

Figure 3.7: One example of upward propagation through turbulence with three phase screens located at 0, 5 and 10 km. "ph" represents phase screen. I_1 and I_2 are intensities at 10 and 20 km.

turbulence-introduced PSF, which is used to convolve with the intensity patterns on sky to perform the reimaging process. During the return path the laser speckle pattern[82], produced by the diffuse reflections of laser light acting on the atmosphere, can be ignored since the time scale of atmospheric molecules moving speed ($\sim$ several ns) is much smaller than the atmosphere coherence time τ_0 ($\sim$ several ms), and the laser speckle will be averaged out.

3.2.1 Calculation of the amount of scattered flux

The amount of backscattered flux can be calculated according to the LIDAR equation[8],

$$N(h) = \left(\frac{E\lambda}{h_P c}\right)(\sigma_B n(h)\Delta h)\left(\frac{A_R}{4\pi h^2}\right)(T_0 T_A^2 \eta), \tag{3.19}$$

where $N(h)$ is the number of photons detected in range Δh; $\sigma_{_B}$ is the effective backscatter cross-section, for Rayleigh scattering which is equal to[8]

$$\sigma_{_B}^{R} = 5.45 \times 10^{-32} \, [550/\lambda(\text{nm})]^4 \quad (\text{m})^2(\text{square radian})^{-1}. \tag{3.20}$$

In equation 3.19, $n(h)$ is the column density of scatters, which is the atmospheric molecules for Rayleigh scatter and sodium atoms for sodium resonance fluorescence. Here Rayleigh scatter is used and the number of atmospheric molecules $n(h)$ is a function of the atmospheric pressure and temperature, satisfying the ideal gas law,

$$PV = \frac{n(h)}{N_A} RT, \tag{3.21}$$

where P and T represent the atmospheric pressure and temperature, which are both determined by the altitude h. V is the volume of the scatters (= 1m^3 here). P can be calculated by

$$P(h) = P_0 e^{-\frac{gMh}{RT_0}}. \tag{3.22}$$

The International Civil Aviation Organization (ICAO) defines an international standard atmosphere (ISA) with a temperature lapse rate of $\sim$6.5 K/km thus T can be approximated as

$$T(h) \approx T_0 - 6.5 \times 10^3 \times h. \tag{3.23}$$

The other parameters to calculate P, T and $n(h)$ in equation 3.21, 3.22 and 3.23 are listed in Table 3.3. The column density of atmospheric molecules with altitudes are shown in Fig. 3.8, from which we know that $n(10\,\text{km}) \approx 1.00 \times 10^{25}$ (m^{-3}) and $n(20\,\text{km}) \approx 3.18 \times 10^{24}$ (m^{-3}).

The other parameters in the LIDAR equation (equation 3.19) are listed in Table 3.4. The amount of flux scattered back with altitudes from 1 to 25 km in the range of 1 km are shown in Fig. 3.9. If $h_1 = 10\,\text{km}$ and $h_2 = 20\,\text{km}$, and Δh_1=1 km and Δh_2=1 km, the numbers of photons detected are 4.24×10^4 and 3.35×10^3 respectively. As the photon noise is introduced mainly by I_2 (see section 4.4.1), we increase Δh_2 from 1 to 5 km. Then the number of photons detected from h_2

Table 3.3: Parameters to calculate the column density of atmospheric molecules $n(h)$.

P_0	sea level standard atmospheric pressure	101325 Pa
g	gravitational acceleration	9.8 m/s^2
M	molar mass of dry air	0.0289 kg/mol
R	universal gas constant	8.31 J/(mol·K)
T_0	sea level standard temperature	288.15 K
N_A	Avogadro constant	6.02×10^{23} per mol

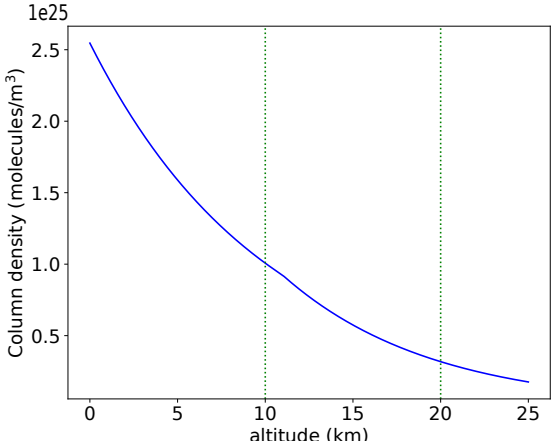

Figure 3.8: The column density of atmospheric molecules with altitudes from 0 to 25 km.

Table 3.4: Parameters in the LIDAR equation. D is the diameter of the telescope primary mirror ($A_R = 12.56\,\mathrm{m}^2$); h_P is Planck's constant; c is the velocity of light; η is the quantum efficiency of photon detector at wavelength λ; T_0 is the transmission of the optical components and T_A is the one-way transmission of the atmosphere; E is the laser energy during the exposure time (2.5 ms), here an average 20 W pulsed laser with 1 KHz frequency is used. Thus the pulse energy is 20W/1KHz = 20mJ. The number of pulses during the exposure time is $\frac{2.5\mathrm{ms}}{1/1\mathrm{KHz}} = 2.5$. Therefore $E = 20\mathrm{mJ} \times 2.5 = 50\mathrm{mJ}$. Δh is the range gate.

D=4 m	$h_P = 6.626 \times 10^{-34}$ Js	$c = 3 \times 10^8$ m/s
η=0.8	T_0=0.5	$T_A \approx 1$
E=0.05 J	Δh=1 km	$\lambda = 1.06\,\mu$m

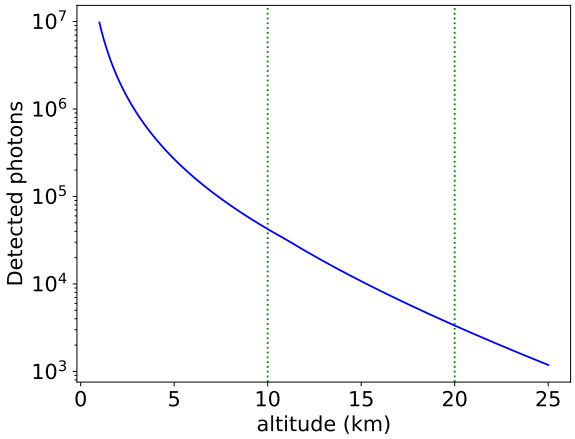

Figure 3.9: The amount of flux detected with altitudes from 1 to 25 km when $\Delta h = 1\,\text{km}$. Assume the FOV of the telescope is adequate for collecting all the light from the scattered plane.

increases to 1.67×10^4. However we can not increase the range gate infinitely as it may cause too much blurring due to the diffraction. If the scale size of the turbulence is r_0, then the diffraction angle is $2\lambda/r_0$ and the blur size is $2\lambda\Delta h/r_0$. It is necessary for this blur to be small compared with this area in the image, which equals to r_0. This requirement leads to the condition

$$\begin{aligned} 2\lambda\Delta h/r_0 \leq r_0 \quad \text{or} \\ \Delta h \leq \frac{r_0^2}{2\lambda}. \end{aligned} \tag{3.24}$$

Assume $r_0 = 0.1\,\text{m}$ at 500 nm and $\lambda = 1.06\mu\text{m}$, then we have $\Delta h \leq 30\,\text{km}$, where the PPPP implementation should always meet this condition.

3.2.2 Downward turbulence introduced PSF

As shown in Fig. 3.10, considering a small part of the pupil d, when the laser propagates upward, it passes through only the corresponding part of the turbulence (shown in red). However when the scattered light comes back, it passes through a much larger part of the turbulence (shown in green). The red and green are poorly correlated except for tip/tilt. The return path then just introduces a general

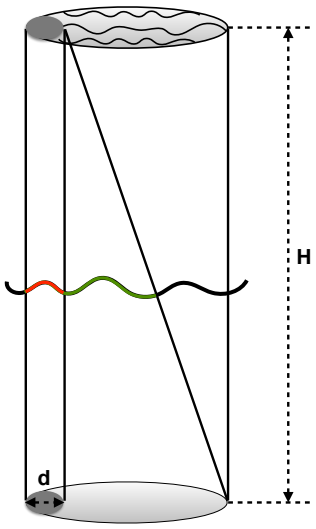

Figure 3.10: Schematic diagram of the upward and downward propagation. The red area of the turbulence affect the upward propagation, while the green area of the turbulence affects the return path.

blurring effect, with a diffraction angle $2\lambda/r_0$. The angle size corresponding to the area of d is d/H. To avoid the blurring effect in the return path, it is necessary for this blur to be small compared with this area in the image. Thus we have $2\lambda/r_0 \leq d/H$, which equals to

$$d \geq \frac{2\lambda H}{r_0}. \tag{3.25}$$

Assume H=20 km, $r_0 = 0.15$ m at 500 nm and $\lambda = 1.06\mu$m, then we know that $d \geq 0.114$ m. That means the images have to be binned with each pixel equaling or larger than 0.114 m. For a 4-m telescope there should be at most $4/0.114 \approx 34$ pixels across the pupil. If $r_0 = 0.08$ m, then the corresponding maximum pixels are 18 pixels.

From another point of view, we can simulate the downward PSF and find out the maximum pixel number to bin the images in order to avoid the blurring effect during the return path in simulation. The PSF of an optical system can be calculated by

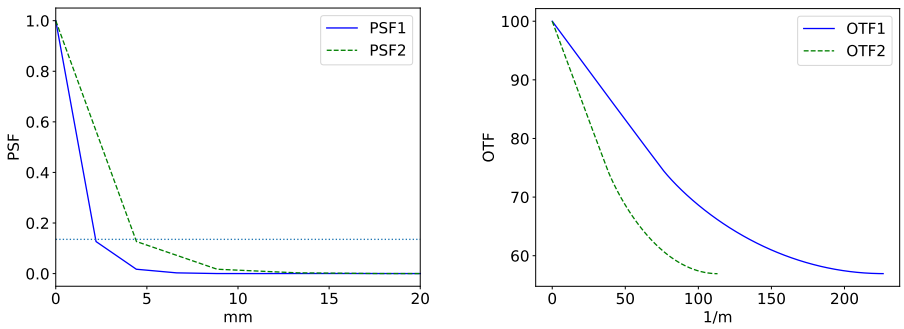

Figure 3.11: The PSFs and OTFs of a 4-m telescope pupil for $h_1 = 10\,\text{km}$ and $h_2 = 20\,\text{km}$ projected to sky. The horizontal dotted line in the left plot represents $1/e^2$ width. PSF1 and OTF1 are calculated from h_1 while PSF2 and OTF2 are calculated from h_2. The simulation wavelength is $1.06\,\mu\text{m}$ and 154×154 grids (128×128 for the pupil) are used.

the scaled Fourier transform of the pupil $P(x, y)$ according to[83]

$$\text{PSF} = |\mathcal{F}[P(\lambda h f_x, \lambda h f_y)]|^2. \tag{3.26}$$

The pupil function $P(x, y)$ here is a circle with 4-m diameter. The corresponding PSFs and OTFs (the Fourier transform of the PSF) for $h_1 = 10\,\text{km}$ and $h_2 = 20\,\text{km}$ are shown in Fig. 3.11.

If there exist atmospheric aberrations, we assume the turbulence ϕ is on the ground (in this way the atmospheric turbulence has the most severe effect on the reimaging process, see Fig. 3.10) and the pupil function is replaced by the general pupil function including the phase term, which is $P'(x, y) = P(x, y) \exp(j\phi)$. Here the turbulence phase ϕ is the same as the one used during the upward propagation. Fig. 3.12 shows the averaged return-path PSFs for h_1 and h_2 projected to the sky for different r_0.

To reduce the effect of the atmospheric PSF on the PPPP on-sky signal $I_2 - I_1$, we have to limit the PSF width ($1/e^2$ width here) to one pixel or less. From Fig. 3.12 the width of PSF2 is nearly twice that of PSF1, which means the intensity pattern at h_2 is more blurred than h_1 during the return path. Considering the worst case, *i.e.* PSF2, the PSF2 width for $r_0 = 0.15\,\text{m}$ (at $500\,\text{nm}$) is approxim-

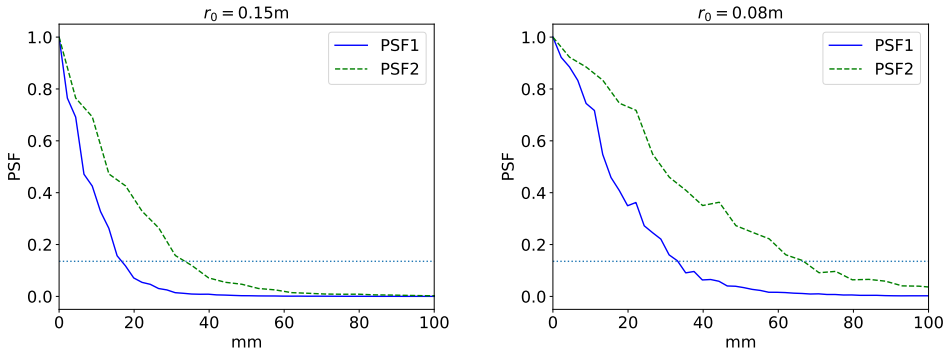

Figure 3.12: Return-path turbulence-introduced averaged short-exposure PSF projected to sky from 100 random phase screens with different r_0 (defined at 500 nm). The dotted line represents $1/e^2$ width.

ately $0.035 \times 2 = 0.07$ m. If the PSF is one pixel or less, then the required pixel number should be at most $D/0.07 = 57$ pixels for a 4-m telescope. If the telescope primary mirror D is doubled, then the maximum pixel number can be doubled as well. For $r_0 = 0.08$ m, the maximum N is 28 pixels. These numbers are larger than the previous analysis maybe because the width used here is $1/e^2$ width instead of the full width.

3.3 Reconstruction

Two reconstruction methods are used for PPPP, one is a linear method based on the Zernike polynomials and matrix operation; the other is a nonlinear method using Artificial Neural Network (ANN). The linear reconstruction has been demonstrated to be an effective one but only for a high SNR[84], whereas the nonlinear one is very useful for a noisy situation and has the potential to advance PPPP technique to practical usage. In this section we describe both methods, and their reconstruction results will be shown in chapter 4.

3.3.1 Linear reconstruction

The linear reconstruction is according to the Gureyev[75] method. This method is based on the decomposition of the TIE (equation 2.16) into a series of Zernike polynomials. From an explicit matrix formula, the Zernike coefficients of the phase can be expressed as functions of the intensity difference at two distances. Firstly let us calculate the scalar product of equation 2.16 with Zernike polynomials. The scalar product of the left-hand side equals

$$\left\langle k\frac{I_2 - I_1}{h_2 - h_1}, Z_j \right\rangle = R^{-2}\int_0^{2\pi}\int_0^R k\frac{I_2 - I_1}{h_2 - h_1} Z_j r dr d\theta, \tag{3.27}$$

where Z_j is the j-th Zernike polynomial, R is the radius of the telescope primary mirror. We define $F_j = \langle k(I_2 - I_1)/(h_2 - h_1), Z_j\rangle$. On the other hand, the scalar product of the right-hand side of equation 2.16 is

$$\langle -\nabla\cdot(I_0\nabla\phi), Z_j\rangle = R^{-2}\int_0^{2\pi}\int_0^R -\nabla\cdot(I_0\nabla\phi) Z_j r dr d\theta. \tag{3.28}$$

If we decompose the turbulence phase ϕ into Zernike polynomials, then

$$\phi = \sum_{i=4}^{N_Z} a_i Z_i, \tag{3.29}$$

where a_i is the coefficient of the i-th Zernike polynomial and N_Z is the highest order of Zernike terms used. Note that the tip/tilt modes are removed. Substituting equation 3.29 into equation 3.28 we get

$$\begin{aligned}&\langle -\nabla\cdot(I_0\nabla\phi), Z_j\rangle = \\ &\quad \sum_{i=4}^{N_Z} a_i R^{-2}\int_0^{2\pi}\int_0^R -\nabla\cdot(I_0\nabla Z_i) Z_j r dr d\theta.\end{aligned} \tag{3.30}$$

Using integration by parts, $\int u dv = uv - \int v du$, equation 3.30 can be written as

$$\begin{aligned}&\langle -\nabla\cdot(I_0\nabla\phi), Z_j\rangle = \\ &\quad \sum_{i=4}^{N_Z} a_i R^{-2}\int_0^{2\pi}\int_0^R I_0\nabla Z_i\cdot\nabla Z_j r dr d\theta,\end{aligned} \tag{3.31}$$

on the condition that the intensity distribution I_0 satisfies

$$\begin{aligned}I_0 > 0 \qquad &\text{inside the 4-m circle } \Omega,\\ I_0 = 0 \qquad &\text{outside } \Omega \text{ and on the boundary } \Gamma,\end{aligned} \tag{3.32}$$

Table 3.5: **M** for Gaussian-like beam I_0 from 4th to 10th Zernike modes. I_0 has been normalized to 1, *i.e.* the sum of I_0 over all pixels is 1.

				j			
i	4	5	6	7	8	9	10
4	13.27	0	0	0	0	0	0
5	0	6.64	0	0	0	0	0
6	0	0	6.64	0	0	0	0
7	0	0	0	23.68	0	-0.0003	0
8	0	0	0	0	23.68	0	0.0003
9	0	0	0	-0.0003	0	8.95	0
10	0	0	0	0	0.0003	0	8.95

thus the integral over the boundary Γ disappears. This is why we use the Gaussian-like beam as I_0 (see Fig. 3.2). Now it is convenient to introduce the matrix **M** with elements

$$M_{ij} = \int_0^{2\pi} \int_0^R I_0 \nabla Z_i \cdot \nabla Z_j r dr d\theta. \tag{3.33}$$

Using this definition we can rewrite equation 3.27, 3.31 and 3.33 as a system of algebraic equations for the unknown Zernike coefficients

$$R^2 F_j = \sum_{i=4}^{N_Z} M_{ij} a_i \qquad \text{or} \qquad R^2 \vec{F} = \mathbf{M}\vec{a}. \tag{3.34}$$

Finally to retrieve the phase ϕ, we simply need to find the Zernike coefficients $\vec{a}$, which equals

$$\vec{a} = R^2 \mathbf{M}^{-1} \vec{F}. \tag{3.35}$$

Equation 3.35 is the final expression of this linear reconstruction. $\vec{F}$ is based on the measured signal and the matrix **M** can be theoretically calculated given the intensity distribution at the pupil I_0. Using a Gaussian-like beam I_0 as in equation 3.8 we have the corresponding **M** and $\mathbf{M}^{-1}$ shown in Table 3.5 and Table 3.6. If a uniform intensity distribution inside the circular aperture like a top-hat beam is used as I_0, the corresponding **M** and $\mathbf{M}^{-1}$ are shown in Table 3.7 and Table 3.8. These tables only present **M** and $\mathbf{M}^{-1}$ from 4th to 10th Zernike modes. Similar matrices generated from $N_Z = 78$ are shown in Fig. 3.13 and Fig. 3.14.

Table 3.6: $\mathbf{M}^{-1}$ for Gaussian-like beam I_0.

				j			
i	4	5	6	7	8	9	10
4	0.075	0	0	0	0	0	0
5	0	0.151	0	0	0	0	0
6	0	0	0.151	0	0	0	0
7	0	0	0	0.042	0	≈0	0
8	0	0	0	0	0.042	0	≈0
9	0	0	0	≈0	0	0.112	0
10	0	0	0	0	≈0	0	0.112

Table 3.7: $\mathbf{M}$ for top-hat beam I_0 from 4th to 10th Zernike modes. I_0 has been normalized to 1, *i.e.* the sum of I_0 over all pixels is 1.

				j			
i	4	5	6	7	8	9	10
4	24.28	0	0	0	0	0	0
5	0	12.14	0	0	0	0	0
6	0	0	12.14	0	0	0	0
7	0	0	0	57.69	0	-0.027	0
8	0	0	0	0	57.69	0	0.027
9	0	0	0	-0.027	0	24.56	0
10	0	0	0	0	0.027	0	24.56

Table 3.8: $\mathbf{M}^{-1}$ for top-hat beam I_0.

				j			
i	4	5	6	7	8	9	10
4	0.041	0	0	0	0	0	0
5	0	0.082	0	0	0	0	0
6	0	0	0.082	0	0	0	0
7	0	0	0	0.017	0	≈0	0
8	0	0	0	0	0.017	0	≈0
9	0	0	0	≈0	0	0.041	0
10	0	0	0	0	≈0	0	0.041

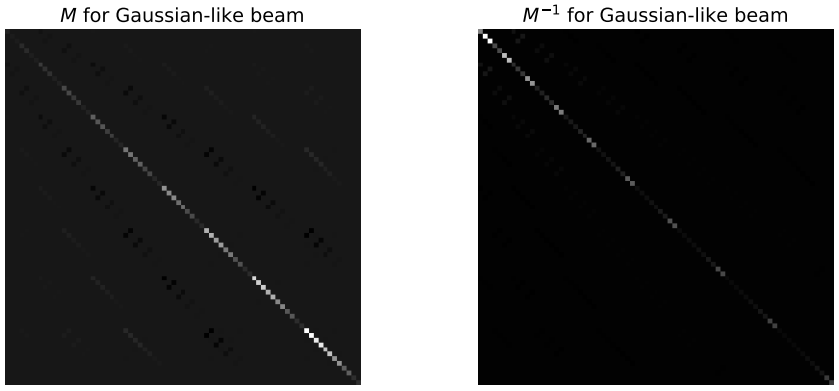

Figure 3.13: $\mathbf{M}$ and $\mathbf{M}^{-1}$ for Gaussian-like beam from 4th to 78th Zernike modes.

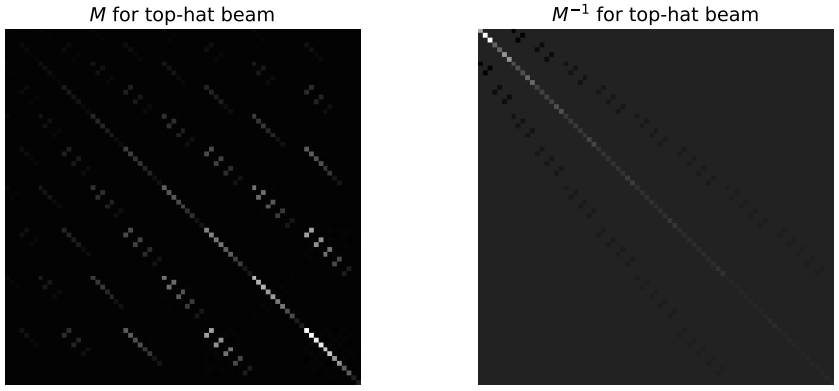

Figure 3.14: $\mathbf{M}$ and $\mathbf{M}^{-1}$ for top-hat beam from 4th to 78th Zernike modes.

3.3.2 An example of PPPP linear reconstruction

Fig. 3.15 shows an example of a complete PPPP simulation process for a 4-m telescope. The laser beam (Gaussian-like beam as shown in Fig. 3.2) propagates from the pupil to h_1 and h_2 according to section 3.1 through a random phase screen (with tip/tilt removed and assuming the phase screen is on the ground). Then I_1 and I_2 on sky are formed. I_1 and I_2 on sky are then convolved with the atmosphere downward PSF1 and PSF2 respectively generated by the same phase screen, forming I_1 and I_2 on ground. Comparing I_1 and I_2 on ground with I_1 and

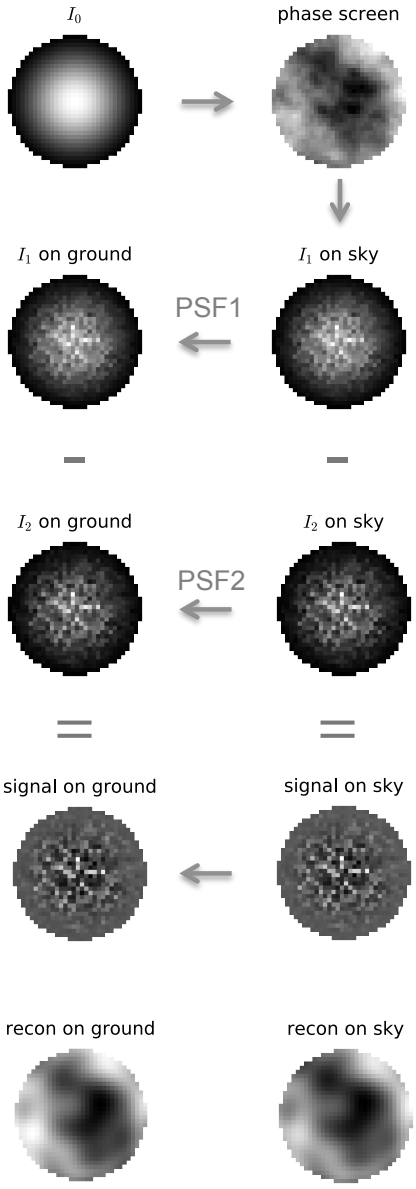

Figure 3.15: An example of PPPP simulation process, including upward propagation, return path and reconstruction. The Gaussian-like beam at the pupil propagates to h_1 and h_2 through a phase screen on the ground, forming I_1 and I_2 on sky. Convolving I_1 and I_2 on sky with the downward PSF we get I_1 and I_2 on ground. The signal is $I_2 - I_1$ for both on sky and on ground, from which the reconstructed phases can be obtained using the linear reconstruction.

I_2 on sky, we find that they are very alike. That is because only 32×32 pixels are used to sample the images and the downward turbulence-introduced PSFs are limited inside one pixel, which therefore has very little effect on the PPPP signal (see section 3.2.2). It is worth mentioning that I_1 and I_2 have been normalized to the same flux amount (here normalized to the total amount of photons scattered back from h_2 for convenience). Applying the linear reconstruction method, we get the reconstructed phases (the last row in Fig. 3.15), which show great similarity to the input phase screen albeit at a lower resolution.

3.3.3 Nonlinear reconstruction

Artificial Neural Networks (ANN) are machine learning-based algorithms which have the ability to learn from different examples and extrapolate that knowledge to unseen data. They were traditionally inspired by human neurons[85], but have been developed to form the Deep Learning models widely used today[86]. ANNs have been used with AO successfully on-sky, including recently to produce a tomographic reconstructor operating with multiple WFSs using an asterism of guide stars as described by Osborn *et al.*[38]. However, each potential asterism demands a different ANN algorithm which in turns leads to a set of time-consuming training processes. In contrast, applying the ANN methodology for PPPP has the advantage that the laser beam is under control and so can be fixed: once trained an ANN-based reconstructor needs not necessarily be retrained when changing the telescope pointing direction. The ANN architecture is built by our collaborators Carlos Gonzalez Gutierrez and F. J. de Cos Juez from University of Oviedo, Spain. The training datasets are provided by the author of this thesis, as well as integrating the nonlinear reconstructor into the AO simulation.

ANN is composed of several layers of neurons, connected to each other in a feed-forward fashion. All the connections between neurons are called weights. A key stage in obtaining an usable ANN is the learning, or training, process. By us-

ing a dataset of known inputs and associated outputs, it is possible to calculate optimal values for the weights. Initially, the weights are random and an input is propagated through the network. The output of the ANN is computed and compared with the expected output, which results in a residual error. This error is back-propagated[87] through the network and the weights are updated accordingly. After iterating through all sets of the training data, one epoch is finished. Training is ended after a certain number of epochs when some suitable criterion to evaluate the network has been met.

As a sub-type of ANNs, Convolutional Neural Network (CNN) is characterized by the appearance of convolutional layers, which help in the extraction of features from an image. These layers are composed of several filters that are convolved with the input image, therefore generating a new set of processed images. The CNN architecture has been demonstrated as particularly advantageous for image processing, and since for PPPP the input are two images, I_1 and I_2, it is appropriate to be used in this work and is referred to as Neural Network (NN) in the following.

3.3.3.1 NN implementation for PPPP

3.3.3.1.1 NN Parameters For PPPP, if we describe a NN as a "black box" nonlinear reconstructor, as shown in Fig. 3.16, then its inputs are two images of the scattered intensity patterns from two different altitudes, *i.e.* I_1 and I_2. The expected output is a vector of 74 Zernike coefficients (from 4th to 78th Zernike polynomials) representing the reconstructed wavefront.

3.3.3.1.2 Training dataset During the training process it is necessary to expose the NN to a large number of pairs of inputs and desired outputs. This training dataset should cover the full range of possible scenarios, and previous experiments in atmospheric wavefront reconstruction show that a NN can accurately predict an output when trained with a superposition of independent training sets[38]. The

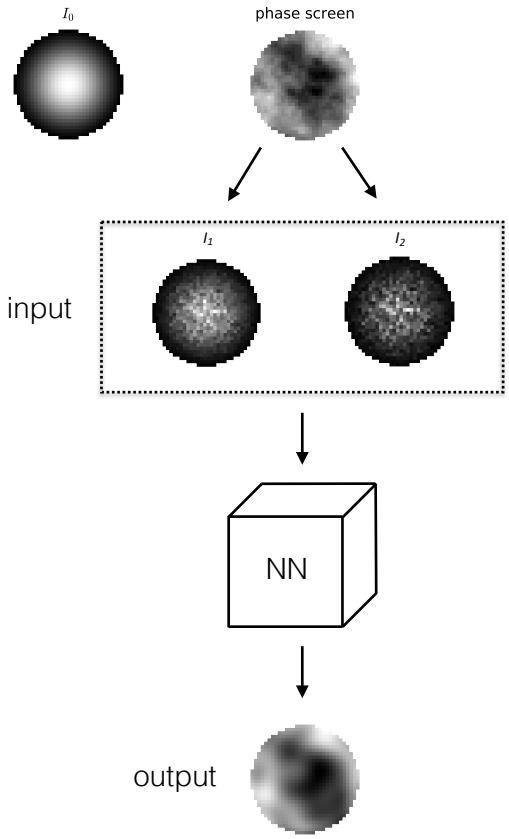

Figure 3.16: Schematic diagram of the PPPP signal and NN reconstructor as a black box. A Gaussian-like beam at the pupil I_0 propagates through a random phase screen to h_1 and h_2, forming images I_1 and I_2 respectively. The input for NN reconstructor then is the two images I_1 and I_2 and the output is the reconstructed 74 Zernike coefficients (here shown as the reconstructed phase for convenience).

conclusion is that not every possible turbulent profile is required but instead a basis set is sufficient for training. Such as basis set for PPPP is now described.

Table 3.9 shows the parameters used to generate the training dataset from the PPPP simulation model. The tip/tilt modes are excluded from both input phase screens and reconstructed Zernike coefficients. The parameters are chosen to balance the PPPP performance and complexity. Four sets of training data were created, each with a constant laser power: 10, 20, 200 W and infinite power (photon noise free). For each power simulated, 100 altitudes for one turbulence layer, h, distributed between 0 and 10 km are defined, with 10 values of r_0 between 0.08 m

Table 3.9: PPPP parameters for training dataset. The number of pixels across the selected square to pad the pupil is N_{sim} to reduce edge effects during propagation, and N_{pupil} is the number of illuminated pixels across the pupil. The transmission of the optical components is T_0, and T_A is the one-way transmission of the atmosphere. The range gate is Δh_1 and Δh_2 for h_1 and h_2 respectively. E is the average laser power and η is the quantum efficiency of photon detector.

simulation	turbulence
D=4 m	one turbulence layer
h_1=10 km	altitude: 0 to 10 km
h_2=20 km	r_0: 0.08 to 0.28 m (at 500nm)
N_{sim}=64	T_0=0.5; T_A=1
Gaussian-like beam I_0	L_0=100 m; l_0=0.01 m
74 Zernike modes (4th to 78th)	
laser	**camera**
λ=1.06 μm	N_{pupil}=54
Δh_1=1 km; Δh_2=5 km	η=0.8
E (W): 10, 20, 200 & infinite	read noise: $3e^-$
laser frequency: 1 KHz	exposure time: 2.5 ms

and 0.28 m per turbulence layer altitude and 300 random turbulence realizations for each r_0 value. Thus for each turbulence altitude, there would be 3000 pairs of input images for training. This leads to 300,000 training data for each laser power including 100 turbulence layer altitudes, with each one created from a well-defined r_0 and h value: this is the basis set. These data can be used to train four different Neural Network, each for a specific laser power, or used together to train one combined Neural Network which is laser power agnostic.

3.4 Summary

In this chapter we described the PPPP simulation modeling in detail including three key steps: upward propagation, return path model and reconstruction. The upward propagation simulation is performed by a Fresnel diffraction together with random phase screen simulations as the atmospheric turbulence. How to calculate the scattered photons and the downward PSF during the return path is modelled in section 3.2, from where we know that the effect of the blurring due to the return path can be neglected if the images are binned to a certain size. Two reconstruction

methods are introduced, one is the linear reconstruction and one is based on the Artificial Neural Network. Detailed simulation results will be presented in chapter 4 based on the simulation model described in this chapter.

Chapter 4

Simulation results and performance analysis

Using the simulation models built in chapter 3, in this chapter we show the Monte-Carlo simulation results, where the PPPP performance is estimated by the residual Wavefront Error RMS between the input turbulence realizations and the reconstructed phases. First, we analyze the PPPP performance given different PPPP parameters and determine suitable choices for the pixel number of sampling the backscattered images, the number of Zernike modes for reconstruction, two backscatter altitudes h_1 and h_2, etc. Secondly, we investigate the effect of different r_0 and turbulence layer altitudes. Thirdly, we provide analysis regarding the PPPP sensitivity and dynamic range, and the SNR analysis as well as the attempts to increase the SNR. Finally, we compare PPPP performance with a SH WFS from a full Adaptive Optics simulation platform, *Soapy* (which is a Monte-Carlo Adaptive Optics simulation platform written by Andrew Reeves[88]), with the PPPP simulation model integrated. These simulation results from *Soapy* include results from both the linear and Neural Network reconstructor. The Neural Network architecture is built by our collaborators Carlos Gonzalez Gutierrez and F. J. de Cos Juez from University of Oviedo, Spain. The training datasets are provided by the author of this thesis, as well as integrating the nonlinear reconstructor into the AO

simulation, *Soapy*.

4.1 PPPP parameters optimization

4.1.1 Investigation of the number of pixels and Zernike modes

Two key parameters for PPPP are the number of pixel N across the pupil to image the backscattered intensity patterns, and the highest order of Zernike modes N_Z for reconstruction (here the linear reconstruction is used). Fig. 4.1 shows the residual WFE RMS between the input phase screen and the reconstructed phase, and the RMS of the input phase screen (with tip/tilt removed) for reference. From Fig. 4.1, we find that the residual WFE shares a similar tendency when N changes from 16 to 256, where the WFE declines from 21 to 78 Zernike modes, followed by a slower decrease from 78 to 300 Zernike modes. The relatively poor performance for $N = 16$ is caused by the poor sampling of the two images. According to Fig. 4.1, it indicates an optimal choice for $N = 64$ and $N_Z = 78$ (the highest order of Zernike mode). However due to the return path blurring effect (see section 3.2.2), we have to limit $N \leq 57$ when $r_0 = 0.15\,\mathrm{m}$ at $500\,\mathrm{nm}$ (and $N \leq 28$ when $r_0 = 0.08\,\mathrm{m}$), thus we choose $N = 32$ pixels in the following.

4.1.2 Investigation of h_1 and h_2

The propagation altitudes of the backscattered images h_1 and h_2 are another key parameter for PPPP. In particular the subtraction and the sum of h_1 and h_2 are of great importance. The subtraction $h_2 - h_1$ is proportional to the PPPP signal according to equation 2.16. Thus we should make $h_2 - h_1$ as big as possible in theory to increase PPPP signal. However, a large propagation distance will increase the nonlinear effect (see section 2.3.2). Fig. 4.2 shows the residual WFE when we keep

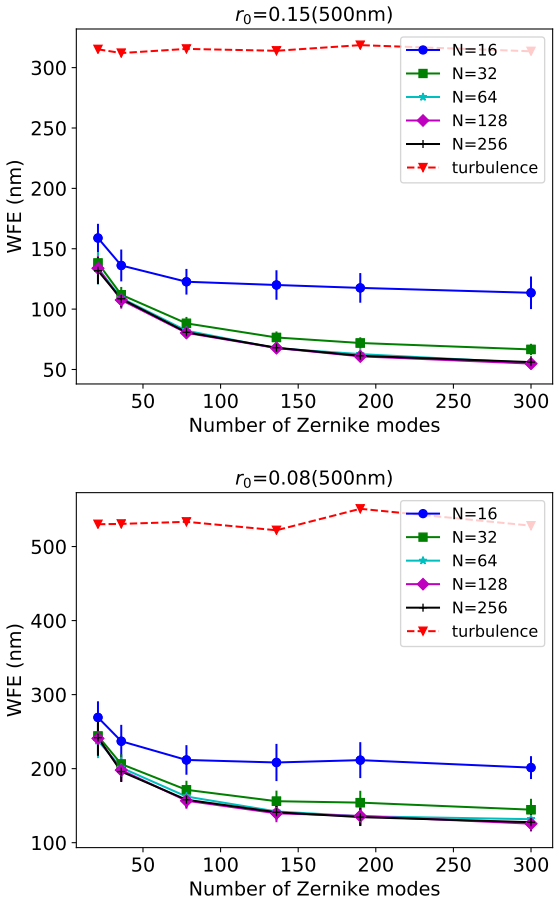

Figure 4.1: Investigation of the number of pixels N and the highest order of Zernike modes N_Z. The turbulence WFE represents the RMS of the input phase screen (around 350 nm when $r_0 = 0.15$ m and 530 nm when $r_0 = 0.08$ m). Each point is an average of 50 random phase screens. $h_1 = 10$ km and $h_2 = 20$ km are used here.

$h_1 = 10$ km and increase h_2 up to 60 km. We find that the residual WFE remains almost unchanged until $h_2 - h_1 \geq 10$ km for both $r_0 = 0.15$ and $r_0 = 0.08$ m. It indicates that, as long as $h_2 - h_1 > 0.1$ m, the PPPP signal is large enough in this noise-free situation. But if $h_2 - h_1 > 10$ km, the nonlinear effect will degrade the PPPP performance. Comparing the result of $N = 64$ with that of $N = 32$ from Fig. 4.2, it suggests that using more pixels can improve the PPPP performance generally, but not when $h_2 - h_1 > 10$ km. This indicates the nonlinear effect can not be reduced by using more pixels.

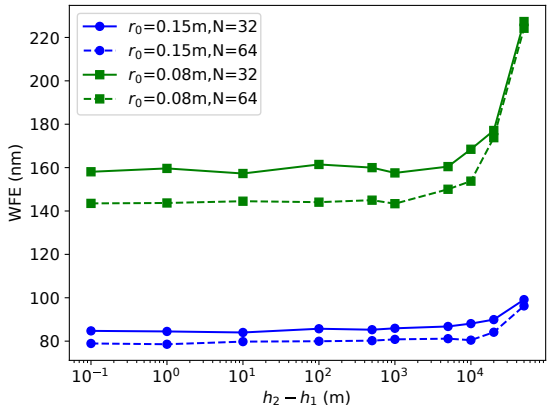

Figure 4.2: Investigation of $h_2 - h_1$. $h_2 - h_1$ increases from 0.1 m to 50 km. $N = 32$ and $N_Z = 78$ are used. The result is an average of 50 random phase screens.

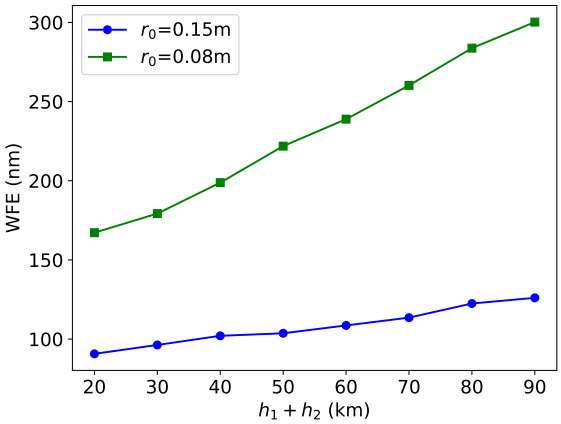

Figure 4.3: Investigation of $h_1 + h_2$. This figure is consistent with the theoretical analysis in section 2.3.2, where PPPP performance is inversely proportional to $h_1 + h_2$.

Now we analyze the sum of h_1 and h_2. The sum of h_1 and h_2 is increased from 20 km to 90 km with $h_2 - h_1 = 2$ m, and the corresponding results are shown in Fig. 4.3. It can be seen that the PPPP performance is inversely proportional to $h_1 + h_2$ due to the nonlinear effect (see section 2.3.2).

4.1.3 Investigation of I_0

Another variable parameter for PPPP is the laser beam profile at the telescope pupil I_0. We have investigated several different beam profiles, including a top-hat beam ($I_0 = 1$ inside the pupil and 0 outside the pupil) and super Gaussian beams to varying degrees (see Table 4.1). Super Gaussian beams are intermediate between a top-hat and the Gaussian-like beam, and can be controlled by changing the content of the exponent to a power P,

$$I_0 = e^{(-r^2/2\sigma^2)^P}. \tag{4.1}$$

The residual WFE for different I_0 is shown in Table 4.1. It is shown that the difference of the WFE caused by using different I_0 is up to a factor of 2. Generally speaking the beam profiles with a truncated edge (including the top-hat beam) perform worse than those with smoothed edge. The reason is that the edge-smoothed beam satisfies equation 3.32 and is more suitable for the linear reconstruction.

4.1.4 Chosen PPPP parameters

According to section 4.1.1, the suitable choice for the number of pixels number N and Zernike modes N_Z are $N = 32$ and $N_Z = 78$. Considering the balance of the nonlinear effect ($h_1 + h_2$ should be as small as possible) and the PPPP sensitivity ($h_2 - h_1$ should be as large as possible), the combination of $h_1 = 10\,\text{km}$ and $h_2 = 20\,\text{km}$ is chosen. As shown in Table 4.1, a Gaussian-like I_0 and a Super Gaussian with $P = 6$ give the best performance. As the linear reconstruction method proposed by Gureyev[75] uses the similar Gaussian-like beam, therefore we adopt this as I_0. The selection of PPPP parameters for the William Herschel Telescope (WHT) is summarized in Table 4.2.

Table 4.1: Investigation of different beam profiles I_0 on WFE.

beam profile	$r_0 = 0.15\,\mathrm{m}$ (at $500\,\mathrm{nm}$)	$r_0 = 0.08\,\mathrm{m}$ (at $500\,\mathrm{nm}$)
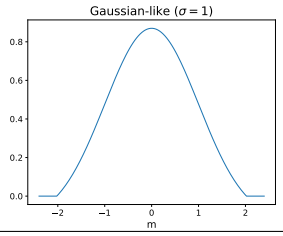	89.07 nm	168.49 nm
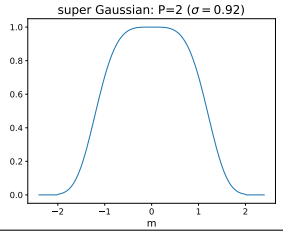	99.91 nm	198.22 nm
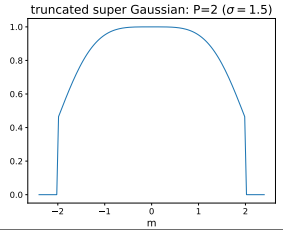	127.08 nm	222.20 nm
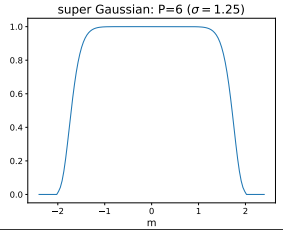	87.75 nm	164.90 nm
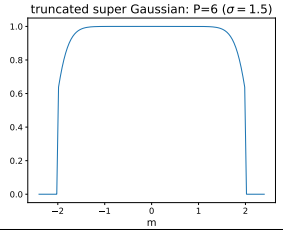	133.96 nm	247.04 nm
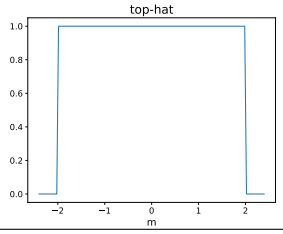	172.38 nm	287.74 nm

Table 4.2: Chosen PPPP parameters. These parameters are designed for a 4-m telescope. The wavelength of the launching laser is 1.06 μm.

N=32, $N_Z = 78$, $h_1 = 10\,\text{km}$, $h_2 = 20\,\text{km}$, Gaussian-like I_0

4.2 Investigation of turbulence altitudes

The above simulations in this chapter have only used a zero-height phase screen, however the real turbulence profiles are never like that. In this section we first look into one turbulence layer located at different altitudes and then analyze multiple turbulence layers.

If one turbulence layer is simulated and moved from the ground up to 25 km, the residual WFE is shown in Fig. 4.4. We can see that when the turbulence layer is below $h_1 = 10\,\text{km}$, the PPPP WFE is nearly constant. This can be proven by equation 2.16, where the signal $I_2 - I_1$ only relates to $h_2 - h_1$ rather than the turbulence altitudes. However when the turbulence layer h is in between h_1 and h_2, only the intensity pattern at h_2 can see the turbulence and, of course when $h > h_2$, PPPP is blind to its effect. Fortunately if the AO system operates in closed loop, the turbulence between 10 km and 20 km can be compensated to nearly the WFE when the turbulence is below 10 km (see section 4.5.1.3).

Fig. 4.5 shows an example of three turbulence layers, located at [0, 5, 10] km with relative C_N^2 strength [0.5, 0.3, 0.2], compared with a compact turbulence layer (sum of these three turbulence layers) on the ground. From Fig. 4.5 we know that multiple turbulence layers should not reduce PPPP performance as long as the turbulence layers are below h_1. In other words PPPP measures the integrated turbulence inside the laser beam below h_1.

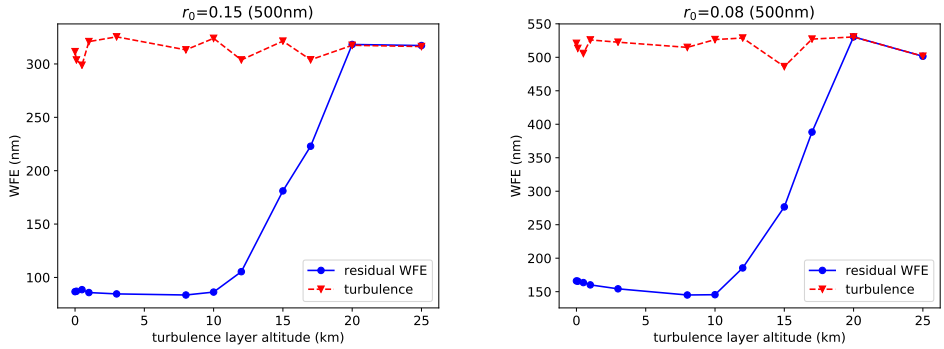

Figure 4.4: Investigation of one turbulence layer at different altitudes for $r_0 = 0.15$ and $r_0 = 0.08\,\mathrm{m}$. The parameters used are the same as in Table 4.2. The result is an average of 50 random turbulence realizations.

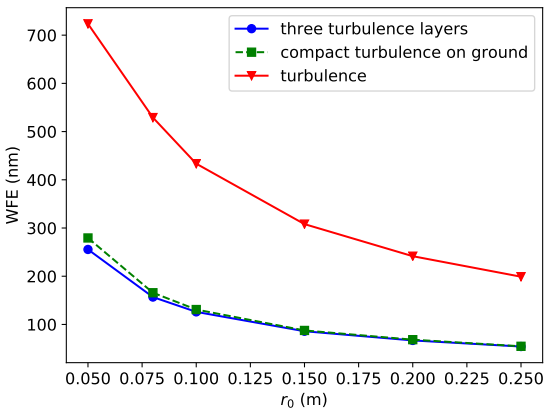

Figure 4.5: Investigation of three turbulence layers at different altitudes, compared with one compact turbulence layer (sum of these three turbulence layers) on the ground.

4.3 PPPP sensitivity and dynamic range

PPPP is not only an alternative LGS, but also a new wavefront sensing method. Thus we now analyze the PPPP sensitivity and dynamic range as in any other WFSs, in terms of defocus, astigmatism, coma and spherical aberrations (similar analysis for curvature WFS has been done by Roddier[89]). The procedure is very simple. We generate aberrations of individual Zernike modes with increasing amplitude, and compute the corresponding reconstructed Zernike coefficients. Comparing the initial and reconstructed amplitude of the Zernike coefficients, we

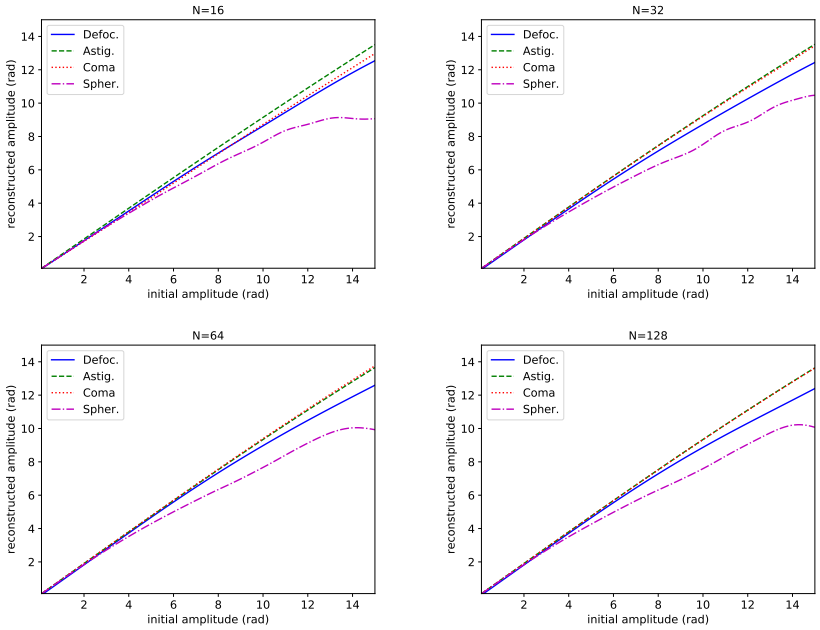

Figure 4.6: PPPP sensitivity and dynamic range when $h_1 = 10$ and $h_2 = 20\,\mathrm{km}$ for defocus, astigmatism, coma and spherical mode in terms of different N. The initial amplitude can be converted into 17 nm to 2530 nm for wavelength equaling $1.06\,\mu\mathrm{m}$.

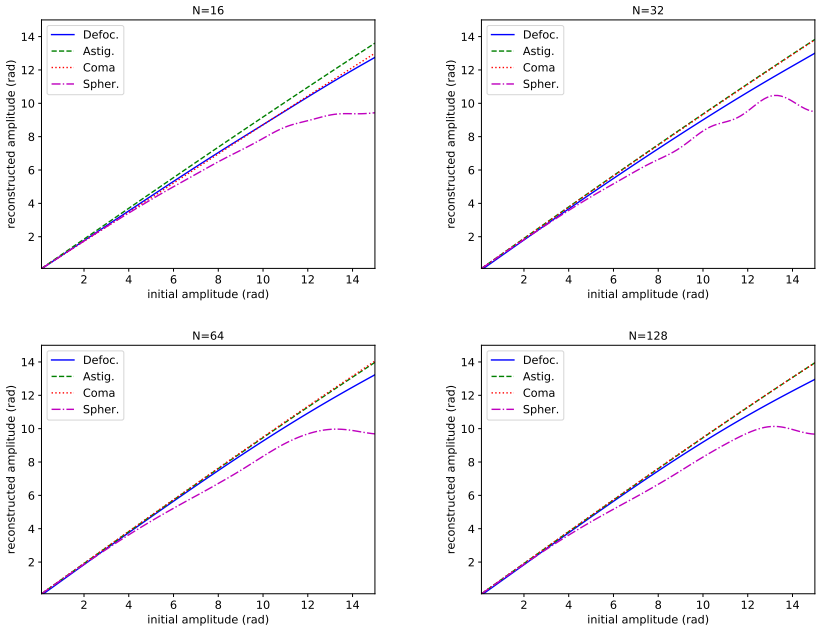

Figure 4.7: PPPP sensitivity and dynamic range when $h_1 = 10$ and $h_2 = 11\,\mathrm{km}$.

can know the PPPP sensitivity when the initial input is very small, and the dynamic range when the initial input is large. From Fig. 4.6 it is obvious that the curves are almost diagonal with small initial amplitude for all these four Zernike modes. That means PPPP has very good sensitivity. However for an initial amplitude larger than 4 radians, it starts to diverge for the spherical mode. Thus the dynamic range for PPPP is approximately 4 radians (equivalent to 675 nm at 1.06 μm wavelength) for the spherical mode, and nearly 2530 nm for the other three modes. Comparing plots with different pixel number N, there are no significant differences. This suggests that the sampling is sufficient even when $N = 16$ pixels for these four low-order modes. If the combination of h_1 and h_2 is changed to 10 and 11 km (see Fig. 4.7), the results are almost the same as $h_2 = 20$ km. This suggests that small $h_2 - h_1$ (equalling 1 km) is also sufficient for the noise free situation.

4.4 PPPP SNR analysis

Until now all the above simulation and analysis are based on a noise-free situation. In this section we present a detailed Signal-to-Noise Ratio analysis when the photon and read noise are added. According to the PPPP SNR analysis in section 4.4.1, we find that PPPP has a very low SNR when the laser power is 20 W. Therefore two attempts to improve SNR have been made in section 4.4.2.

4.4.1 PPPP SNR analysis

Firstly we only consider the photon noise using a 20 W laser (at 1.06 μm). Assume the normalized PPPP signal is

$$s_n = \frac{I_2 - I_1}{2I_0}, \tag{4.2}$$

then the variance of s_n is approximated as follows according to van Dam[78],

$$E[(s_n - \overline{s_n})^2] \approx 1/(N_1 + N_2), \tag{4.3}$$

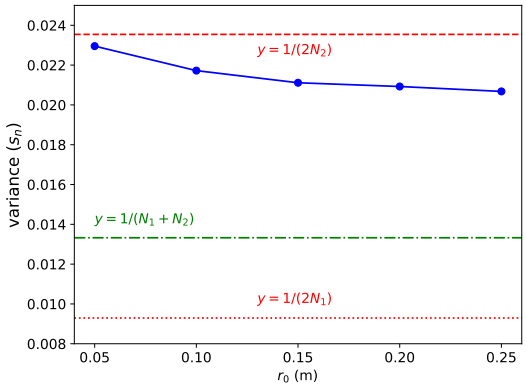

Figure 4.8: Variance of s_n in each pixel with different r_0. The results are an average of 50 random phase screens and for each phase screen 50 random Poisson distributions are performed to sample the effect of photon noise. The same applies to other figures in section 4.4. Note that a top-hat beam instead of a Gaussian-like beam is used here because there should be no difference between each pixel for a top-hat beam.

where N_1 and N_2 are the number of photons in each pixel from h_1 and h_2, and $\overline{s_n}$ represents the average of the normalized signal s_n. If 32×32 pixels are used to sample the pupil, the average return flux in each pixel for the detectors conjugate at h_1 and h_2 are 53.8 and 21.24 photons respectively according to section 3.2.1 with the parameters listed in Table 3.4 (4.24×10^4 and 1.67×10^4 photons in total). Then the theoretical variance of s_n caused by photon noise according to equation 4.3 should be $1/(53.8 + 21.24) = 0.0133$. The corresponding simulated average variance of s_n with different r_0 is plotted in Fig. 4.8, where $\mathrm{var}(s_n) \approx 0.021$. It can be seen that the curve exhibits the behavior predicted by equation 4.3 more closely when the amount of return flux from h_2 is used, *i.e.* the blue curve is more close to the upper horizontal red line with $y = 1/(2N_2)$. That suggests the photon noise for PPPP comes mainly from the detector conjugate at h_2 instead of h_1.

Now we add read noise as well to analyze the noise variance and the SNR. The PPPP signal is $s = I_2 - I_1$, and the variance of s is $E[(s - \overline{s})^2]$. Fig. 4.9 shows the variance of the noise including the photon and read noise, as well as their sum. We can see that both photon and read noise are independent of the turbulence strength r_0, and photon noise is dominant unless the read noise is larger than $5\,e^-$

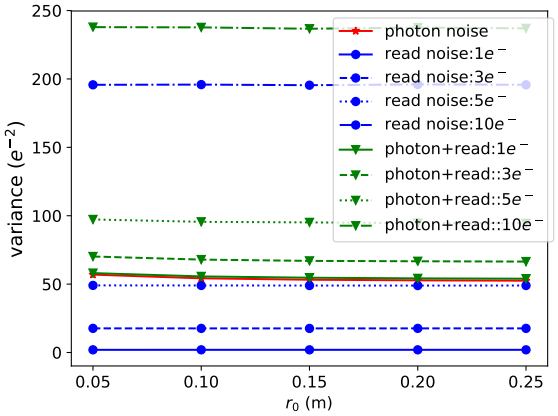

Figure 4.9: Variance of the error in terms of photon noise, read noise to a different degree and their combination. The variance of the read noise is 2 times of the theoretical value (1, 9 and 25 e^{-2} respectively) because two images are used together for PPPP. The results are an average of 50 random phase screens and for each phase screen 50 random Poisson (and Gaussian) distributions are performed to sample the photon (and read) noise. A top-hat beam is used again.

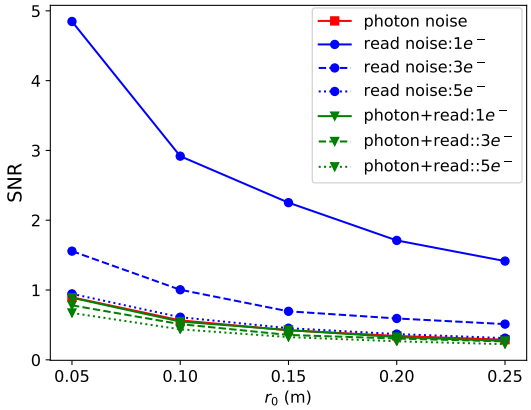

Figure 4.10: SNR including photon noise, read noise to a different degree and their combination. This is for a top-hat beam as well.

RMS.

Given the variance of the error of the photon and read noise, Fig. 4.10 provides the corresponding SNR with different r_0. It is obvious that all SNR curves decrease with r_0, which demonstrates that PPPP signal is inversely proportional to r_0 since the noise is independent of r_0. This is fairly easy to understand from equation 2.16,

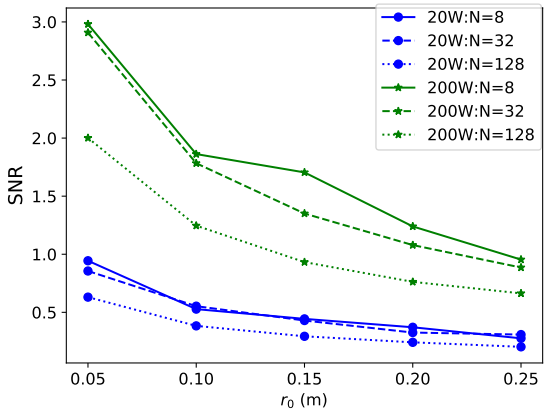

Figure 4.11: SNR including only photon noise with different pixel numbers and laser powers.

where the signal $I_2 - I_1$ is proportional to the first derivative and the curvature of ϕ. From Fig. 4.10 we find that the photon noise is the main limit to SNR when the read noise is less than $5e^-$. In reality we intend to adopt an Avalanche Photo-Diodes detector[90] instead of a CCD to reduce the read noise to nearly 0. We therefore ignore the read noise and analyze the effect of return flux on the photon noise. The number of photons in each pixel can be determined either by the laser power or the pixel size in a similar manner. The corresponding SNR is shown in Fig. 4.11, where we can come to the conclusion that binning the images (reducing N) to increase photon number in each pixel can improve SNR very slightly compared to increasing the laser power. That is because the binned signal is very badly sampled.

There are other noise sources such as dark current and sky background. These two kinds of noises are normally very small compared to the photon and read noise. For example the dark current is around $0.015e^-$ during 2.5 ms exposure time for the Keck OSIRIS (a near-infrared integral field spectrograph) detector. According to Gemini tests on Mauna Kea, the sky background is only about 10 photons per second per arcsec squared per meter squared at $\lambda = 1.06\,\mu$m.

4.4.2 Attempts to improve SNR

As shown in Fig. 4.10, PPPP SNR is below 1 and mainly limited by the photon noise for a 20 W laser. The low SNR renders PPPP impractical, and increasing SNR therefore is of great importance to advance PPPP to practical usage. We have made two attempts: one is using a modulated laser beam and the other is using multiple backscattered images from different altitudes instead of two.

4.4.2.1 Laser beam modulation

From equation 2.16, the PPPP signal $I_2 - I_1$ is determined by two terms: $\nabla I_0 \cdot \nabla \phi$ and $I_0 \nabla^2 \phi$. We have found that increasing the turbulence strength (decreasing r_0) can increase $\nabla \phi$ and $\nabla^2 \phi$, and thus giving better SNR (see Fig. 4.10). However the turbulence phase ϕ can not be controlled by instrumentation. Instead of increasing the derivative and curvature of ϕ, we can also increase ∇I_0 by modulating the laser beam I_0. Different types of modulation has been tried and the corresponding results are shown in Table 4.3. It is shown that the beam modulation with high frequency can improve SNR slightly, but can not help with the residual WFE. Increasing the pixel number N from 32 to 64 can slightly decrease the residual WFE.

4.4.2.2 Multiple backscattered images

Another attempt we have made is to use multiple backscattered images from different altitudes instead of two. Specifically the backscattered images from two altitudes (with 10 km difference in between) as one pair are subtracted to form the PPPP signal, just as before. Then up to 4 image pairs are combined to increase the SNR. The corresponding results are shown in Table 4.4. Again we find that using up to 4 combined PPPP signal can increase the SNR slightly, but no significant improvement for the residual WFE is obtained. The last thing we have tried with

Table 4.3: SNR and residual WFE for different types of modulation of the initial beam profile I_0. A 200 W laser is assumed.

beam profile	SNR	residual WFE when $r_0 = 0.15$
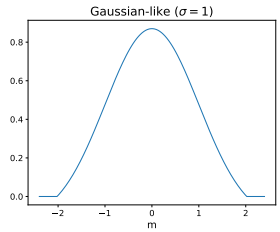	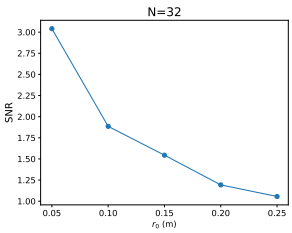	194.17 nm
	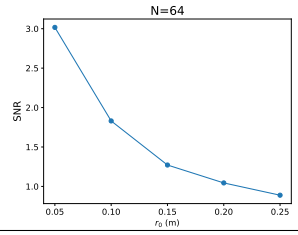	187.19 nm
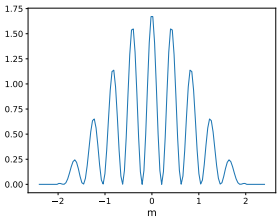	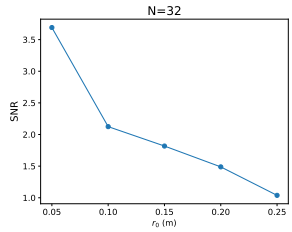	212.15 nm
	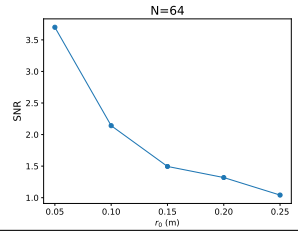	199.52 nm
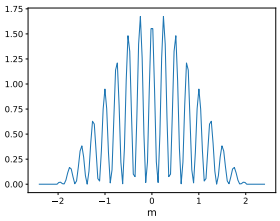	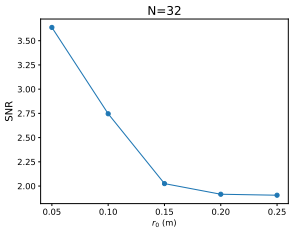	201.50 nm
	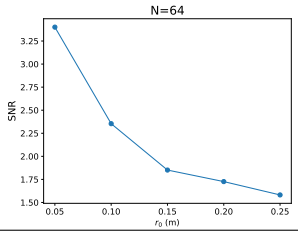	192.28 nm

Table 4.4: SNR and residual WFE for multiple backscattered images from different altitudes. Images from h_1 and h_2 are combined one by one as a pair to form the PPPP signal, and up to 4 pairs (*i.e.* 4 signals) are used to improve the SNR. $\Delta h_1 = 1$ and $\Delta h_2 = 5$ km are used as previous, as well as a 200 W laser.

altitudes of images pair (km)	SNR	residual WFE
h_1=[10] h_2=[20]	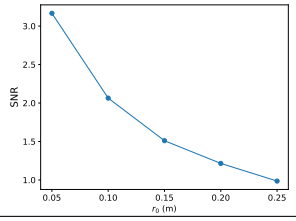	196.57 nm
h_1=[10,11] h_2=[20,21]	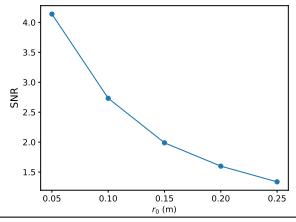	204.70 nm
h_1=[10,11,12] h_2=[20,21,22]	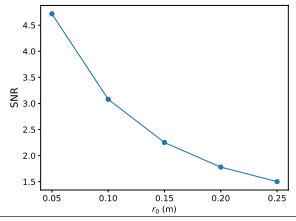	189.41 nm
h_1=[10,11,12,13] h_2=[20,21,22,23]	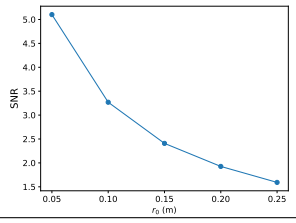	197.27 nm

success is using the Neural Network nonlinear reconstructor (see section 3.3.3 and section 4.5.2).

4.5 PPPP results from an AO simulation compared with a SH WFS

The PPPP simulation model has been integrated into *Soapy*, which is a Monte-Carlo Adaptive Optics simulation platform written in the Python programming

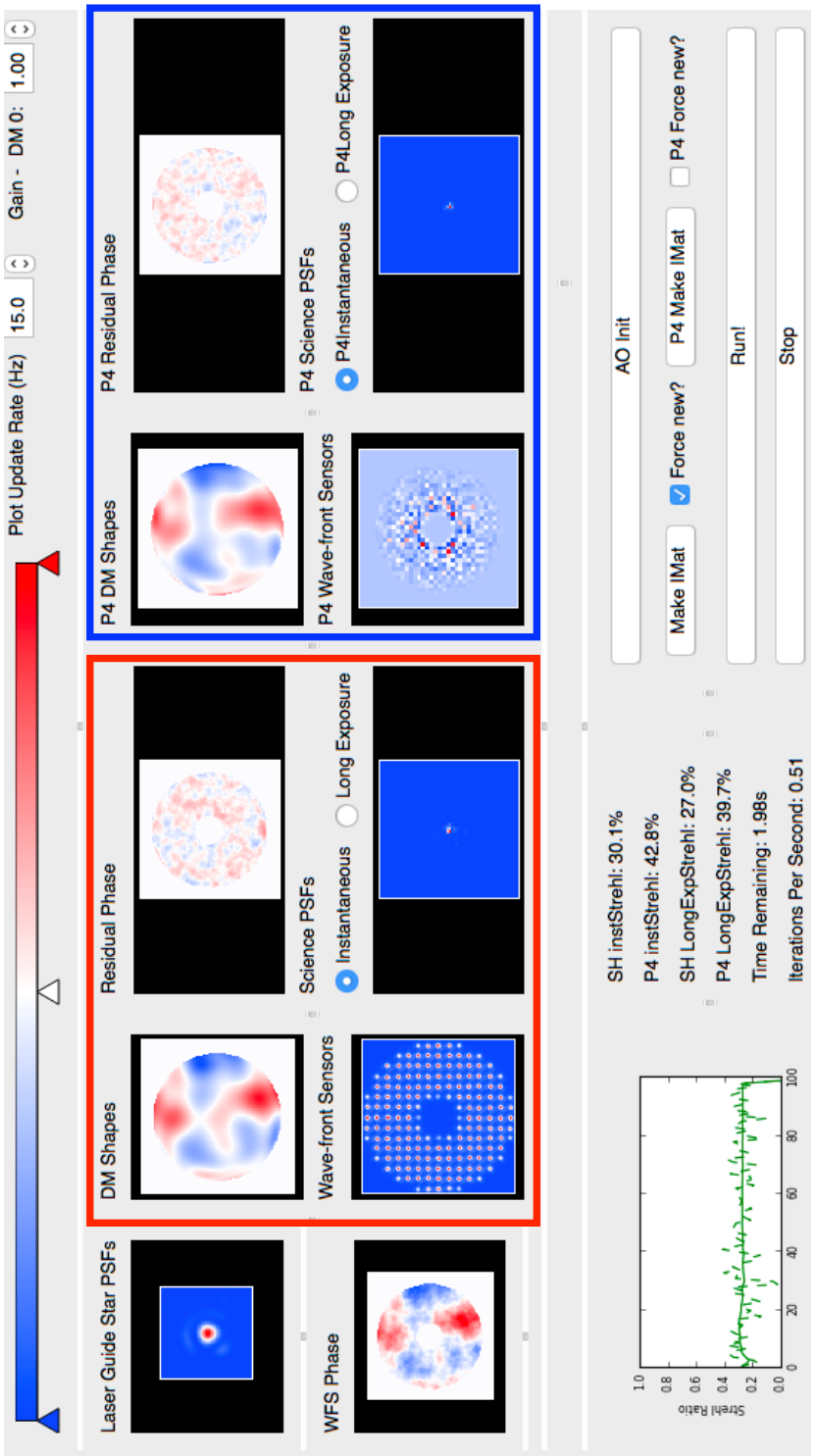

Figure 4.12: *Soapy* GUI including PPPP model. Example use of the simulation is provided by the GUI, which shows the phase observed ("WFS Phase") and the SH results (in the red box) including SH WFS images, DM shapes, residual phase of the science target and the science PSF. The corresponding results of PPPP are shown in the blue box.

Table 4.5: Parameters for the *Soapy* simulation. PPPP and SH WFS share the same parameters for Telescope, Atmosphere, DM and Science camera. T_0 is the transmission of the optical components and T_A is the one-way transmission of the atmosphere. N_Z is the highest order of Zernike mode.

Telescope	Atmosphere
D=4 m; L=4.8 m	one or 20 turbulence layers
128 × 128 pixels	T_A=1
T_0=0.5	
DM	Science camera
Zernike DM	64 × 64 pixels
$N_Z = 78$ (tip/tilt removed)	$\lambda = 0.8\,\mu$m
PPPP	SH WFS
32 × 32 pixels	LGS height : 10 or 20 or 90 km
λ=1.06 μm	λ=1.06 μm (or 589 nm)
h_1=10 km; h_2=20 km	10 × 10 sub-apertures
$\Delta h_1 = 1$ km; $\Delta h_2 = 5$ km	10 × 10 pixels per subap
read noise $3e^-$	read noise $3e^-$
η=0.8	

language[91]. The simulation is arranged into objects which represent individual AO components, such as the atmosphere, WFS, DM, and reconstruction, etc. A GUI of *Soapy* including PPPP model is shown in Fig. 4.12. The PPPP performance is estimated by the average residual WFE from 50 random turbulence realizations. As a comparison, a conventional Shack-Hartmann WFS with a Rayleigh LGS focused at 10 km or 20 km, or a sodium LGS has been used, with the parameters listed in Table 4.5. We present the PPPP simulation results using the linear and NN reconstructor separately.

4.5.1 Linear reconstructor

With the linear reconstructor, we first simulate one turbulence layer at different altitudes, to verify that PPPP is indeed free of Focal Anisoplanatism. Then representative turbulence profiles from ESO Paranal[61] with 20 layers are used for a more practical PPPP performance study. Finally closed loop results are presented in section 4.5.1.3.

4.5.1.1 Results with one turbulence layer

First we simulate only one turbulence layer located at 0, 5 and 10 km respectively, compared with a SH WFS. Fig. 4.13 shows the performance of the PPPP and SH WFSs with Rayleigh LGSs (10 km and 20 km) and sodium LGS. For different turbulence layer altitudes, the PPPP WFE (blue curves) keep almost the same (in both cases of $r_0 = 0.08$ and $r_0 = 0.15$ m), which confirms that PPPP is a focal-anisoplanatism free method. However it is obvious that PPPP curves increase rapidly when the laser power decreases, which is caused by the low SNR when laser power decreases (see section 4.4). The NN reconstructor has been demonstrated an effective approach to improve PPPP performance when the laser power is below 1000 W (see section 4.5.2). Looking at the SH WFS curves with Rayleigh and sodium LGSs (cyan, green and magenta curves), it is obvious that when the turbulence layer is on the ground, the WFE for all Rayleigh LGSs and sodium LGS are very similar. However when the turbulence layer moves up to 5 km or 10 km, the sodium LGS gives much better performance than Rayleigh LGSs. This proves the existence of Focal Anisoplanatism for a single LGS AO system.

Now we calculate the WFE variance caused by the Focal Anisoplanatism from Fig. 4.13. According to the propagation of error for uncorrelated variables with equal weight,

$$\sigma^2 = \sum_i^n \sigma_i^2, \tag{4.4}$$

where σ^2 is the total variance and σ_i^2 is the variance of the i-th element. Here the total variance is σ^2_{LGS}, including elements of σ^2_{NGS} and σ^2_{f} (representing Focal Anisoplanatism). σ^2_{LGS} can be extracted from Fig. 4.13 corresponding to the infinite laser power. σ^2_{NGS} can be extracted from the WFE value when the turbulence is on the ground (corresponding to the infinite laser power as well). Given σ^2_{LGS} and σ^2_{NGS}, the WFE caused by Focal Anisoplanatism is calculated and listed in Table 4.6. It is obvious that the lower the LGS is, and the higher the turbulence layer is, the bigger the WFE caused by the Focal Anisoplanatism becomes.

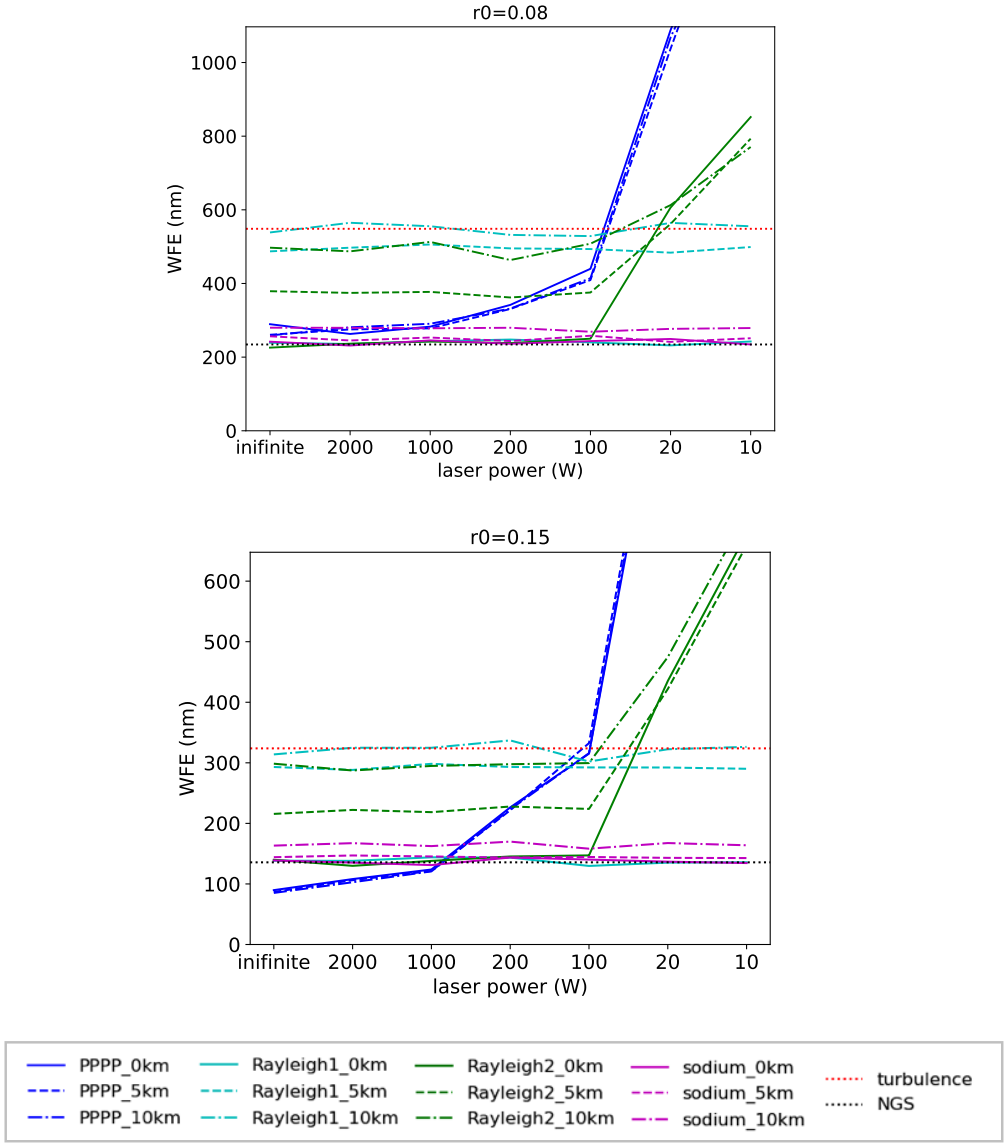

Figure 4.13: PPPP performance with linear reconstructor when one turbulence layer is located at 0, 5 or 10 km, compared with a SH WFS associated with either Rayleigh LGSs (10 km and 20 km) or sodium LGS. The x-axis is the average laser power. Rayleigh1 and Rayleigh2 represent Rayleigh LGSs located at 10 km and 20km, whose flux has been normalized to the same flux with I_1 and I_2 for PPPP respectively. "NGS" represents the result from a SH WFS with an infinitely bright NGS (no noise). The result is an average of 50 turbulence realizations from *Soapy* simulation.

Table 4.6: WFE RMS (nm) caused by focal anisoplanatism in terms of Rayleigh LGSs focused at 10 km and 20 km and sodium LGS when the turbulence layer is located at 5 or 10 km respectively. The turbulence WFE RMS is around $\sqrt{1.8} \approx 1.34$ times smaller than theoretical value given certain r_0 according to equation 1.9, and this is consistent with Fig. 3.5.

	turbulence layer altitude			
	$r_0 = 0.08$ m		$r_0 = 0.15$ m	
	5 km	10 km	5 km	10 km
Rayleigh1	427.1	484.8	259.8	283.1
Rayleigh2	297.8	438.4	167.6	265.9
sodium	104.4	153.1	48.7	90.8
PPPP	260.7		89.7	
NGS	234.3		135.7	
turbulence	548.5		323.8	

4.5.1.2 Results with 20 turbulence layers

To simulate a more realistic atmospheric turbulence, two representative optical turbulence profiles measured at Cerro Paranal are used, with r_0 equaling 0.0976 and 0.171 m at 500 nm[61]. The turbulence profiles are shown in Fig. 4.14. Both the turbulence profiles are consistent with the statistic analysis[92], where the turbulence on the ground is dominant, and there are several peaks between 5 and 20 km. Comparing these two profiles, we find that it is a stronger ground layer for $r_0 = 0.0976$, while for $r_0 = 0.171$ m the layer around 20 km is stronger. These two profiles are used since their r_0 values can cover the worst and best seeing from 83 nights in Paranal, with the percentage equaling 9.7% and 1.4%. Given these two turbulence profiles (20 layers model are used to save time), we can generate 50 random turbulence realizations, which are consistent with the relative turbulence strengths of the 20 layers. The integrated r_0 and individual r_0 to generate random phase screen at each layer are listed in Table 4.7.

Fig. 4.15 shows the performance of PPPP using these 20-layers turbulence profiles as shown in Fig. 4.14, compared with a SH WFS with either Rayleigh LGSs

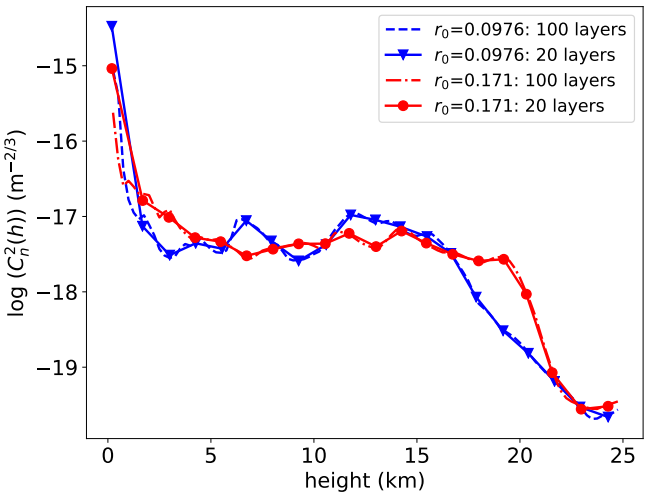

Figure 4.14: Two representative optical turbulence profiles from ESO Paranal[61] with r_0 equaling 0.0976 and 0.171 m at 500 nm. We show a 20 and 100 turbulence layers representative models and the one with 20 turbulence layers are used for the simulation to save time.

Table 4.7: The integrated r_0 and the corresponding separate r_0 for each layer.

turbulence layer height (km)									
0.2	1.7	3.0	4.3	5.5	6.7	7.9	9.3	10.6	11.8
individual r_0(m) when integrated $r_0 = 0.0976$ m									
0.10	3.87	6.57	5.29	5.84	3.49	5.06	7.30	5.43	3.14
individual r_0(m) when integrated $r_0 = 0.171$ m									
0.18	2.02	2.75	4.00	4.30	5.57	4.93	4.48	4.46	3.69
turbulence layer height (km)									
13.0	14.2	15.5	16.6	17.9	19.2	20.4	21.7	22.9	24.3
individual r_0(m) when integrated $r_0 = 0.0976$ m									
3.44	3.90	4.68	6.36	14.19	26.30	39.60	66.43	104.01	132.65
individual r_0(m) when integrated $r_0 = 0.171$ m									
4.71	3.54	4.41	5.42	6.12	5.94	11.26	47.35	92.19	88.46

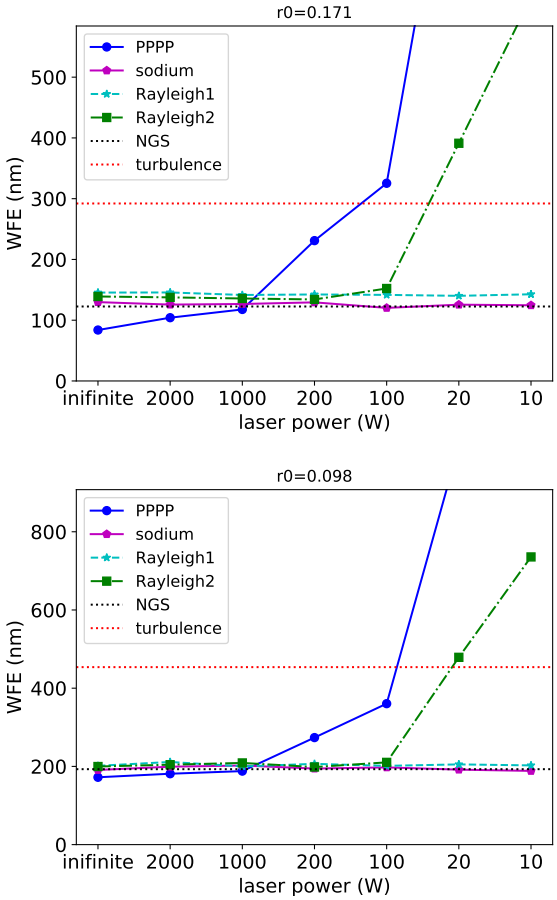

Figure 4.15: The PPPP performance with linear reconstructor using 20-layers turbulence profile, compared with a SH WFS associated with either Rayleigh LGSs (10 km and 20 km) or sodium LGS. The result is an average of 50 turbulence realizations from *Soapy* simulation.

(10 km and 20 km) or sodium LGS. We can find again that PPPP residual WFE increases rapidly with decreasing laser power. When the laser power is ≥ 1000 W PPPP slightly overtakes the SH WFS. While for laser power < 1000 W especially < 200 W, PPPP is very disadvantageous. On the contrary the SH WFS, associated with either Rayleigh LGS or sodium LGS, is not sensitive to the laser power in the range of 10 W to infinite power except for Rayleigh2. That is because the flux of Rayleigh2 is scaled to the same as I_2, which is only 39% flux of I_1.

For infinite laser power, PPPP can achieve 84 nm WFE RMS when $r_0 = 0.171$ and

172 nm WFE RMS when $r_0 = 0.098$. We know that for a 4-m telescope and one single sodium LGS, the WFE RMS caused by the Focal Anisoplanatism is 83.6 nm at 1.06 μm (see Fig. 2.3) when the 20-layers turbulence profile with integrated $r_0 = 0.0976$ m is used, which is already roughly half of the PPPP WFE (172 nm) and would be much more critical for larger telescopes.

4.5.1.3 Closed loop results

In this section a closed loop PPPP (including laser uplink correction automatically) is operated, and the results with only one turbulence layer at different altitudes is shown in Fig. 4.16. It can be seen that the results of closed loop PPPP is slightly better than open loop when the turbulence layer is below $h_1 = 10$ km, but much better for the turbulence layer located between $h_1 = 10$ and $h_2 = 20$ km (excluding $h_2 = 20$ km). That is because the partially measured turbulence between $h_1 = 10$ and $h_2 = 20$ km is gradually corrected within several iterations in closed-loop mode. In terms of SH WFS, it is almost the same between the closed-loop and open-loop results since we assume a perfect DM in this simulation.

Table 4.8: Closed-loop PPPP with 20-layers turbulence profile with the integrated $r_0 = 0.0976$ m. The residual WFE after 10 iterations instead of 20 is used to prevent accumulated errors on the edge. Again the residual WFE is computed inside a circle with 0.95 pupil size.

WFE (nm)	PPPP	Rayleigh1	Rayleigh2	sodium
closed loop	132.37	180.24	179.16	171.23
open loop	173.57	174.88	171.22	162.46
turbulence	380.39			

If the 20-layers turbulence profile is applied, then the corresponding closed-loop results are given in Table 4.8. Again we find that the closed-loop PPPP outcompetes the open-loop PPPP because of the high-altitude turbulence, while the SH WFS results are similar for closed and open loop.

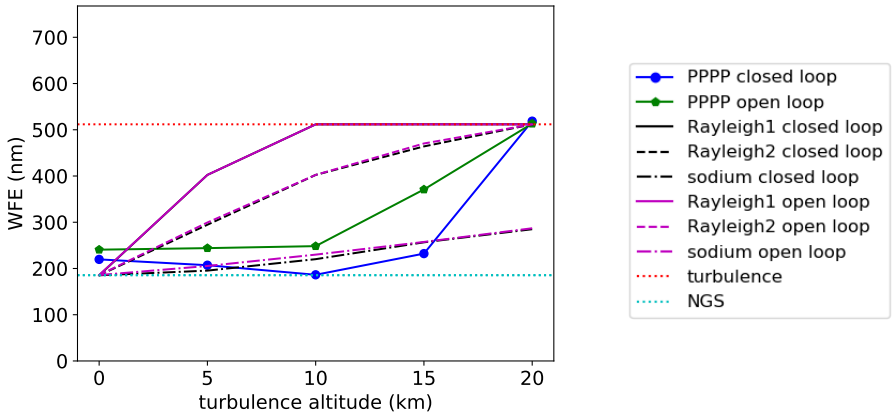

Figure 4.16: Closed loop PPPP performance with one turbulence layer located between 0 and 20 km. This is a noise-free situation and the gain of the closed loop control for both PPPP and SH WFS is 0.7. The closed loop result is the residual WFE after 20 iterations. Note that the result is from only one fixed phase screen instead of an average of 50 random phase screens. To prevent accumulated errors on the edge after iterations, the residual wavefront error are computed inside a circle with 0.95 pupil size.

4.5.2 Neural Network reconstructor

As the linear reconstructor is not able to provide good performance when the laser power is below 1000 W, we will use the NN reconstructor instead in this section. The NN reconstructor was integrated into *Soapy* as a nonlinear reconstructor. For a wavefront sensing comparison with PPPP, a SH WFS (26×26 sub-apertures) associated with an infinitely bright NGS is implemented.

4.5.2.1 Suitability for real-time operation

The number of operations for each reconstruction method is now discussed in terms of highlighting suitability for real-time use. For the NN, reconstruction is calculated network layer by layer. In the convolutional stage, each image is multiplied with all the filters. The amount of calculations required for each subsequent convolutional layer is reduced substantially when propagating through the NN hence the convolution operations dominate. In the fully connected layers the number of operations

is equal to the product of the number of input neurons by the number of output neurons. The total number of arithmetic operations for the NN reconstruction is therefore estimated as $\sim 875,000$. In comparison, the linear reconstructor uses a matrix vector multiply operation (the reconstruction matrix of size $(N_Z-3)^2$ is multiplied with measurement related vector F, which is a length (N_Z-3) vector). This makes the matrix-vector-multiplications require a $O[(N_Z-3)^2]$ number of calculations. However, the formation of F_j requires pixel-by-pixel processing for $N_p = \pi(N_{pupil}/2)^2 \approx 2300$ per image. This is $O[2(N_Z-3)N_p]$ for two images and so dominates the number operations. It is estimated that $\sim 365,000$ operations are required for the linear reconstruction. Therefore the NN is only $\sim$2 times more computationally complex than the linear method and the processing of the input data, I_1 and I_2, dominates in both methods.

4.5.2.2 Performance of NN reconstructor

For the NN validation the same two representative optical turbulence profiles are used (see Fig. 4.14), with r_0 equalling 0.0976 and 0.171 m at 500 nm respectively. The simulation is configured to run in open loop.

Initially, we discuss the NN after it is trained with all laser powers. From the two turbulence profiles shown in Fig. 4.14 and the PPPP parameters listed in Table 3.9, the average WFE is obtained from 50 random turbulence realizations. The results with different laser powers (varying photon noise in the measured images) are shown in Fig. 4.17. It is found that the NN reconstructor can significantly reduce the residual WFE when the laser power is less than 1000 W compared with the linear reconstructor, which in turn reduces the laser power requirements for implementation. As expected, for both the linear and NN reconstructor, with larger WFE the corresponding standard deviation increases. Comparing $r_0 = 0.0976$ m and $r_0 = 0.171$ m, we find that the intersection of the two reconstructors is around 500 W for $r_0 = 0.0976$ m, and 1000 W for $r_0 = 0.171$ m. For the linear reconstructor, equation 2.16 implies the signal $I_2 - I_1$ is larger for poorer seeing. However the NN

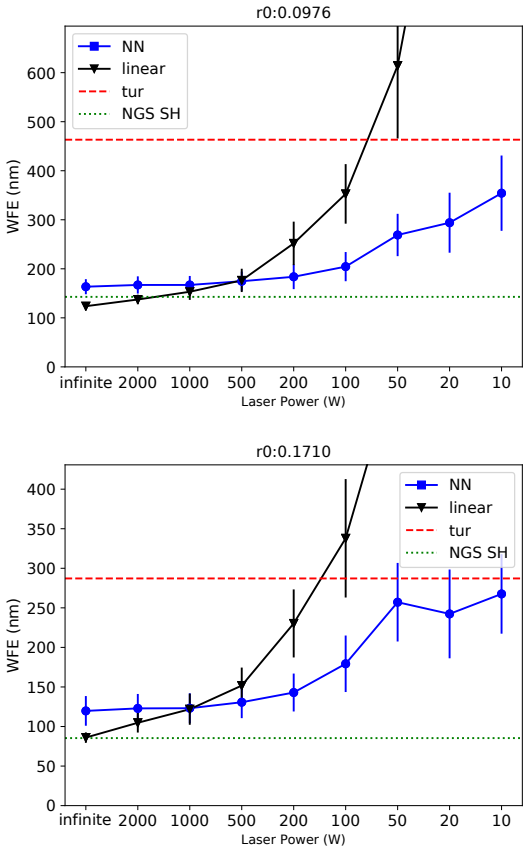

Figure 4.17: The WFE (nm) of linear and NN reconstructor with different laser powers. The "NGS SH" shows the ideal performance and the "tur" represents the RMS of the uncorrected wavefront. The result is an average of 50 random turbulence realizations from the *Soapy* simulations.

reconstructor is not as sensitive to the seeing which suggests that the NN is using I_1 and I_2 independently and not their difference directly. The intriguing suggestion is that sufficient information for reconstruction is contained within each image, and this is discussed in section 4.5.2.3.

To understand the source of discrepancy in reconstructor performance, the reconstructed Zernike coefficients are shown in Fig. 4.18, which shows the AO-corrected Zernike coefficients variance for laser powers equalling 20 W, 200 W and infinity and for both turbulence profiles. For all three wavefront sensing configurations (PPPP NN, PPPP linear and NGS SH), with no photon noise (top row) the residual is consistent with a constant fractional error. The linear PPPP retrieval,

however, has a suggestion of structure consistent with smaller residuals for Zernike polynomials with smaller azimuthal frequency. This structure becomes clear when a 200 W laser is simulated for both PPPP reconstructors (PPPP NN and PPPP linear), although it is weaker for the NN reconstructor. For the lowest laser power, 20 W, the correlation between the Zernike azimuthal frequency and coefficient variance becomes clear for both the PPPP reconstructors. However, the NN always gives a result better than the turbulence itself, while the linear reconstructor has a useless retrieval if a 20 W laser is used.

The NN reconstructor used so far is trained from the combined datasets of 10, 20, 200 W and infinite laser power, which results in 1,200,000 independent combinations of inputs and outputs. Using this NN we demonstrate that the reconstructor has slightly worse performance (168 nm WFE RMS for $r_0 = 0.0976$ and 120 nm for $r_0 = 0.171$ m) than the linear reconstructor (125 nm WFE RMS for $r_0 = 0.0976$ and 86 nm for $r_0 = 0.171$ m) for infinite laser power, but much better performance for laser powers ≤ 500 W (see Fig. 4.17).

The total flux of the measured backscattered images can change from laser power declining through lifetime effects or from the opacity of the atmosphere changing. The NN model used so far therefore has the advantage of being insensitive to the number of photons detected. The alternative scenario is fixing the laser power during training the NN. The result is that the performance from a single-power trained NN is only slightly better than the multiple-power trained NN but only for the specific training laser power. Table 4.9 gives the corresponding WFEs, suggesting 160 nm RMS when r_0=0.0976 m and 125 nm RMS when r_0=0.171 m for a 4-m telescope if a 200 W laser is used. If error sources such as the fitting and temporal errors are ignored and the tip/tilt is compensated for perfectly then the expected Strehl Ratio is 0.67/0.56 in J band for $r_0 = 0.171$ m when using a single/multiple power trained NN reconstructor.

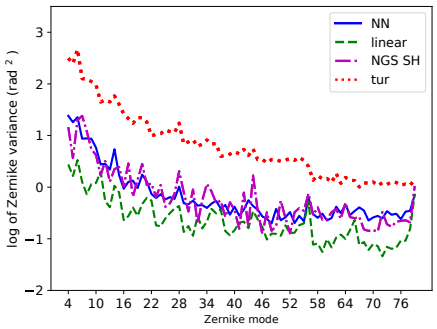

(a) r_0=0.0976 m; infinite power

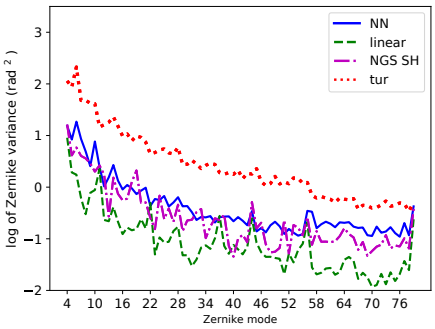

(b) r_0=0.171 m; infinite power

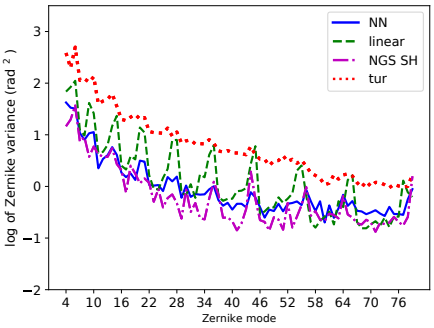

(c) r_0=0.0976 m; 200 W

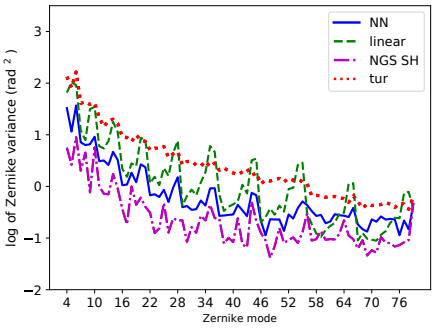

(d) r_0=0.171 m; 200 W

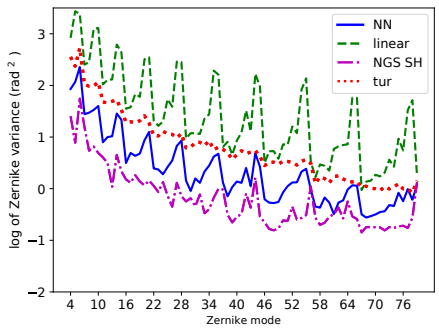

(e) r_0=0.0976 m; 20 W

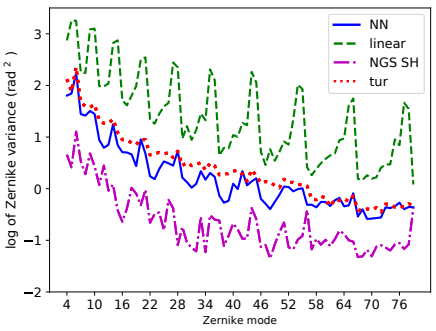

(f) r_0=0.171 m; 20 W

Figure 4.18: Residual variance of the Zernike coefficients for the linear and NN reconstructor from AO simulation for different laser powers and for the two turbulence profiles, *(left)* $r_0 = 0.0976$ and *(right)* $r_0 = 0.171$ m. The "NGS SH" lines shows the idealized performance from a noiseless SH WFS and the "tur" lines are the uncorrected Zernike coefficient variances.

Table 4.9: WFE (nm) for different models using different training datasets. The first three rows use a NN trained with laser power equalling: only 20 W, only 200 W or a combination (10, 20, 200 W and infinity). The WFE of the linear reconstructor and NGS SH are shown for comparison, as well as the uncorrected turbulence RMS.

dataset	validation laser power					
	r_0=0.0976 m			r_0=0.171 m		
	∞	200 W	20 W	∞	200 W	20 W
200 W	137	160	1160	92	125	1146
20 W	305	324	282	235	231	219
combined	168	178	281	120	147	236
linear	125	248	1132	86	226	1171
NGS SH	142			86		
Turbulence	460			290		

4.5.2.3 Using one image to train the NN

As discussed earlier, the trained NN reconstructor did not appear to use the difference of I_1 and I_2, but instead I_1 and I_2 independently. Therefore, a NN can be trained with just one image. We trained a single image NN reconstructor with either I_1 or I_2 as the input component of the datasets. Both of the training, combined datasets for 20 W and 200 W power were used. The corresponding results for a I_1-only reconstructor are shown in Fig. 4.19 (results from training with I_2 are worse hence not discussed further). Encouragingly, the I_1-only NN reconstructor shows a better performance in the simulation than the linear reconstructor (which requires both I_1 and I_2) for laser powers below 200 W. This result points towards a simplified on-sky implementation for PPPP with a NN reconstructor wherein the camera shutter needs only be required to have an open/close repetition rate per pulse rather than twice within a pulse. Due to the optical and mechanical simplicity, Hickson[93] has also tried to do wave-front curvature sensing from a single defocused image, and found it is feasible at good astronomical sites, *i.e.* good seeing condition.

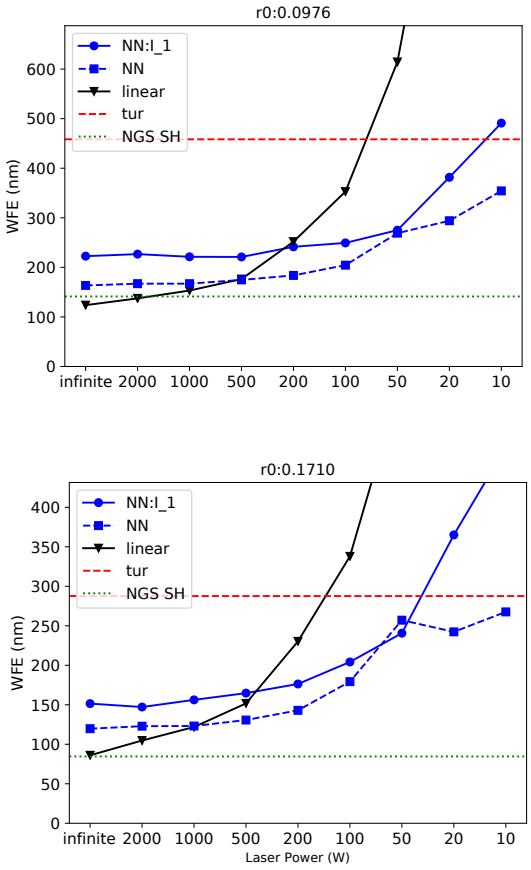

Figure 4.19: The WFE (nm) of a I_1-only reconstructor. "NN: I_1 " represents the NN model trained with only I_1 and "NN" represents the model trained with both I_1 and I_2 (see Fig. 4.17). The result is an average of 50 random turbulence realizations from *Soapy* simulations.

4.6 Summary

In this chapter we first analyzed the PPPP performance in terms of various parameters (including the number of pixels $N = 32$ to sample the images, Zernike modes $N_Z = 78$ for reconstruction, propagation altitudes of the two backscattered images $h_1 = 10\,\text{km}$ and $h_2 = 20\,\text{km}$, as well as the initial launching laser beam profile I_0) and provide a suitable choice of the PPPP parameters. Given these simulation parameters, we then investigated the effect of the turbulence layer altitudes and find that PPPP is insensitive of the turbulence altitudes as long as the turbulence is below h_1. As a wavefront sensing technique, PPPP has great sensitivity and

large dynamic range from the example of four low-order aberrations. A detailed SNR analysis is given and the major problem of PPPP has been demonstrated to be the low SNR, and two attempts to improve the PPPP SNR have been discussed. Finally we show the simulation results from a full AO simulation platform *Soapy* with a PPPP model integrated, using both the linear and NN reconstructor, compared with a conventional LGS AO system using the SH WFS. We find that the PPPP can achieve similar performance as a SH WFS with one single sodium LGS using the linear reconstruction but only when the laser power is above 500 W. For lower laser power, NN reconstructor has been shown as an effective method and thus can advance PPPP to practical usage.

Chapter 5

Laboratory experiment

PPPP is very different from a conventional LGS AO system, in terms of the laser launching configuration, wavefront sensing technique and reconstruction process. Similar systems have never been built on the bench, not to mention on sky. Thus a laboratory demonstration is necessary for understanding the PPPP technique, including extracting the PPPP signal, calibrating the system, reconstructing the phase, and how it behaves compared with a SH WFS, before putting a lot of staff effort and resources into the on-sky experiment. In this chapter we describe a proof-of-concept laboratory demonstration of PPPP[94].

5.1 Experimental description

The optical layout of PPPP laboratory experiment is shown in Fig. 5.1 and the actual bench picture is shown in Fig. 5.2. This setup includes propagating the laser beam to two different distances (*i.e.* the upward propagation) and re-imaging the backscattered light from the scatter screen. The DM used in this experiment is a 40-actuator Piezoelectric DM, with a circular keystone DM actuator array shown in Fig. 5.3. This DM is DMP40/M-P01 from Thorlabs, which is suitable for generating low-order Zernike aberrations (from tip/tilt to 15th Zernike mode) and ideal for correcting distortions that result from common sources of wavefront

aberrations, such as astigmatism and coma, and include a separate mechanism to adjust for tip/tilt. From Fig. 5.1 the propagation distances are controlled by moving the mirror pair $M_{3a,b}$ on a rail, and the scattered light is re-imaged through the same optical path back into the PPPP beam profile imaging camera. The merit of the design employed is that when moving the mirror pair from position 1 to position 2, we can simply move f_7 and Camera2 together and the images have the same pixel scale in terms of the beam diameter. The signal for PPPP is the subtraction of these two images (after scaling them to the same flux amount to satisfy the conservation of energy). Given the measured PPPP signal, we use a linear modal reconstruction method based on Zernike-like modes. A SH WFS is used as a comparison with PPPP, and Camera1 is used to record the Point Spread Function (PSF). The relevant parameters are listed in Table 5.1.

Table 5.1: Parameters of PPPP experiment shown in Fig. 5.1. The unit is millimetres. The size of the lenslet is 10×10 mm with 500 μm pitch. The SH WFS has 9×9 subapertures. The two propagation distances (h_1=600 and h_2 =900 mm) are equivalent to 29.6 and 44.4 km altitudes on-sky for a 4-m laser beam.

D_1=12	D_2=18	h_1=600	h_2=900	f_1=50
f_2=100	f_3=150	f_4=250	f_5=150	f_6=75
f_7=100	f_8=100	f_9=25	f_{10}=30	f_{11}=16
B/S2: 50:50 R:T		B/S1&3: 10:90 R:T		λ = 633nm

The laboratory setup is a simplified demonstration of the PPPP on-sky configuration (see Fig. 2.13) due to the limited experimental conditions, regarding the three major processes (*i.e.* upward propagation, return path and reconstruction). Specifically during the upward propagation, we use the DM or a piece of perspex of low optical quality (the lid of a container) as the atmosphere simulator. As for the return path, the scatter material (which should be the atmospheric molecules on-sky) is simplified as a reflective tape. In addition the very significant difference between the laboratory and on-sky experiments is that the light travels through the atmospheric turbulence during both upward propagation and return path for

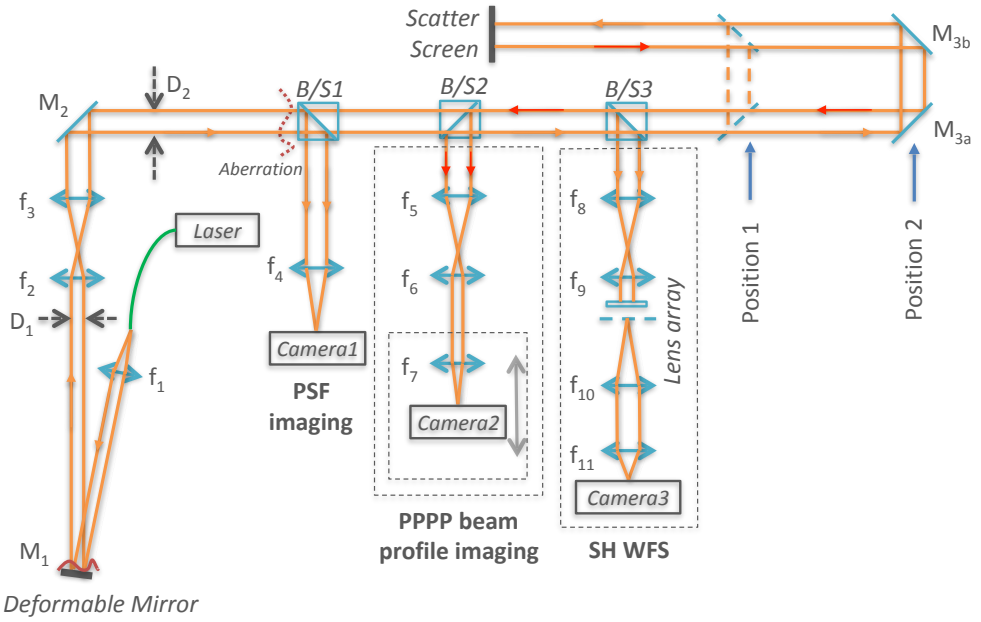

Figure 5.1: Optical layout of PPPP. A 633 nm laser beam is confined into a single mode fiber and the other end of the fiber is mounted on a pinhole, performing as a point source. After passing through lens f_1, a collimated beam is formed from the point source. The collimated beam then reaches the DM. Here the DM has two functions: one is as the atmosphere simulator to generate random aberrations (the aberration is generated on the DM and the conjugate plane is shown in the red dotted line labelled "Aberration"); and the other one is as a normal wavefront corrector. f_2 and f_3 are the optical relay to change the beam diameter from D_1 to D_2. The beam is then transmitted through B/S1 (the reflected light from B/S1 goes into the Camera1), B/S2 and then is divided into two parts at B/S3. The first part (10% reflected light from B/S3) goes into the SH WFS, and the main part (90% transmission light) propagates to the Scatter Screen (here a reflective tape is used) via the mirror pair $M_{3a,b}$. Then the light scatters back from the scatter screen and travels back to the PPPP beam profile imaging camera through the mirror pair again. f_5 and f_6 are another optical relay, and f_7 and Camera2 are used to record the image of the backscattered pattern from the scatter screen.

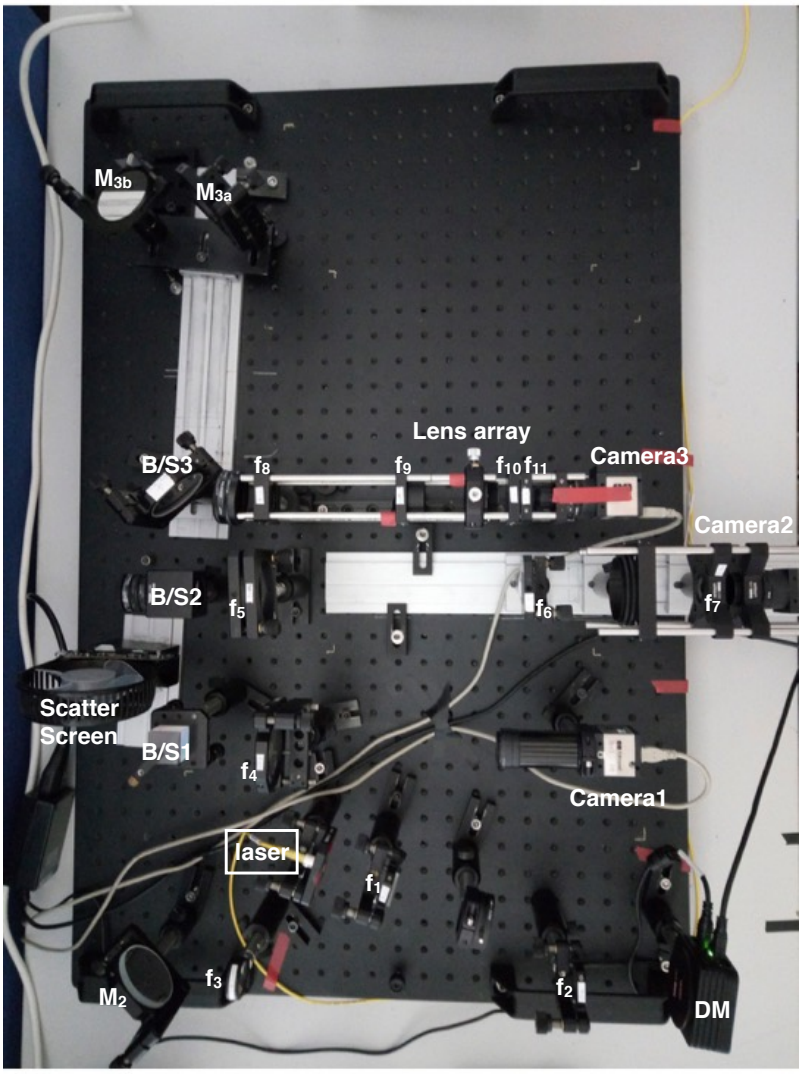

Figure 5.2: The laboratory experiment of PPPP.

the on-sky experiment, while in this laboratory experiment the laser beam only passes through the atmospheric turbulence during the upward propagation process if the DM is used as the atmosphere simulator. This difference can be neglected though when the images are binned so that each pixel is larger than the downward turbulence-introduced PSF (see section 3.2.2). To verify this, we replace the scatter screen with a 1951 USAF target illuminated by a torch (there is no laser light here) and taking the image of the target from the PPPP beam profile imaging camera, with the perspex as the atmosphere simulator. The perspex is placed at

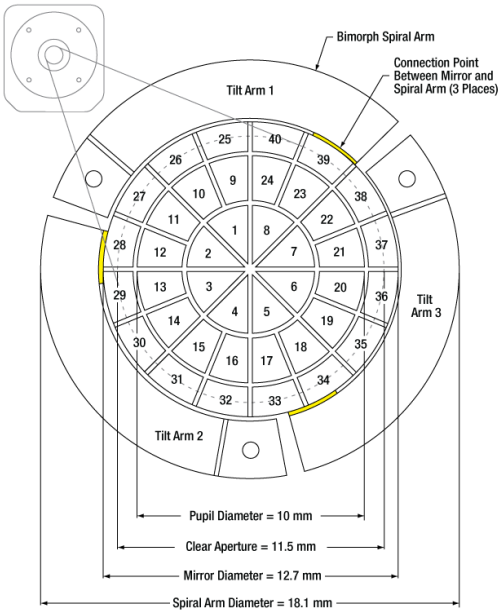

Figure 5.3: The circular keystone DM actuator array (credit to Thorlabs).

two positions: one is right after B/S2 (equivalent to 2500 m altitude for a 4-m laser beam); and the other is very close to the scatter screen. According to section 3.2.2 the blurring effect of h_2 is more severe than h_1, thus we put the mirror pair at position 2 to simulate the worst case.

The images of the USAF target are shown in Fig. 5.4, as well as the corresponding binned images. Comparing Fig. 5.4b and Fig. 5.4c, we know that the lower the turbulence layer is, the more blurred the images become. However when the images are binned from 300×280 down to 30×28 pixels, the effect of the turbulence during the return path can be neglected (see Fig. 5.4e and Fig. 5.4f). This re-imaging test using the USAF target is consistent with the return path process of a 4-m laser beam scattered back from the altitude of 44.4 km. According to the simulation (section 3.2.2), 57×57 pixels are the maximum to sample the backscattered images to eliminate the return path effect if $h_2 = 20$ km when $r_0 = 0.15$ m at 500 nm, and 28×28 pixels when $r_0 = 0.08$ m. From Fig. 5.4 we demonstrate 30×28 pixels are sufficient to eliminate the return path effect even when $h_2 = 44.4$ km (which means more blurring effect) for the perspex as the atmosphere simulator. However

the optical effect of the perspex does not match the atmospheric statistics (such as Kolmogorov theory[2]), so there is no r_0 which can be derived from it. This test then is to show the effect of the re-imaging process and the effect of binning images qualitatively rather than quantitatively.

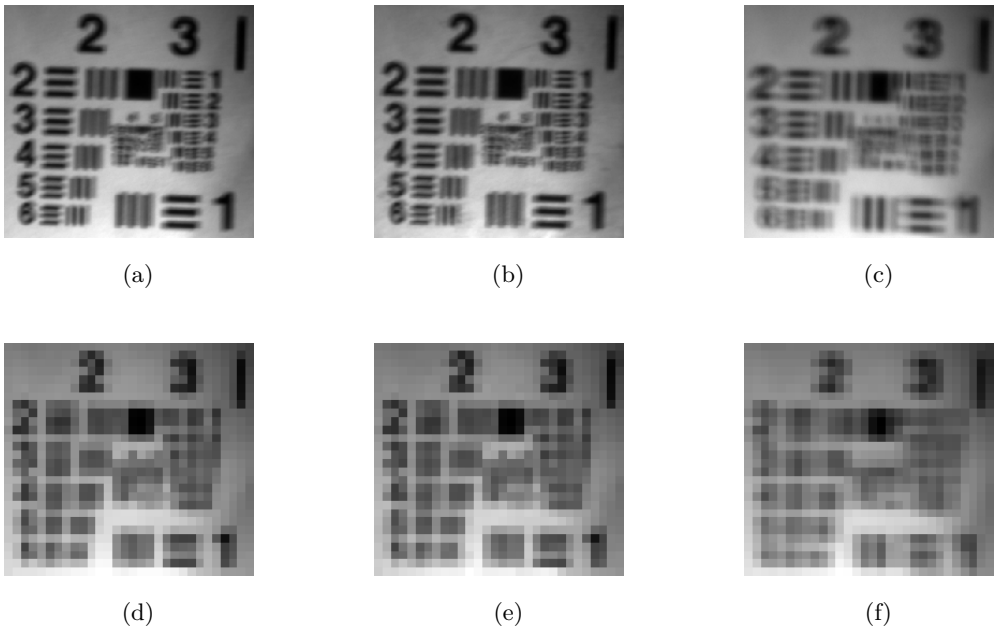

(a) (b) (c)

(d) (e) (f)

Figure 5.4: Images of the 1951 USAF target. Fig. 5.4a is the original image of the 1951 USAF target without the perspex as the phase screen. Fig. 5.4b and Fig. 5.4c are the images when the perspex is placed very close to the target (equivalent to 44.4 km altitude for a 4-m laser beam) and right after B/S2 (equivalent to 2500 m altitude for a 4-m laser beam) respectively. Fig. 5.4d, Fig. 5.4e and Fig. 5.4f are the corresponding down-sampled images from 300×280 pixels to 30×28. The size of the 1951 USAF target is 20×18 mm.

5.2 PPPP signal

When a fixed piece of reflective tape is used as the scatter screen, the images from the PPPP camera (Camera2) are very speckled (see Fig. 5.5a) because of the diffuse reflections of laser light acting on the fixed scatter screen. In reality the atmospheric molecules move very fast with time scale $\sim$several ns, while the atmospheric coherence time is with time scale $\sim$ms. So the laser speckles will be

averaged out during the "frozen" length of the turbulence. To simulate the average effect, we simply place the scatter screen on a rotating disk to average out the speckles (see Fig. 5.5b). The structure of Fig. 5.5b is due to the diffraction effect when reflecting from the DM.

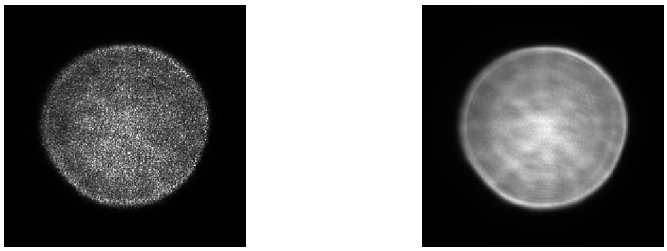

(a) speckled image (b) smoothed image

Figure 5.5: Speckled and smoothed images with rotating disk. The images are taken when the mirror pair is at position 2 and they are similar to those at position 1 although with less diffraction effects.

The PPPP signal is the subtraction of the images at h_1 and h_2, *i.e.* I_1 and I_2 respectively. Corresponding to this laboratory experiment, I_1 is the image of the scattered pattern when the mirror pair is at position 1 and I_2 is from position 2. $I_{1;0}$ and $I_{2;0}$ are the images when the DM is neutral (all the actuators are set to 100 V with range 0 to 200 V). Due to the optical static aberrations and diffraction effects, it is not possible to get zero signal from $I_{2;0} - I_{1;0}$. Thus $I_{2;0} - I_{1;0}$ is considered as the bias signal. Then adding a simple aberration (15th Zernike mode) from the DM, we get the corresponding images and PPPP signal (see Fig. 5.6). In terms of the simulated signal (Fig. 5.6h), since only $I_{1;0}$ and $I_{2;0}$ are measured instead of the beam profile at the pupil I_0, we use Fresnel diffraction to propagate the laser beam $I_{1;0}$ (Fig. 5.6a) with distance -h_1 to the ground, then adding a simulated 15th Zernike polynomial and propagating it back to h_1. In this way the simulated image I_1 can be obtained, and similarly for I_2. Then the simulated signal is the subtraction of the simulated I_2 and I_1 (with the bias, Fig. 5.6c, removed). Comparing the simulated and measured PPPP signal (Fig. 5.6h and Fig. 5.6g), it shows

great similarity on the edge but some difference in the middle. That is because the simulated 15th Zernike polynomial is different from the actual 15th Zernike mode generated from the DM. It is worth noting that the images have a total intensity of $\sim 2 \times 10^6$ ADU (analogue to digital units), which corresponds to an approximate 1500 W laser (at 1.06 μm) for on-sky PPPP, where the altitudes of h_1 and h_2 equal 10 km and 20 km, the optical transmission of the system is 0.5 and the quantum efficiency of the detector is 0.8. As shown in chapter 4, a 1500 W laser performs almost the same as in a noise free situation. Therefore this laboratory experiment is only a proof-of-concept experiment without a complete study of the noisy situation.

5.3 PPPP calibration

In this proof-of-concept laboratory experiment, we only use the linear reconstruction method. For the linear reconstruction, there are two approaches for the PPPP calibration. One is to generate individual Zernike modes (or their approximation) by the DM (termed DM modes) and get the corresponding PPPP signal, placed in a so-called interaction matrix. The other is to calculate a theoretical interaction matrix according to section 3.3.1 given the laser beam profile at the pupil I_0. We use both of the calibration methods. The interaction matrix can be theoretically calculated as long as I_0 is known, thus it is fairly easy to obtain. The theoretical method is based on the Zernike polynomials[14] instead of the DM modes, thus there will exist an error when applying the reconstructed Zernike coefficients, from the theoretical calibration, to the DM directly for correction. Therefore the theoretical calibration here is used only for the wavefront measurement experiment (instead of a full closed loop control). The measured calibration, on the contrary, is used for the AO closed loop control. The advantage of the measured method is that it can cancel out the static aberration from the optical system, especially the difference of the optical aberration between position 1 and position 2 when

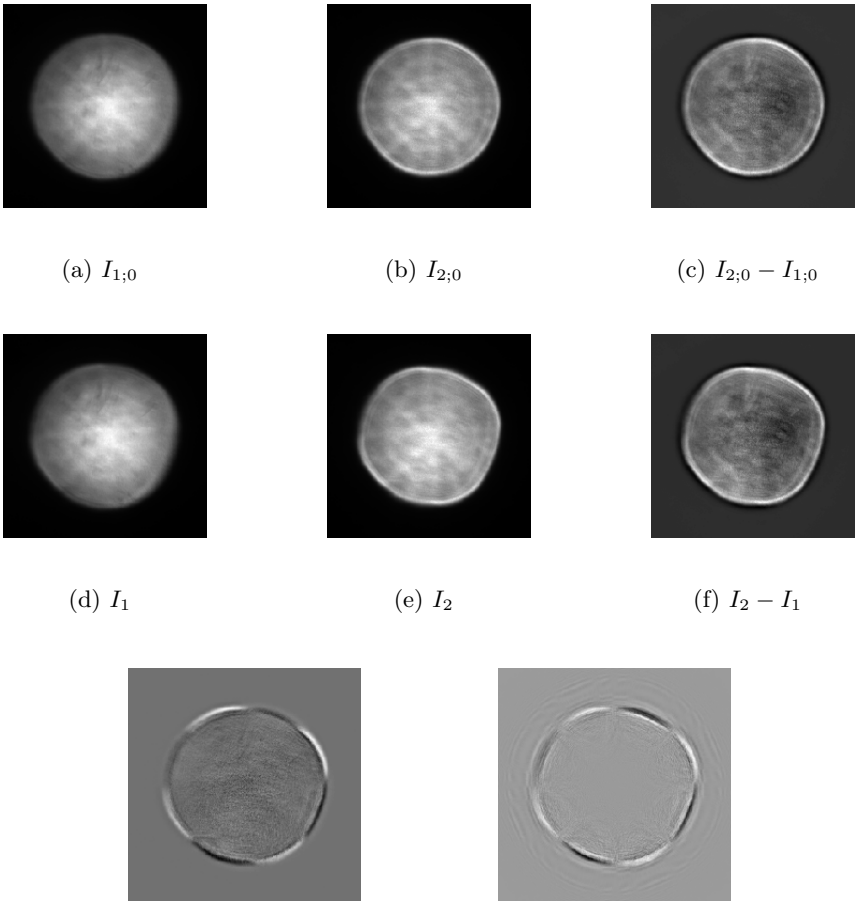

(a) $I_{1;0}$ (b) $I_{2;0}$ (c) $I_{2;0} - I_{1;0}$

(d) I_1 (e) I_2 (f) $I_2 - I_1$

(g) $I_2 - I_1 - (I_{2;0} - I_{1;0})$ (h) simulated

Figure 5.6: Images of backscattered patterns with neutral DM and the 15th Zernike mode added on the DM. Fig. 5.6a and Fig. 5.6b are images with neutral DM at position 1 and position 2 respectively (*i.e.* $I_{1;0}$ and $I_{2;0}$). Fig. 5.6c is the bias signal $I_{2;0} - I_{1;0}$. Fig. 5.6d, Fig. 5.6e and Fig. 5.6f are the corresponding results when the 15th Zernike mode (quadrafoil) is added. Fig. 5.6g is the measured signal for the 15th Zernike mode with the bias signal removed (*i.e.* the subtraction of Fig. 5.6f and Fig. 5.6c) and Fig. 5.6h is the corresponding simulated result as a comparison.

re-imaging the scattered patterns. It can also connect the DM voltage command with the measured PPPP signal directly without knowing the actual wavefront.

5.3.1 Theoretical calibration

The theoretical calibration, together with the reconstruction, is based on the Gureyev linear method[75]. The final expression of the interaction matrix **M** is

$$M_{ij} = \int_0^{2\pi} \int_0^R I_0 \nabla Z_i \cdot \nabla Z_j r dr d\theta, \tag{5.1}$$

where Z_i is i-th Zernike mode, and R is the radius of the laser beam. The beam profile at the pupil I_0 here is approximated as the average of $I_{1;0}$ and $I_{2;0}$. The reconstructed Zernike coefficients $\vec{a}$ corresponding to the phase ϕ then can be expressed as

$$\vec{a} = kR^2 \mathbf{M}^{-1} \vec{F}, \tag{5.2}$$

where $\vec{F}$ is the scalar product of the measured signal with element

$$F_j = R^{-2} \int_0^{2\pi} \int_0^R \frac{I_2 - I_1}{h_2 - h_1} Z_j r dr d\theta. \tag{5.3}$$

5.3.2 Measured calibration

For the measured calibration, each DM mode is generated twice with an equal positive and negative magnitude. The magnitudes for each DM mode to generate the measured interaction matrix are shown in Table 5.2. Then the corresponding final PPPP signal is the subtraction of the PPPP signal for the positive magnitude and the PPPP signal for the negative magnitude, then divided by two. The measured interaction matrix is shown in Fig. 5.7. Notice that tip/tilt modes are excluded because a NGS is still needed for the tip/tilt measurement for PPPP, just as in any conventional LGS AO system.

Table 5.2: Magnitudes (Peak-to-Valley stroke, PV) for each DM mode to generate measured interaction Matrix. The unit is micrometres.

Z_j	4	5	6	7	8	9	10	11	12	13	14	15
PV	0.65	0.68	0.68	0.25	0.25	0.24	0.24	0.1	0.11	0.11	0.21	0.21

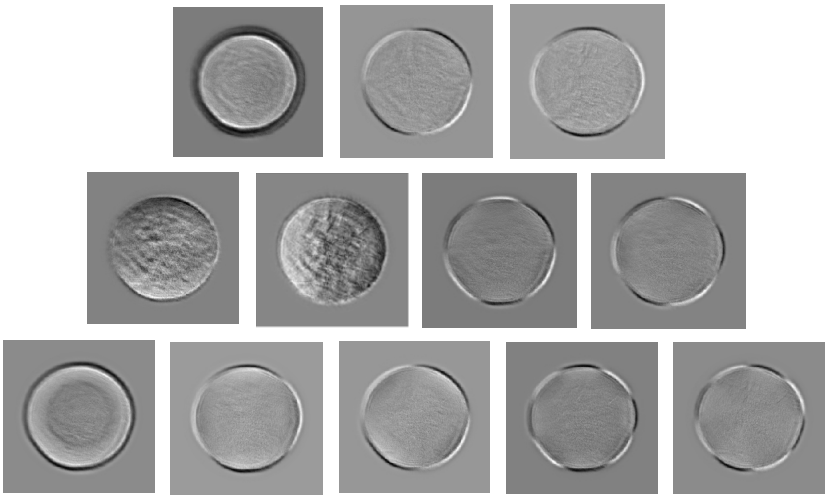

Figure 5.7: 2D display of the measured interaction matrix for each DM mode (from 4th to 15th Zernike modes).

5.3.3 Comparison of theoretical and measured calibration

The theoretical interaction matrix **M** from equation 5.1 is a square matrix (12×12) from the 4th to the 15th Zernike modes. To compare **M** with the measured interaction matrix, we calculate the correlation matrix, which is the dot product of any two modes, from the measured interaction matrix, and the result is shown in Fig. 5.8. There exists a big difference between the measured correlation matrix (Fig. 5.8a) and the theoretical one (Fig. 5.8b). It indicates again that DM modes are quite different from the simulated ones and the correlation between each Zernike mode (for example the 4th and 11th Zernike modes) for the measured interaction matrix is much larger than the theoretical one.

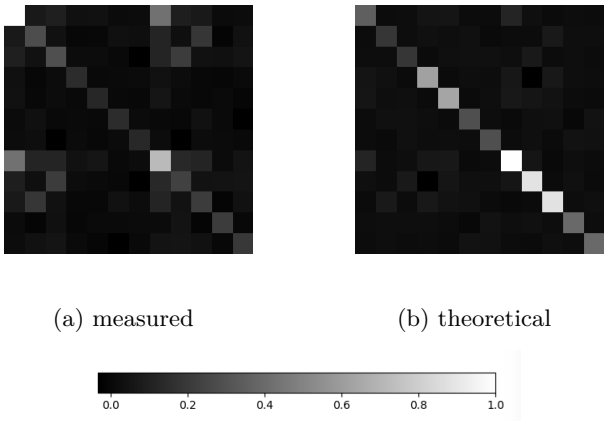

(a) measured (b) theoretical

Figure 5.8: Normalized correlation matrix. Fig. 5.8a is the correlation matrix of the measured interaction matrix and Fig. 5.8b is the theoretical interaction matrix. Both the correlation matrices are 12×12, from 4th to 15th Zernike mode.

5.4 Experimental results

Corresponding to these two calibration methods, there are two modes for this PPPP experiment. One mode is the wavefront measurement using the theoretical calibration, where the distorted wavefront is reconstructed but no AO correction is involved. The other mode is a complete AO closed loop using the measured calibration.

5.4.1 Wavefront measurement

The theoretical calibration is used for the wavefront measurement, according to equation 5.2. To verify the measurement accuracy, a SH WFS is used for comparison. Specifically a theoretical reconstruction using Fried geometry from the SH slopes is used to reconstruct the distorted wavefront[8].

For the wavefront measurements, the perspex used in Fig. 5.4 is used as the turbulence simulator here again. The perspex is placed right after B/S2 (equivalent to 2500 m altitude for a 4-m laser beam). In this case the beam goes through the turbulence during both the upward propagation and return path, and the blur-

ring effect is most severe for the return path (see Fig. 5.4). Thus this wavefront measurement experiment is consistent with the on-sky PPPP situation, for a worst case since the turbulence is near the ground which has more blurring effect for the return path. Fig. 5.9 shows the reconstructed phases from both PPPP and SH WFS. From Fig. 5.9a to Fig. 5.9d, we can see that the reconstructed phases from SH WFS and PPPP are very similar and that increasing the pixel number N from 32 to 128 has almost no effect on the reconstructed phases. That is because of the blurring effect of the return path, which limits the pixel number of the binned images to be 32×32 at most. In terms of the reconstructed Zernike coefficients (Fig. 5.9e), it shows again $N = 32$ and $N = 128$ are very similar to each other, as well as to the SH result, but slightly different from $N = 8$. Comparing $N = 32$ and SH WFS, the "residual of $N = 32$ & SH" curve has a relatively big absolute value especially for defocus (the difference between $N = 32$ and SH is 149 nm) and spherical (232 nm). This error might come from the static aberration of the optical system, especially the difference of the optical aberration between reimaging the scattered patterns from position 1 and position 2.

5.4.2 Closed loop control

The measured calibration is used for the closed loop control, and the DM is used as both the atmosphere simulator and wavefront corrector to perform an internal closed-loop AO system. When a random aberration is generated by the DM, we measure the images I_1 and I_2 and get the corresponding PPPP signal $I_2 - I_1$ (with the bias $I_{2;0} - I_{1;0}$ removed). Then multiplying the PPPP signal with the control matrix (which is the pseudo-inverse, from singular value decomposition, of the measured interaction matrix), we can get the reconstructed 12 DM coefficients. Applying this reconstructed phase on the DM, one iteration of the closed-loop control is finished. For the next iteration, only the residual aberration is measured. The voltage command applied on the DM can be expressed as $C_n = C_{n-1} + a_n \cdot g$ (C_n means the absolute voltage command required for n-th iteration, a_n represents

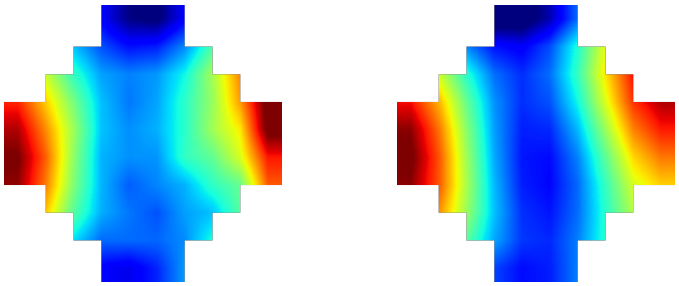

(a) SH

(b) N=32

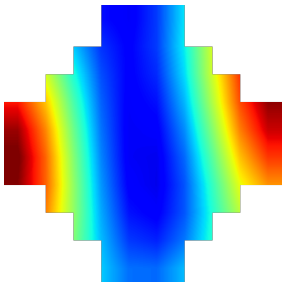

(c) N=8

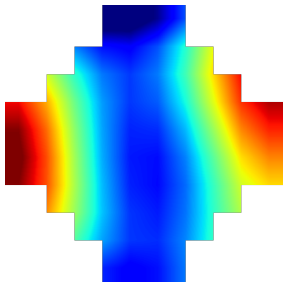

(d) N=128

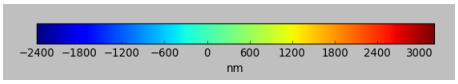

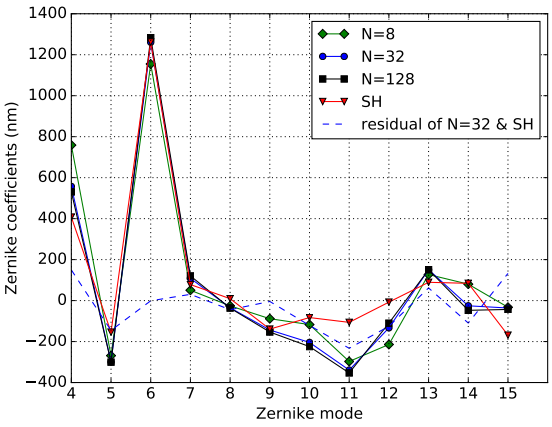

(e) reconstructed Zernike coefficients

Figure 5.9: Reconstructed phases from PPPP and SH WFS using the perspex as the atmosphere simulator. Fig. 5.9a is the reconstructed phase from the SH WFS. Fig. 5.9b, Fig. 5.9c and Fig. 5.9d are the reconstructed phases from PPPP when the images are binned to N equaling 32, 8 and 128 pixels respectively. The plots are shown on the same color scale (-2400 to 3200 nm). Fig. 5.9e shows the corresponding reconstructed Zernike coefficients.

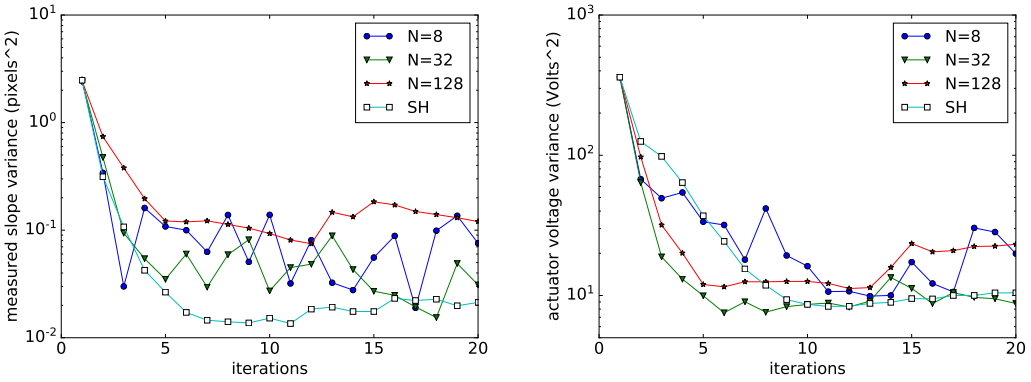

(a) slopes variance (b) actuator voltage variance

Figure 5.10: Closed loop results in terms of different binned pixel number N for a random aberration generated by the DM for both PPPP and SH WFS. Fig. 5.10a gives the variance of the measured slopes for x-axis and Fig. 5.10b shows the variance of the actuators' voltage.

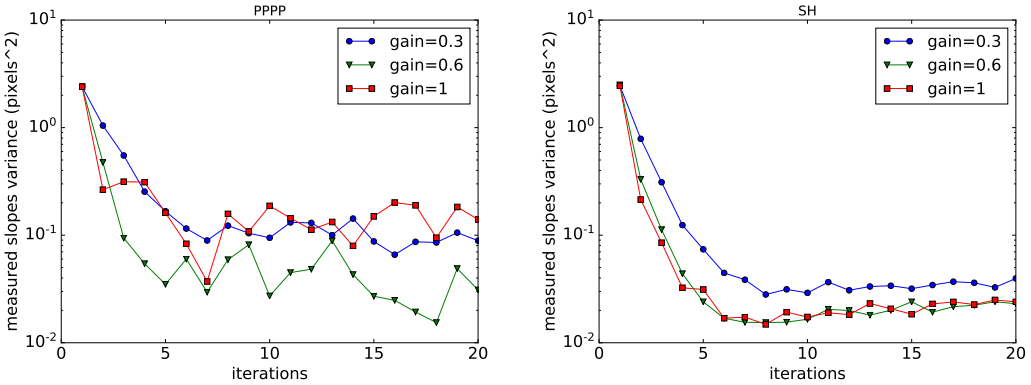

(a) PPPP (b) SH

Figure 5.11: Closed loop results in terms of closed-loop gain from the same aberration as in Fig. 5.10 for both PPPP and SH WFS. Fig. 5.11a shows the PPPP results and Fig. 5.11b is the SH results. $N = 32$ is used here.

the reconstructed DM coefficients and g is the gain), and $C_0 = 0$ (corresponding to a neutral DM, where all the actuators are set to 100 V). The closed loop is repeated for 20 iterations. Again a SH WFS is used for comparison with similar measured calibration method, where the measured slopes are placed in an interaction matrix when each DM mode is generated.

As shown in section 5.4.1, the binned pixel number N is an important parameter for PPPP. Fig. 5.10 shows the closed-loop results of one random aberration generated by the DM in terms of different N. The performance is estimated by the variance of the measured slopes, as well as the variance of the actuators' voltage. The variance of the measured slopes should be close to 0 with iterations. Since the DM is used as both the aberration generator and the wavefront corrector, the variance of the actuators' voltage should approach 0 as well. From Fig. 5.10 we can see that $N = 32$ gives a slightly better result after 20 iterations. The reason that $N = 32$ outperforms $N = 128$ might be that oversampling can lead to coupled error from high-order modes. Also since the return path will introduce a blurring effect and limit the pixel size N to 32, we come to the choice of $N = 32$. The result of the SH WFS in Fig. 5.10 is slightly better than PPPP. Since the results are shown on a logarithm scale, the absolute difference between PPPP and SH actually is quite small. This shows great potential for PPPP since the SH WFS is a commonly-used WFS for AO systems.

The closed-loop gain is another key parameter for both PPPP and SH WFS for closed loop AO system. Fig. 5.11 shows the performance of both PPPP and SH WFS in terms of different closed-loop gain (only the variance of the measured slopes is shown here) when the same aberration as in Fig. 5.10 is generated on the DM. From Fig. 5.11 we find that the greater the gain is, the faster it converges; also the smaller the gain is, the more stable the system becomes. As a balance we choose the gain equaling 0.6. The measured slopes variance for PPPP converges to around 0.03, and it can reach 0.02 for SH WFS.

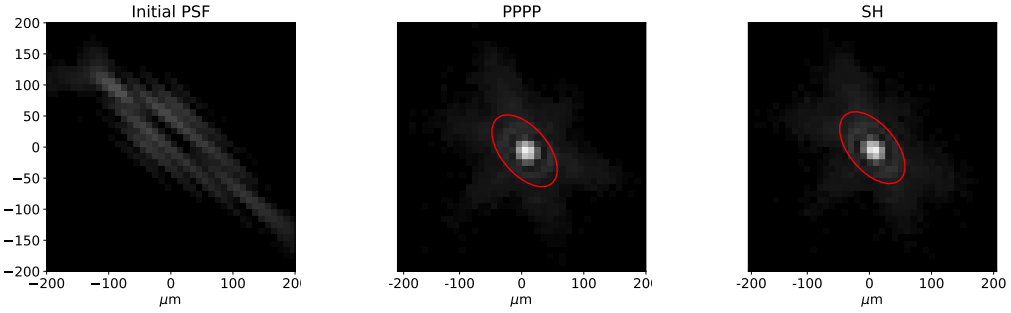

(a) (b) (c)

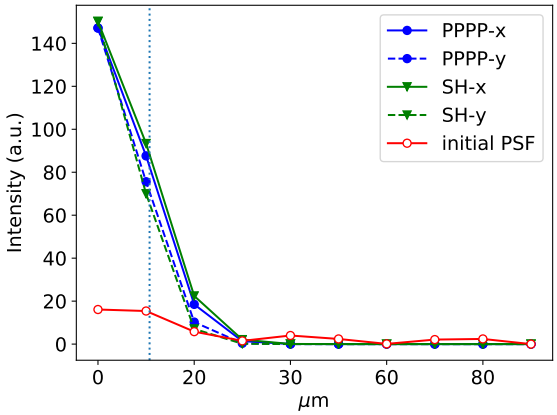

(d)

Figure 5.12: Initial and corrected PSFs. To illustrate the detailed pattern of the PSFs, Fig. 5.12a, Fig. 5.12b and Fig. 5.12c show the square root of the PSFs. The red ellipse in Fig. 5.12b and Fig. 5.12c shows a Gaussian fit. Fig. 5.12d is the cross section of Gaussian fit along rotated 'x' and 'y' axis, where the FWHM can be estimated as 23.12 μm (x-axis) & 20.40 μm (y-axis) with a 41.08 degree rotation (Counterclockwise) for PPPP, and 24.15 μm (x-axis) & 19.05 μm (y-axis) with a 39.38 degree rotation for SH WFS. The vertical dotted line shows the diffraction limited region, which equals to 10.72 μm.

With the chosen $N = 32$ and gain = 0.6, Fig. 5.12 gives the corresponding PSFs after 20 iterations for both PPPP and SH, as well as the initial PSF we start with. From Fig. 5.12 we can see that after 20 iterations the PSFs from both PPPP and SH are mostly limited to within the diffraction limited region and improve significantly compared to the initial PSF. From Fig. 5.12b and Fig. 5.12c we can see that within 20 iterations, there is a similar high-order aberration accumulated from both PPPP and SH, which means that the DM introduces some extra high-order aberrations within closed-loop iterations. These extra aberrations can not be seen by both PPPP and SH, therefore they can not be corrected and are accumulated. In theory the DM should only generate a shape which can be decomposed into 12 DM modes, as the DM commands are 12 Zernike coefficients. However the DM apparently generates those extra high-order aberrations during iterations and causes the pattern in Fig. 5.12b and Fig. 5.12c. That is because the DM shape is not the same even if the same DM voltages are added due to large hysteresis, and therefore the actual shape generated by the DM is not exactly a combination of 12 DM modes. Despite the imperfection of the DM, the two methods (PPPP and SH) produce similar PSFs, which implies that PPPP is as good as the SH.

5.5 Summary

In this chapter we demonstrate the feasibility of Projected Pupil Plane Pattern associated with its wavefront sensing and reconstruction methods from a laboratory setup. It has been demonstrated that the PPPP signal is generated during the upward propagation and the return path can be neglected if we bin the image of the scattered patterns to 32×32 pixels. Two calibration methods are used: the theoretical one and measured calibration. The advantage of the theoretical calibration is that it can be theoretically calculated and therefore fairly easy to obtain, and a distorted wavefront can be reconstructed. The disadvantage is that

it is based on the simulated Zernike polynomials, thus the difference between the simulated and generated Zernike modes will introduce errors when trying to do closed-loop control. We have used the theoretical calibration for the wavefront measurement only and the reconstructed phase shows great similarity compared with the reconstructed phase from the SH WFS. As for the measured calibration, it can connect the PPPP signal directly with the DM voltage command. So it can be used for closed loop control. We have analyzed the effect of the binned pixel number N and the closed-loop gain for PPPP. From the closed-loop result of a random aberration generated by the DM, we can confirm that PPPP can achieve equivalent performance to a SH WFS.

Chapter 6

On-sky implementation

The on-sky experiment to verify PPPP technique was originally planned to be implemented on the William Herschel Telescope 4-m telescope, La Palma, Spain. However due to another on-going project, WEAVE (WHT Enhanced Area Velocity Explorer)[95], it has to be moved to other telescopes. Craig Smith, James Webb and Mark Blundell from Electro Optical Systems (EOS) Space Systems offered the opportunity to test PPPP on-sky using their Debris Laser Ranging (DLR) system[96] on Mt Stromlo, Australia. EOS is motivated towards implementation/validation of PPPP as a general means of retrofitting AO capability to their observatories with minimal overhead. They are currently undertaking a debris laser maneuvering experiment in conjunction with the Space Environment Research Centre (SERC) that demands the use of AO correction of outgoing laser energy. PPPP is an elegant solution in that it allows a direct wavefront measurement of the output laser.

6.1 Experiment design

6.1.1 DLR system

The DLR system is designed for space debris tracking, configured with the 1.8-m telescope, as well as other 1.0-m and 0.7-m telescopes close to each other (see Fig. 6.1). The 1.8-m telescope is used as a beam delivery system, with a Nd:YAG laser

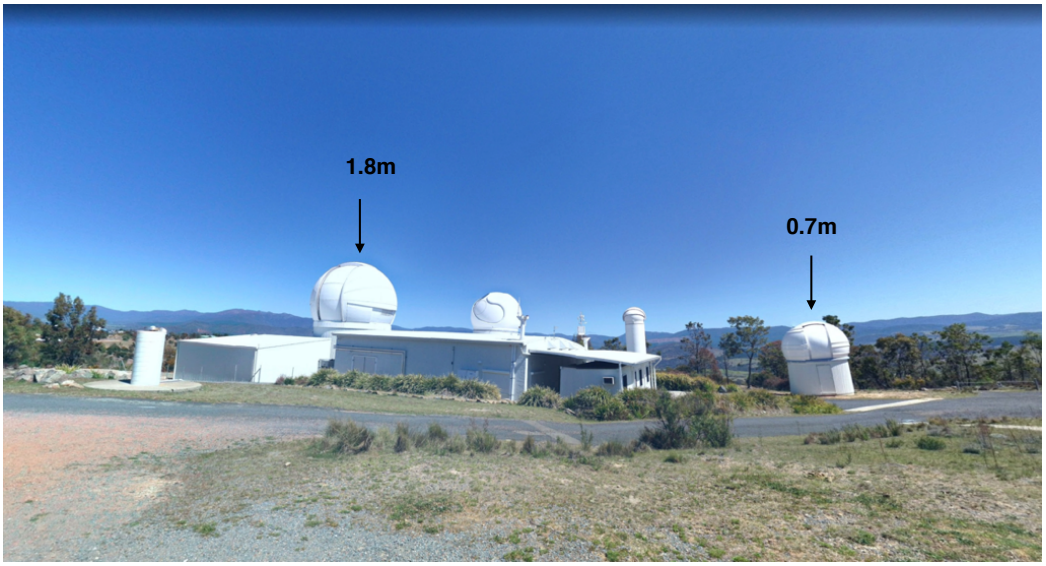

Figure 6.1: EOS DLR system. (Credit to Google Maps).

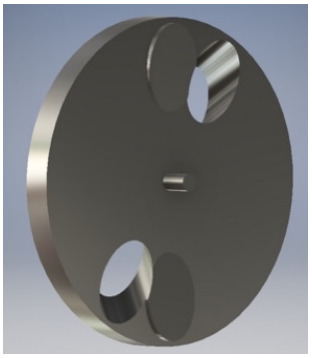

Figure 6.2: Concept of TR disc. This spinning disc is mounted at 45 degree to the incoming laser beam, which fires through the holes (from the rear) (Credit to EOS).

operating at 1.06 μm and providing maximum 760 W average power at 175 Hz. The laser beam is expanded up and then conveyed by the coudé optics to the 1.8-m telescope. This laser can provide high beam quality with great stability, and it can be operated fully automated under software control, and needs minimal maintenance.

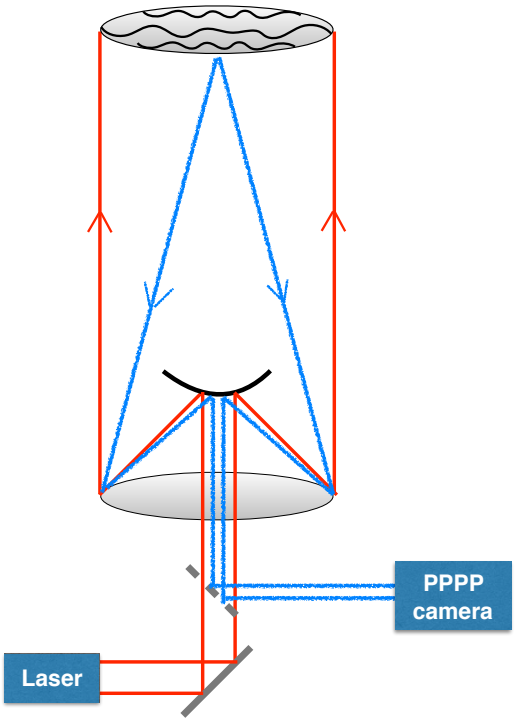

Figure 6.3: Schematic PPPP on-sky prototyping. The red line represents the launched collimated laser beam, and the blue line shows the scattered light from the image plane on sky. The wavelength of the launched laser and scattered light should be the same (1.06 μm), here different colors are used only for convenient distinction.

6.1.2 PPPP implementation with DLR system

The PPPP laser is launched from the primary mirror of the 1.8-m telescope, which requires multiplexing of transmit (outgoing laser pulse) and receive (backscatter detection) optical paths. This architectural complexity has already been implemented as part of the EOS DLR system which makes it a possible development platform for extension. However this implementation of PPPP is still technically challenging for several reasons. Foremost is the need to rapidly switch between transmit and receive modes of operation, *i.e.* to receive the Rayleigh backscatter from two distances, typically 10 km away, requires the detectors being ready to detect 66 μs after pulse transmission. As the EOS DLR transmit/receive (TR)

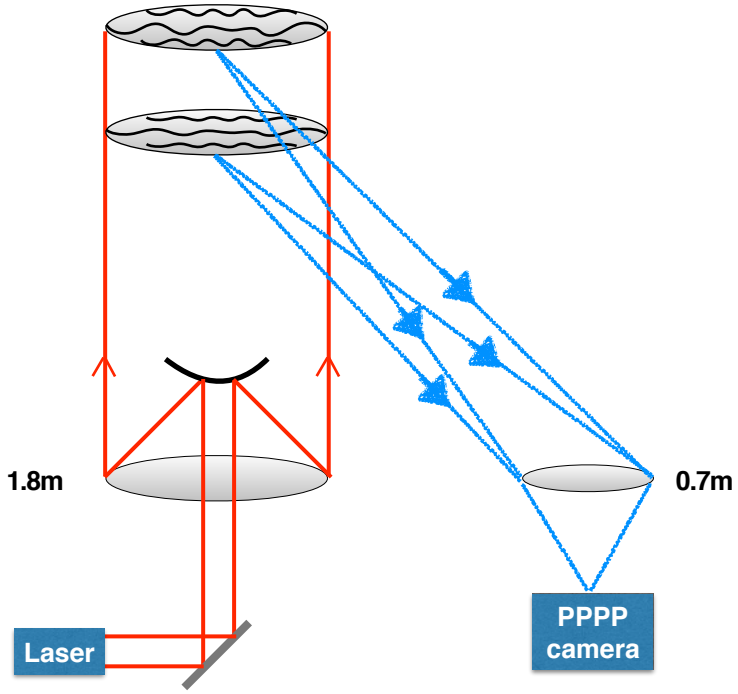

Figure 6.4: A conceptual sketch for an on-sky bistatic configuration of PPPP. The launched laser light (red) from the larger telescope on the left is backscattered (blue) and received by the 0.7-m telescope on the right. Any backscattered light into the 1.8-m telescope is ignored.

switch is currently a spinning mechanical disk/shutter (see Fig. 6.2), this will require significant speedup/redesign if used for PPPP. The second difficulty is how to (economically) take 2 separate images, each conjugated to different atmospheric altitudes and temporally separated by only 66 μs. Then the overall optical layout could be as drawn in Fig. 6.3. It is worth mentioning that an on-axis SH WFS is required to compare with PPPP, but it is not shown in Fig. 6.3.

A more appealing option is a bistatic configuration, where another telescope close to the beam projection telescope is used to capture the backscattered images. This eliminates the need to modify the beam projection system. Luckily the EOS DLR system is equipped with a 0.7-m telescope located 35 m distant (termed A2 telescope). While the DLR 1.8-m telescope emits the laser beam, it is reimaged via

temporal range-gating using the A2 telescope. Fig. 6.4 shows the conceptual sketch for an on-sky bistatic configuration of PPPP. In this configuration, the additional equipment required to be added to the EOS facility will be reduced to:

- On A2 telescope: 1 μm sensitive, low-noise detector, with $\geq$ 37 arcsec FOV (able to image 1.8 m on-sky intensity pattern from 10 km) ;
- On A2 telescope: high-speed wide-field shutter;
- 1.8-m telescope to A2 timing signal, able to synchronize detector readout and shutter with laser pulses.

The A2 detector will be a SAPHIRA APD array[97], which is optically interfaced via a coudé port. The wide-field requirement for the A2 shutter is compatible with the use of a Pockel cell[98]. The 1.8-m telescope to A2 telescope timing signals are at a low rate (175 Hz) and require limited precision ($\sim 6\,\mu$s, equivalent to 1 km range gate) so compatible with COTS (Commercial off-the-shelf) solutions. Reconciliation of PPPP against an independent on-axis SH WFS on the 1.8-m telescope is also required for validation.

6.1.3 PPPP feasibility study with DLR system

A simulation of the PPPP feasibility with EOS DLR system has been carried out with the parameters listed in Table 6.1. Fig. 6.5 shows the PPPP residual WFE in terms of different pixel number N and Zernike modes N_Z. In Fig. 6.5 it is clear that 16 pixels are the minimum number required to sample the images, which equals approximately 11 cm on-sky for each pixel. Increasing N can slightly improve the PPPP performance. Similarly, the highest order of Zernike modes N_Z (tip/tilt modes are removed) can be chosen as 22, which includes all terms to the second order spherical aberration thus is a sensible limit.

Adding the photon and read noise, we now analyze how much detector read noise

Table 6.1: Parameters of PPPP on-sky experiment using EOS DLR system.

Emission telescope: 1.8 m	Receiver telescope: 0.7 m
$h_1 = 12\,\text{km}$	$h_2 = 22\,\text{km}$
$\Delta h_1 = 3\,\text{km}$	$\Delta h_2 = 3\,\text{km}$
Laser wavelength: $1.06\,\mu\text{m}$	Laser pulse power: 4 J
Laser pulse length: 26 ns	Laser pulse rate: 175 Hz
$r_0 = 0.08$ or 0.15 (at 500 nm)	Quantum efficiency: 0.8
Atmospheric transmission: $T_A = 1$	Telescope transmission: $T_0 = 0.5$
Beam profile at pupil	
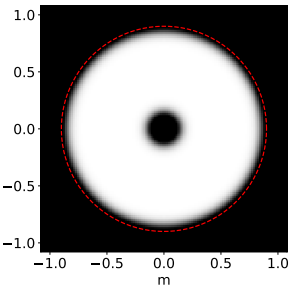	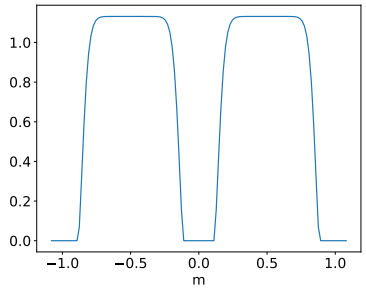

can be tolerated. We use the parameters $N = 16$ pixels and $N_Z = 22$. In Fig. 6.6, for a 4 J pulse, a detector with $\leq 10e^-$ is required.

It is important to note that these results have ignored the tip/tilt component of the wavefront because PPPP cannot detect this component nor can it easily be disassociated from telescope vibrations. Our conclusion is therefore that a demonstration of PPPP using a 1.8-m emission telescope and a 0.7-m receiver telescope, $1.06\,\mu$m laser with 4 J pulse and an infra-red sensitive detector with read-noise of less than $10e^-$, would be a feasible setup. These results are compatible with the SAPHIRA APD array detector, where the read noise can be limited to $0.2e^-$ RMS[97].

6.2 A scoping on-sky run

To familiar ourselves with the EOS DLR system, a scoping on-sky run was carried out on 27/09/2018 on Mt Stromlo, Australia, including recording a sequence of short-exposure images from 0.7-m A2 telescope, and recording slopes simul-

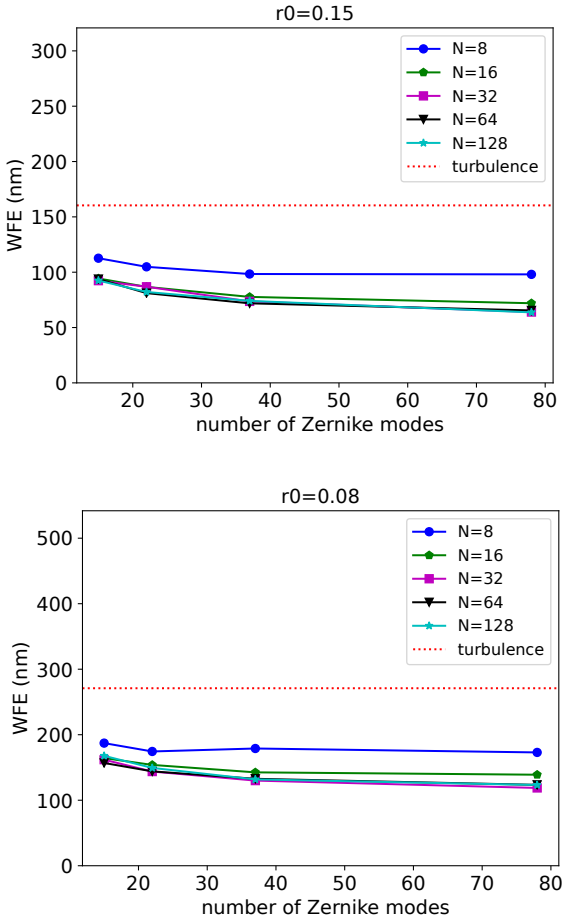

Figure 6.5: Investigation of the number of pixels across the pupil and the number of Zernike modes for reconstruction.

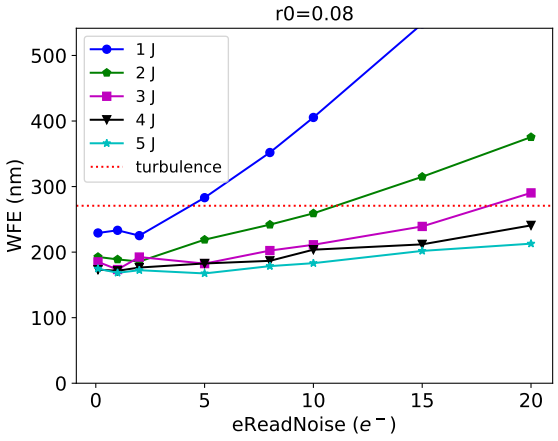

Figure 6.6: A comparison of different read-noise quantities effects on retrieved WFE for the bistatic configuration, assuming $N = 16$ and $N_Z = 22$. Only results with $r_0 = 0.08\,\mathrm{m}$ are shown and results from $r_0 = 0.15\,\mathrm{m}$ are similar.

Table 6.2: EOS System description. The last row is the initial (final) sub-aperture map left (right). Those sub-apertures with a flux less than 62% of the maximum observed sub-aperture flux are removed.

1.8-m telescope pointing			
Latitude	-35° 18' 58.66"	Elevation	770 m
Longitude	149° 0' 35.42"	FK5 catalogue	4120 F5
RA (right ascension)	01h19m58.43s	Magnitude	7.4V
DEC (declination)	-57° 20' 56.3"	Date	27/09/2018 03:04am
0.7-m A2 telescope specification			
Focal length	4.54 m	FOV	0.86 °
Image scale	22 μm/arcsec	Obstruction	47%
Zyla detector specification (A2 telescope)			
Wavelength	600 nm	Pixel number	2560×2160
Read noise	0.9 e^-	Pixel size	6.5 μm
Quantum efficiency	0.82	Type	sCMOS
on-axis SH WFS			
frames	10000	Sub-apertures	24×24
λ	500 nm		
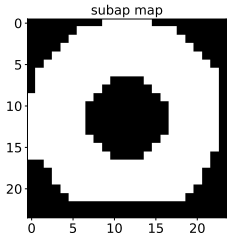		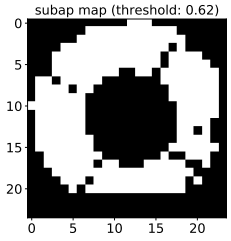	

taneously from an on-axis SH WFS on the 1.8-m laser delivery telescope. When the short-exposure images of the selected star are stacked, these simulate a high-dynamic range long-exposure image, from which the Fried's coherence length r_0 (or seeing) can be estimated. Simultaneously the calibrated slopes from the on-axis SH WFS can be used to estimate seeing, as observed by the 1.8 m telescope. We show an initial result of this seeing comparison in section 6.2.1. Besides the 760 W infrared laser was fired from the 1.8-m telescope and the Zyla camera at the focus of the 0.7-m A2 telescope was set to take the laser plume image. The system parameters are listed in Table 6.2.

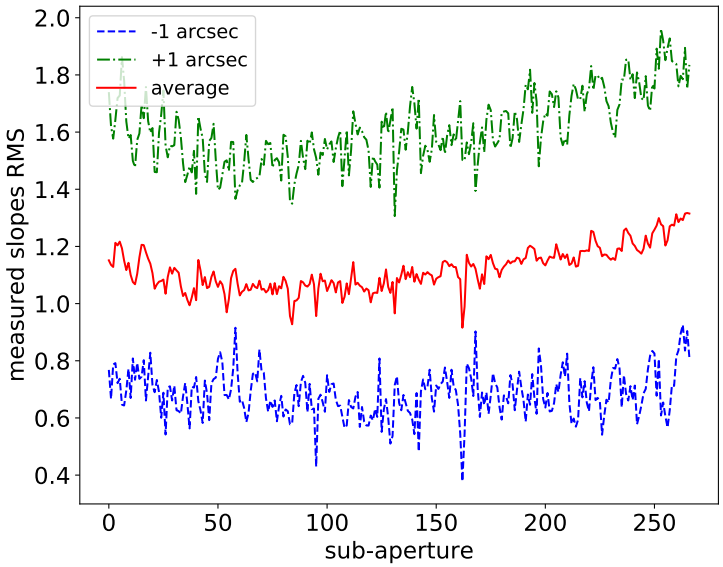

Figure 6.7: The RMS of all slopes as a result of offsetting the telescope by +1/-1 arcseconds in elevation.

6.2.1 Seeing comparison

6.2.1.1 Seeing estimation from SH WFS

The first step is to convert the centroids (measured positions of the SH spots) into physical slopes, which was done via a telescope offset of +1/-1 arcsec. This change is shown in Fig. 6.7 and from the data, we can estimate that the SH WFS plate scale is about 1.12 pixels/arcsec.

Then with the selected sub-apertures' calibrated slopes, the Differential Image Motion Monitor (DIMM) formula[99] allows a connection between the variance of slopes along one axis (here 'x') in the longitudinal and transverse directions between two sub-apertures and r_0

$$\begin{aligned} \sigma^2_{x;l} &= 0.358(1 - 0.541b^{-1/3})\lambda^2 r^{-5/3}_{(0;l)} d^{-1/3}, \\ \sigma^2_{x;t} &= 0.358(1 - 0.811b^{-1/3})\lambda^2 r^{-5/3}_{(0;t)} d^{-1/3}, \end{aligned} \tag{6.1}$$

where the sub-aperture diameter d=1.8/24=7.5 cm and $\lambda = 500$ nm. b is the separation between two selected sub-apertures. An example of the separation $b = 7$

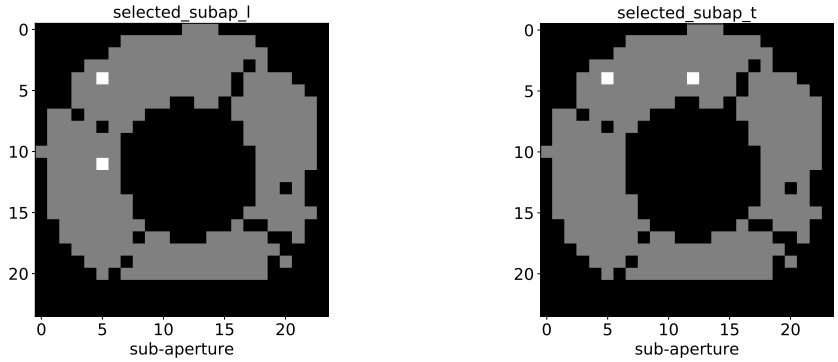

Figure 6.8: Two sub-apertures separated by the same distance in a horizontal (transverse) and vertical (longitudinal) direction ($b = 7$).

of two sub-apertures is shown in Fig. 6.8 and the resulting estimates of transverse and longitudinal r_0 values are: $r_{(0;t)} = 0.055\,\mathrm{m}$ and $r_{(0;l)} = 0.065\,\mathrm{m}$ at 500 nm.

According to Sarazin and Roddier[99] the choice of $b = 7$ sub-apertures is optimal, hence we report only this value here. However, analysis of $3 < b < 10$ does not lead to dramatically different values. The average transverse and longitudinal r_0 values from all available sub-apertures are 0.0520 m and 0.0517 m respectively, and finally r_0 (500nm) at Zenith according to equation 1.3 can be computed equaling 5.76 cm.

6.2.1.2 Seeing estimation from short-exposure images

Using the stacked images from the short-exposure images recorded from A2 telescope, we obtain the seeing disc as shown in Fig. 6.9. The cross-section (horizontal) then allows an estimate of the Full Width Half Maximum (FWHM), which can be lead to r_0 according to[99]

$$\mathrm{FWHM} = 0.98 f \times \frac{\lambda}{r_0}, \tag{6.2}$$

where $f = 4.54\,\mathrm{m}$ is the telescope focal length. From equation 6.2 we can make an estimate of elevation-dependent seeing, $r_{(0;EL)}$ (600nm) = 7.6 cm and zenith-

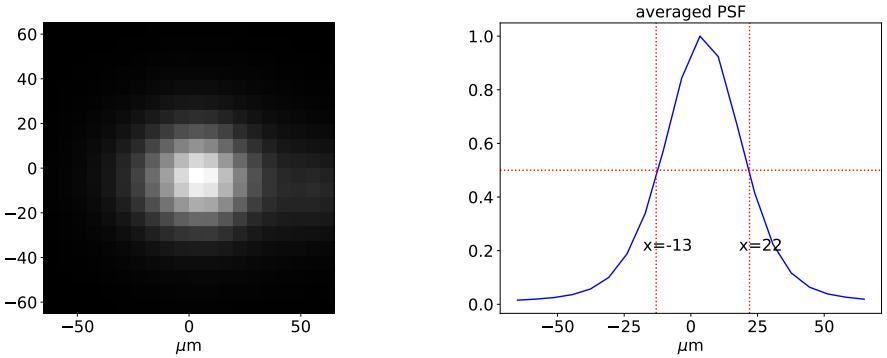

Figure 6.9: The average short-exposure images from A2 telescope.

pointing seeing r_0 (600 nm) = 8.3 cm (equation 1.3). Converting values further to a standard wavelength of 500nm, we have r_0 (500 nm)= 6.8 cm at zenith.

6.2.2 Imaging laser plume

As an initial on-sky test, we have launched the 760 W 1.06 μm pulsed laser from the 1.8-m telescope and the Zyla camera at the focus of the 0.7-m A2 telescope was set to take the laser plume image. One example image is shown in Fig. 6.10. As no shutter system and sensitive, low-noise detector were installed at that time, this image can not be taken for PPPP analysis but gives us good experience of calibrating the system, launching the powerful laser, recording images, etc. We plan to carry out the first PPPP proof-of-concept on-sky experiment in early 2020 at the EOS DLR system.

6.3 Summary

In this chapter we described an on-sky implementation for PPPP using the EOS DLR system. From a feasibility study we find that a demonstration of PPPP using a 1.8-m emission telescope and a 0.7-m receiver telescope, 1.06 μm laser with 4 J pulse and an infra-red sensitive detector with read-noise of less than $10e^-$, would be a feasible setup. From a scoping on-sky run on 27/09/2018 on EOS DLR system,

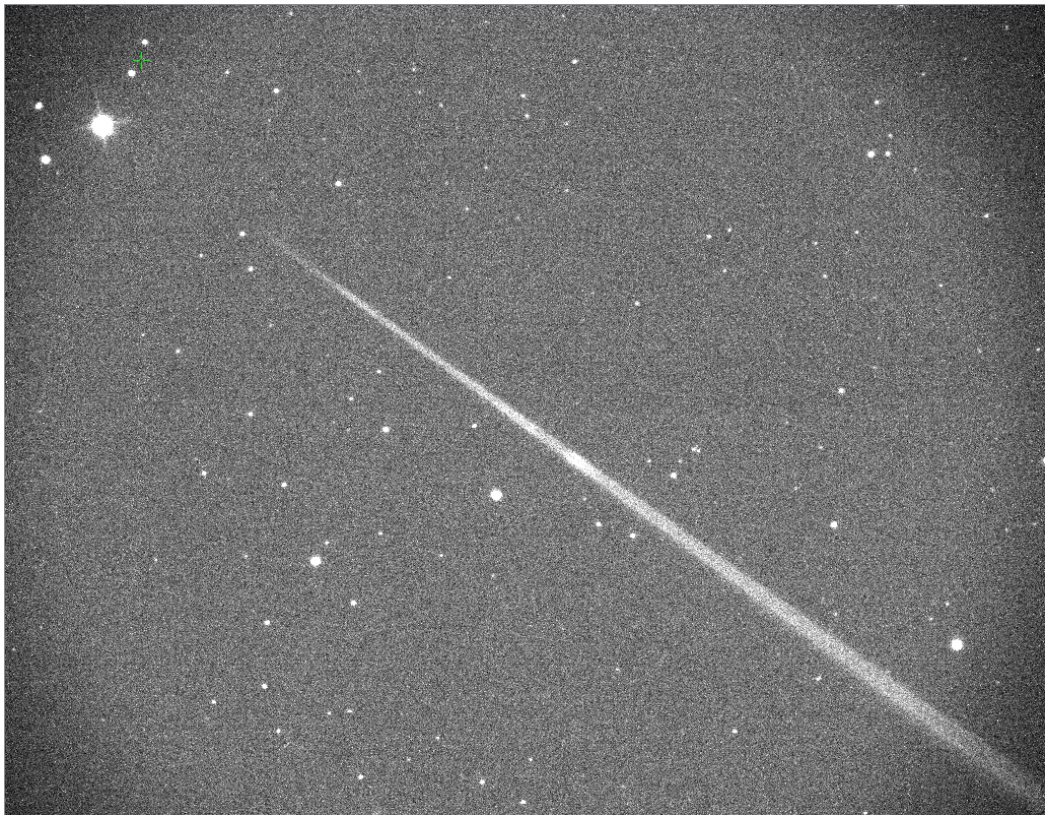

Figure 6.10: Image of laser plume (with a 1.06 μm, 760 W laser) taken on 27/09/2018.

a comparison of estimating the seeing r_0 from both the on-axis SH WFS and a set of short-exposure images from A2 0.7-m telescopes is made in section 6.2.1. The estimated r_0 at 500 nm at zenith is around 0.06 m. This scoping on-sky run gives us a good experience of calibrating the system, launching the powerful laser, recording images, etc., and lays the foundation for the next on-sky run planned in early 2020.

Chapter 7

Conclusion

The aim of this work has been to develop an alternative LGS configuration: Projected Pupil Plane Pattern, to eliminate the Focal Anisoplanatism in astronomical LGS AO systems. Such a technique begins with its conceptualisation, then numerical simulation, laboratory experiment, and finally on-sky prototyping.

7.1 Theory

With PPPP, turbulence is sensed during uplink by a laser beam projected as a collimated beam from the whole telescope primary mirror. This automatically eliminates the effects of Focal Anisoplanatism. Phase changes due to the turbulence introduce intensity variations that then increase in amplitude with propagation distance. By observing the distribution of intensities at two distant planes, the Transport-of-Intensity Equation (TIE) can be used to determine the phase aberration encountered during the uplink path. A simple imaging camera can then be used to measure the wavefront by imaging the backscattered light patterns at those two altitudes (h_1 and h_2).

Similar to a curvature WFS, PPPP suffers from the nonlinear effect due to the approximation of the TIE (equation 2.16) and the changing wavefront. From a theoretical analysis of the PPPP nonlinear effect (section 2.3.2), we find that the PPPP nonlinear effect is proportional to the sum of h_1 and h_2. However the PPPP

signal from equation 2.16 shows that $h_2 - h_1$ should be, on the contrary, as big as possible, but within the requirement of equation 2.23 (less than 30 km assuming $r_0 = 0.1$ m at 500 nm and $\lambda = 1.06\,\mu$m). Thus a trade-off choice for h_1 and h_2 should be made. Due to the fact that the Rayleigh LGS can only be detected at an altitude where air density is still high, typically below 25 km[15], and the fact that the atmospheric turbulence between h_1 and h_2 can only be sensed by I_2 (see section 4.2), a good choice would be $h_1 = 10$ km and $h_2 = 20$ km.

7.2 Simulation

The PPPP numerical simulation modelling includes three key steps: upward propagation, return path model and reconstruction. The upward propagation simulation is performed by the Fresnel diffraction (section 3.1.1) together with generating phase screens as the atmospheric turbulence (section 3.1.2). The return path simulation is used to reimage the Rayleigh backscattered intensity patterns on sky, which is simplified as a convolution of the turbulence-introduced downward PSF and the backscattered intensity patterns on sky. The LIDAR equation is used to calculate the number of scattered photons (section 3.2.1). The downward PSF during the return path is modelled (section 3.2.2), and we find that the blurring effect due to the return path can be neglected if the images are binned to 57×57 pixels when $r_0 = 0.15$ m at 500 nm and 28×28 pixels when $r_0 = 0.08$ m. Two reconstruction methods are used, one is the linear method based on the matrix operation (section 3.3.1), and the other is the nonlinear method based on the Artificial Neural Network (section 3.3.3).

Using the PPPP simulation model described in chapter 3, the PPPP performance in terms of various parameters (including the pixel number to sample the images, Zernike modes for reconstruction, propagation altitudes of the two back-scattered images, as well as the initial launching laser beam profile) is analyzed (section 4.1),

and a suitable choice of the PPPP parameters is made (see Table 4.2). Given these simulation parameters, we then investigated the effect of turbulence layer altitudes and found that PPPP is insensitive to the turbulence altitudes as long as the turbulence is below h_1 (section 4.2). Also PPPP has demonstrated great sensitivity and a large dynamic range from an example of four low order aberrations (section 4.3). A detailed SNR analysis was given and it was shown that the major limitation of PPPP is the low SNR, and two attempts to improve the PPPP SNR have been discussed but without success (section 4.4). On the contrary the nonlinear reconstructor based on Neural Network reduced the laser power requirements significantly to $\sim 200\,\mathrm{W}$ from $\sim 1000\,\mathrm{W}$ for useful residual WFE. The simulation results from a full AO simulation platform *Soapy* with a PPPP model integrated is presented in section 4.5. We confirmed that PPPP is free of Focal Anisoplanatism using one turbulence layer at different altitudes (section 4.5.1.1). The results using a more realistic turbulence profile with 20 layers measured at Paranal (Fig. 4.14) is presented in section 4.5.1.2, where we find that PPPP using the linear reconstruction can achieve similar performance as a SH WFS with one single sodium LGS, but only when the laser power is above 500 W. From the closed loop simulation results (section 4.5.1.3), we can infer that the partially measured turbulence between h_1 and h_2 is gradually corrected within several iterations in closed loop. Compared to the linear reconstruction, NN reconstructor has been demonstrated an effective method for lower laser power (section 4.5.2), which can provide $\sim 160\,\mathrm{nm}$ residual WFE with a single 200 W laser on a 4-m telescope. NN reconstructor also provides the possibility of using only one backscattered image instead of two, which points towards a simplified on-sky implementation for PPPP (section 4.5.2.3). Although the simulation shows great potential of PPPP as an alternative LGS wavefront sensing technique, there are a few further investigations required for the future work. One of them is the reconstruction accuracy for each individual Zernike mode as shown in Fig. 4.18, which shows smaller residuals for Zernike polynomials with smaller azimuthal frequency. It suggests that a new sets

of basis functions may perform better than the Zernike modes for PPPP.

7.3 Laboratory experiment

A proof-of-concept laboratory experiment has been built to demonstrate the PPPP technique (chapter 5). It has been demonstrated that the PPPP signal is generated during the upward propagation and the return path can be neglected if we bin the image of the scattered patterns to 32×32 pixels (see Fig. 5.4). Two calibration methods (both are based on the linear reconstruction) are used: the theoretical one and measured calibration (section 5.3). The advantage of the theoretical calibration is that it can be theoretically calculated given the input laser beam profile, and is therefore fairly easy to obtain. Also a distorted wavefront can be reconstructed from the theoretical method. The disadvantage is that it is based on the simulated Zernike polynomials, thus the difference between the simulated and generated Zernike-like modes on the DM (DM modes) will introduce errors when trying to do closed loop control. We have used the theoretical calibration for the wavefront measurement only and the reconstructed phase shows great similarity compared with the reconstructed phase from the SH WFS (section 5.4.1). As for the measured calibration, it can connect the PPPP signal directly with the DM modes. So it can be used for closed loop control. We have analyzed the effect of the binned pixel number N and the closed-loop gain for PPPP, where a choice of $N = 32$ and gain $= 0.6$ is made. From the closed loop results of an example of a random aberration generated by the DM, it is confirmed that PPPP can achieve equivalent performance to a SH WFS (section 5.4.2).

This proof-of-concept laboratory experiment is a milestone between the numerical simulation and the on-sky test as PPPP is very different from a conventional LGS AO system, in terms of the laser launching configuration, wavefront sensing technique and reconstruction process. Similar systems have never been built on the

bench, not to mention on sky. Thus a laboratory demonstration is necessary for understanding the PPPP technique, including extracting the PPPP signal, calibrating the system, reconstructing the phase, and how it behaves compared with a SH WFS, before putting a lot of staff effort and resources into the on-sky experiment. Further experimental analysis could be conducted, in terms of the noise propagation (to qualify the residual WFE for different exposure time or noise level), and include a more realistic turbulence simulator, etc. Also the NN reconstructor is now only tested on the simulated data, and it would be beneficial to try with the bench (or even on-sky) data. To do so a more robust bench without needing to move components manually on the rail is needed as NN trains with a large amount of data and manual control would introduce too much effort to collect all the training data.

7.4 On-sky implementation

An on-sky implementation of PPPP using EOS DLR system is under development. From a feasibility study we find that a demonstration of PPPP using a DLR 1.8-m emission telescope and a 0.7-m receiver telescope, 1.06 μm laser with 4 J pulse and an infra-red sensitive detector with read-noise of less than $10e^{-}$, would be a feasible setup (section 6.1.3). To set up such a system, three additional equipments are required to be added to the EOS facility: 1) a 1 μm SAPHIRA APD array detector at the focus of the 0.7-m receiver telescope; 2) a high-speed (less than 10 μs) Pockel cell shutter system in front of the SAPHIRA detector; 3) timing signal between the 1.8-m emission telescope and 0.7-m receiver telescope. A set of laboratory experiments for characterization of the SAPHIRA APD array, the Pockel cell shutter system (such as FOV, response time, etc) are needed before the on-sky run (planned in early 2020).

From a scoping on-sky run on 27/09/2018 at the EOS DLR system, we managed to build an on-axis SH WFS on the 1.8-m telescope, as well as using the nearby

0.7-m telescope to obverse the same target. A comparison of estimating the seeing r_0 from both the on-axis SH WFS on the 1.8-m emission telescope and the images recorded from the 0.7-m telescopes is made (section 6.2.1). The estimated r_0 at 500 nm at zenith is around 0.06 m. This scoping on-sky run gives us a good experience of calibrating the system, launching the powerful laser, recording images, etc., and lays the foundation for the next on-sky run. We also learned a lesson that the SH WFS camera is overexposed during launching the 760 W laser. Thus a new camera or a blocking unit is required for the SH WFS.

7.5 The future potential of PPPP

PPPP performs as a cone-effect free astronomical LGS SCAO system. To increase the FOV (currently only a few arcseconds), a wide-field PPPP implementation by launching two expanded laser beams of varying degrees of expansion has been proposed. This is an alternative tomography configuration compared to commonly used multiple LGSs in different directions. This upgraded wide-field PPPP can provide larger overlapping area for tomography than other tomography systems such as MCAO and MOAO, thereby conceptually allowing more accurate tomographic reconstruction.

Beyond astronomy, PPPP can be used for other AO applications as well. The most tempting field would be the laser communication or laser launching system such as the EOS DLR system. This is because what PPPP uses to measure the turbulence is the backscattered light from two altitudes, and the backscattered light is just a by-product for the laser launching system. Therefore no additional equipment is required. Furthermore the correction requirement for laser communication is lower than astronomical imaging, thus low order PPPP is sufficient for this application. Besides PPPP measures the turbulence during the upward propagation, which is in the same direction with these systems, and therefore the measurement can be

more accurate using PPPP than those downward methods.

Bibliography

[1] D. F. Buscher, G. D. Love, and R. M. Myers. Laser beacon wave-front sensing without focal anisoplanatism. *Optics Letters*, 27:149–151, 2002.

[2] A. Kolmogorov. The Local Structure of Turbulence in Incompressible Viscous Fluid for Very Large Reynolds' Numbers. *Akademiia Nauk SSSR Doklady*, 30:301–305, 1941.

[3] F. Roddier. The effects of atmospheric turbulence in optical astronomy. *Progess in Optics*, 19:281–376, 1981.

[4] A Consortini, C Innocenti, and G Paoli. Estimate method for outer scale of atmospheric turbulence. *Optics Communications*, 214(1):9 – 14, 2002.

[5] Theodore von Kármán. Progress in the statistical theory of turbulence. *Proceedings of the National Academy of Sciences*, 34(11):530–539, 1948.

[6] J. D. Schmidt. *Numerical Simulation of Optical Wave Propagation.* SPIE Press, 2010.

[7] D. L. Fried. Optical resolution through a randomly inhomogeneous medium for very long and very short exposures. *J. Opt. Soc. Am.*, 56(10):1372–1379, Oct 1966.

[8] J. Hardy. *Adaptive Optics for Astronomical Telescopes.* Oxford University Press, Oxford, 1988.

[9] F. Roddier. Curvature sensing and compensation: a new concept in adaptive optics. *Applied Optics*, 27:1223–1225, 1988.

[10] Julian C. Christou, Giovanna Pugliese, Rainer Köhler, and Jack D. Drummond. Photometric and astrometric analysis of gemini/hokupa'a galactic center adaptive optics observations. *Publications of the Astronomical Society of the Pacific*, 116(822):734–744, aug 2004.

[11] John Edward Bowers Weishu Wu, Aaron R. Hawkins. Design of ingaas/si avalanche photodetectors for 400-ghz gain-bandwidth product. volume 3006, 1997.

[12] J. N. Bahcall and R. M. Soneira. The distribution of stars to V = 16th magnitude near the north galactic pole - Normalization, clustering properties, and counts in various bands. *The Astrophysical Journal*, 246:122–135, May 1981.

[13] F. Roddier. *Adaptive Optics in Astronomy.* Cambridge University Press, 1999.

[14] R. J. Noll. Zernike polynomials and atmospheric turbulence. *J. Opt. Soc. AM.*, 66:207–211, 1975.

[15] Laird A. Thompson and Richard M. Castle. Experimental demonstration of a rayleigh-scattered laser guide star at 351 nm. *Optics Letters*, 17:1485–1487, 1992.

[16] C. E. Max, S. S. Olivier, H. W. Friedman, J. An, K. Avicola, B. V. Beeman, H. D. Bissinger, J. M. Brase, G. V. Erbert, D. T. Gavel, K. Kanz, M. C. Liu, B. Macintosh, K. P. Neeb, J. Patience, and K. E. Waltjen. Image improvement from a sodium-layer laser guide star adaptive optics system. *Science*, 277(5332):1649–1652, 1997.

[17] R. Q. Fugate, David L. Fried, Guillermo A Ameer, Bilgehan Böke, S. Browne, Paul H. Roberts, R. E. Ruane, Glenn A. Tyler, and L. M. Wopat. Measurement of atmospheric wavefront distortion using scattered light from a laser guide-star. *Nature*, 353:144–146, 1991.

[18] A. Bouchez. Keck laser guide star adaptive optics: science verification results. *Proceedings of Advancements in Adaptive Optics*, 5490:321–333, 2004.

[19] K. Strehl. *Theorie des fernrohrs: auf grund der beugung des Lichts.* Number v. 1 in Theorie des Fernrohrs: auf Grund der Beugung des Lichts. J.A. Barth (A. Meiner), 1894.

[20] A. Maréchal. *Etude des effets combinés de la diffraction et des aberrations géométriques sur l'image d'un point lumineux.* SER (Riom). Éditions de la Revue d'optique théorique et instrumentale, 1948.

[21] H. W. Babcock. The Possibility of Compensating Astronomical Seeing. *Astronomical Society of the Pacific*, 65:229, October 1953.

[22] P. Wizinowich, D. S. Acton, C. Shelton, P. Stomski, J. Gathright, K. Ho, W. Lupton, K. Tsubota, O. Lai, C. Max, J. Brase, J. An, K. Avicola, S. Olivier, D. Gavel, B. Macintosh, A. Ghez, and J. Larkin. First light adaptive optics images from the keck II telescope: A new era of high angular resolution imagery. *Publications of the Astronomical Society of the Pacific*, 112(769):315–319, mar 2000.

[23] M. Iye, H. Takami, N. Takato, S. Oya, Y. Hayano, Olivier Guyon, S. Colley, M. Hattori, M. Watanabe, M. Eldred, Y. Saito, N. Saito, K. Akagawa, and S. Wada. Cassegrain and nasmyth adaptive optics systems of 8.2-m subaru telescope. In W. Jiang and Y. Suzuki, editors, *Proceedings of SPIE - The International Society for Optical Engineering*, volume 5639, pages 1–10, 2004.

[24] Bruce Macintosh, James R. Graham, Patrick Ingraham, and et al. First light of the gemini planet imager. *Proceedings of the National Academy of Sciences*, 111(35):12661–12666, 2014.

[25] J. B. Hutchings, J. Stoesz, J-P Veran, and F. Rigaut. 60 Milliarcsecond Near-Infrared Imaging of 3C 273 with Altair and Gemini. *Astronomical Society of the Pacific*, 116:154–160, February 2004.

[26] G. Rousset, F. Lacombe, P. Puget, N. N. Hubin, E. Gendron, T. Fusco, R. Arsenault, J. Charton, P. Feautrier, P. Gigan, P. Y. Kern, A.-M. Lagrange, P.-Y. Madec, D. Mouillet, D. Rabaud, P. Rabou, E. Stadler, and G. Zins. NAOS, the first AO system of the VLT: on-sky performance. In P. L. Wizinowich and D. Bonaccini, editors, *Adaptive Optical System Technologies II*, volume 4839 of *Proc.SPIE*, pages 140–149, February 2003.

[27] Cyril Petit and et al. Saxo: the extreme adaptive optics system of sphere (i) system overview and global laboratory performance. *Journal of Astronomical Telescopes, Instruments, and Systems*, 2:2 – 2 – 17, 2016.

[28] R. M. Myers and et al. NAOMI adaptive optics system for the 4.2m William Herschel telescope. In P. L. Wizinowich and D. Bonaccini, editors, *Adaptive Optical System Technologies II*, volume 4839 of *Proc.SPIE*, pages 647–658, February 2003.

[29] Jennifer E. Roberts and et al. Results from the palm-3000 high-order adaptive optics system. volume 8447 of *Proc.SPIE*, pages 8447 – 8447 – 8, 2012.

[30] R. Q. Fugate, B. L. Ellerbroek, C. H. Higgins, M. P. Jelonek, W. J. Lange, A. C. Slavin, W. J. Wild, D. M. Winker, J. M. Wynia, J. M. Spinhirne, B. R. Boeke, R. E. Ruane, J. F. Moroney, M. D. Oliker, D. W. Swindle, and R. A. Cleis. Two generations of laser-guide-star adaptive-optics experiments at the starfire optical range. *J. Opt. Soc. Am. A*, 11(1):310–324, Jan 1994.

[31] P. L. Wizinowich, D. Le Mignant, A. H. Bouchez, R. D. Campbell, J. C. Y. Chin, A. R. Contos, M. A. van Dam, S. K. Hartman, E. M. Johansson, R. E. Lafon, H. Lewis, P. J. Stomski, D. M. Summers, C. G. Brown, P. M. Danforth, C. E. Max, and D. M. Pennington. The W. M. Keck Observatory Laser Guide Star Adaptive Optics System: Overview. *Astronomical Society of the Pacific*, 118:297–309, February 2006.

[32] Maxime Boccas and et al. Laser guide star upgrade of altair at gemini north. volume 6272 of *Proc.SPIE*, pages 6272 – 6272 – 9, 2006.

[33] Yutaka Hayano and et al. Current status of the laser guide star adaptive optic system for subaru telescope. volume 7015 of *Proc.SPIE*, pages 7015 – 7015 – 8, 2008.

[34] D. Bonaccini Calia and et al. First light of the eso laser guide star facility. volume 6272 of *Proc.SPIE*, pages 6272 – 6272 – 11, 2006.

[35] Laird A. Thompson, Scott W. Teare, Yao-Heng Xiong, Richard M. Castle, Abhijit Chakraborty, Robert A. Gruendl, and Robert W. Leach. UnISIS: Laser guide star and natural guide star adaptive optics system. *Publications of the Astronomical Society of the Pacific*, 121(879):498–511, may 2009.

[36] Christoph Baranec, R. Riddlea, A. N. Ramaprakashb, N. Lawc, S. Tendulkara, Smita Kulkarnia, R. Dekanya, K. Buia, J. Davisa, M. Burseb, H. Dasb, S. Hildebrandta, S. Punnadib, and Robin Smitha. Robo-AO : autonomous and replicable laser-adaptive-optics and science system. Proc.SPIE, 2012.

[37] E. Gendron, F. Vidal, M. Brangier, T. Morris, Z. Hubert, A. Basden, G. Rousset, R. Myers, F. Chemla, A. Longmore, T. Butterley, N. Dipper, C. Dunlop, D. Geng, D. Gratadour, D. Henry, P. Laporte, N. Looker, D. Perret, A. Sevin, G. Talbot, and E. Younger. MOAO first on-sky demonstration with CANARY. *Astronomy and Astrophysics*, 529:L2, May 2011.

[38] J. Osborn, D. Guzman, F. J. de Cos Juez, A. G. Basden, T. J. Morris, E. Gendron, T. Butterley, R. M. Myers, A. Guesalaga, F. Sanchez Lasheras, M. Gomez Victoria, M. L. Sánchez Rodríguez, D. Gratadour, and G. Rousset. Open-loop tomography with artificial neural networks on canary: on-sky results. *Monthly Notices of the Royal Astronomical Society*, 441(3):2508–2514, 2014.

[39] T. Morris, E. Gendron, A. Basden, O. Martin, J. Osborn, D. Henry, Z. Hubert, G. Sivo, D. Gratadour, F. Chemla, A. Sevin, M. Cohen, E. Younger, F. Vidal, R. Wilson, T. Batterley, U. Bitenc, A. Reeves, N. Bharmal, H.-F. Raynaud, C. Kulcsar, J.-M. Conan, D. Guzman, J. De Cos Juez, J.-M. Huet, D. Perret, C. Dickson, D. Atkinson, T. Baillie, A. Longmore, S. Todd, G. Talbot, S. Morris, R. Myers, and G. Rousset. Multiple Object Adaptive Optics: Mixed NGS/LGS tomography. In S. Esposito and L. Fini, editors, *Proceedings of the Third AO4ELT Conference*, page 114, December 2013.

[40] F. Vidal and et al. GeMS: from the on-sky experimental system to science operation. The AO point of view. In S. Esposito and L. Fini, editors, *Proceedings of the Third AO4ELT Conference*, page 46, December 2013.

[41] S. Rabien, R. Angel, L. Barl, U. Beckmann, L. Busoni, S. Belli, M. Bonaglia, J. Borelli, J. Brynnel, P. Buschkamp, A. Cardwell, A. Contursi, C. Connot, R. Davies, M. Deysenroth, O. Durney, F. Eisenhauer, M. Elberich, S. Esposito, B. Frye, W. Gaessler, V. Gasho, H. Gemperlein, R. Genzel, I. Y. Georgiev, R. Green, M. Hart, C. Kohlmann, M. Kulas, M. Lefebvre, T. Mazzoni, J. Noenickx, G. Orban de Xivry, T. Ott, D. Peter, A. Puglisi, Y. Qin, A. Quirrenbach, W. Raab, M. Rademacher, G. Rahmer, M. Rosensteiner, H. W. Rix, P. Salinari, C. Schwab, A. Sivitilli, M. Steinmetz, J. Storm, C. Veillet, G. Weigelt, and J. Ziegleder. ARGOS at the LBT. Binocular laser guided ground-layer adaptive optics. *Astronomy and Astrophysics*, 621:A4, January 2019.

[42] P.-Y. Madec, J. Kolb, S. Oberti, J. Paufique, P. La Penna, W. Hackenberg,

H. Kuntschner, J. Argomedo, M. Kiekebusch, R. Donaldson, M. Suarez, and R. Arsenault. Adaptive Optics Facility: control strategy and first on-sky results of the acquisition sequence. In *Adaptive Optics Systems V*, volume 9909 of *Proc.SPIE*, page 99090Z, July 2016.

[43] O. A. Martin, É. Gendron, G. Rousset, D. Gratadour, F. Vidal, T. J. Morris, A. G. Basden, R. M. Myers, C. M. Correia, and D. Henry. Wave-front error breakdown in laser guide star multi-object adaptive optics validated on-sky by Canary. *Astronomy and Astrophysics*, 598:A37, February 2017.

[44] Stefan Hippler. Adaptive Optics for Extremely Large Telescopes. *Journal of Astronomocail Instrumentation*, 8(2), 2018.

[45] Niranjan A. Thatte and et al. The E-ELT first light spectrograph HARMONI: capabilities and modes. volume 9908 of *Proc.SPIE*, pages 9908 – 9908 – 11, 2016.

[46] E. Diolaiti and et al. MAORY: adaptive optics module for the E-ELT. volume 9909 of *Proc.SPIE*, pages 9909 – 9909 – 7, 2016.

[47] B. R. Brandl, T. Agócs, G. Aitink-Kroes, T. Bertram, F. Bettonvil, R. van Boekel, O. Boulade, M. Feldt, A. Glasse, A. Glauser, M. Güdel, N. Hurtado, R. Jager, M. A. Kenworthy, M. Mach, J. Meisner, M. Meyer, E. Pantin, S. Quanz, H. M. Schmid, R. Stuik, A. Veninga, and C. Waelkens. Status of the mid-infrared E-ELT imager and spectrograph METIS. In *Ground-based and Airborne Instrumentation for Astronomy VI*, volume 9908 of *Proc.SPIE*, page 990820, August 2016.

[48] R. Davies and et al. MICADO: first light imager for the E-ELT. volume 9908 of *Proc.SPIE*, pages 9908 – 9908 – 12, 2016.

[49] T. Morris, A. Basden, T. Buey, F. Chemla, J.-M. Conan, E. Fitzsimons, T. Fusco, E. Gendron, F. Hammer, P. Jagourel, C. Morel, R. Myers, B. Neichel, C. Petit, M. Rodrigues, and G. Rousset. Adaptive optics for MOSAIC: design

and performance of the wide(st)-field AO system for the E-ELT. In *Adaptive Optics Systems V*, volume 9909 of *Proc.SPIE*, page 99091I, July 2016.

[50] A. Szentgyorgyi, D. Baldwin, S. Barnes, and et al. The GMT-Consortium Large Earth Finder (G-CLEF): an optical Echelle spectrograph for the Giant Magellan Telescope (GMT). In *Ground-based and Airborne Instrumentation for Astronomy VI*, volume 9908 of *Proc.SPIE*, page 990822, August 2016.

[51] Rob Sharp and et al. Gmtifs: The giant magellan telescope integral fields spectrograph and imager. volume 9908 of *Proc.SPIE*, pages 9908 – 9908 – 15, 2016.

[52] D. L. DePoy and et al. Gmacs: a wide-field, moderate-resolution spectrograph for the giant magellan telescope. volume 10702 of *Proc.SPIE*, pages 10702 – 10702 – 4, 2018.

[53] D. T. Jaffe, S. Barnes, C. Brooks, H. Lee, G. Mace, S. Pak, B.-G. Park, and C. Park. GMTNIRS: progress toward the Giant Magellan Telescope near-infrared spectrograph. In *Ground-based and Airborne Instrumentation for Astronomy VI*, volume 9908 of *Proc.SPIE*, page 990821, August 2016.

[54] Glen Herriot and et al. Nfiraos: first facility ao system for the thirty meter telescope. volume 9148 of *Proc.SPIE*, pages 9148 – 9148 – 11, 2014.

[55] James E. Larkin and et al. The infrared imaging spectrograph (iris) for tmt: instrument overview (conference presentation). volume 10702 of *Proc.SPIE*, 2018.

[56] B. Mobasher, D. Crampton, and L. Simard. An Infrared Multi-Object Spectrograph (IRMS) with adaptive optics for TMT: the science case. In *Ground-based and Airborne Instrumentation for Astronomy III*, volume 7735 of *Proc.SPIE*, page 77355P, July 2010.

[57] M. Akiyama, S. Oya, Y. H. Ono, H. Takami, S. Ozaki, Y. Hayano, I. Iwata, K. Hane, T. Wu, T. Yamamuro, and Y. Ikeda. TMT-AGE: wide field of regard

multi-object adaptive optics for TMT. In *Adaptive Optics Systems IV*, volume 9148 of *Proc.SPIE*, page 914814, July 2014.

[58] Dr. Richard Sebastian Shorter. Principles of adaptive optics, 4th edition, by robert k. tyson. *Contemporary Physics*, 58(4):364–364, 2017.

[59] Richard Hudgin. Wave-front compensation error due to finite corrector-element size. *J. Opt. Soc. Am.*, 67(3):393–395, Mar 1977.

[60] David L. Fried and John F. Belsher. Analysis of fundamental limits to artificial-guide-star adaptive-optics-system performance for astronomical imaging. *J. Opt. Soc. Am. A*, 11(1):277–287, Jan 1994.

[61] O J D Farley, J Osborn, T Morris, M Sarazin, T Butterley, M J Townson, P Jia, and R W Wilson. Representative optical turbulence profiles for ESO Paranal by hierarchical clustering. *Monthly Notices of the Royal Astronomical Society*, 481(3):4030–4037, 2018.

[62] Ronald R. Parenti and Richard J. Sasiela. Laser-guide-star systems for astronomical applications. *J. Opt. Soc. Am. A*, 11(1):288–309, Jan 1994.

[63] Elise V. Viard, Norbert N. Hubin, and Miska Le Louarn. Adaptive optics with four laser guide stars: cone effect correction on large telescopes. volume 4007 of *Proc.SPIE*, pages 4007 – 4007 – 9, 2000.

[64] M. Tallon and R. Foy. Adaptive telescope with laser probe: isoplanatism and cone effect. *Astronomy and Astrophysics*, 235:549–557, 1990.

[65] Marchetti Enrico Ragazzoni Roberto and Rigaut François. Modal tomography for adaptive optics. *Astronomy and Astrophysics*, 342:53–56, 1999.

[66] Roberto Ragazzoni, Enrico Marchetti, and Gianpaolo Valente. Adaptive-optics corrections available for the whole sky. *Nature*, 403:54–56, 2000.

[67] Yael Baharav, Erez N. Ribak, and Joseph Shamir. Atmospheric tomography using a fringe pattern in the sodium layer. *Opt. Lett.*, 19(4):242–244, Feb 1994.

[68] Yael Baharav, Erez N. Ribak, and Joseph Shamir. Wide-field analysis of turbulence layers using fringes in the mesosphere. *J. Opt. Soc. Am. A*, 13(5):1083–1093, May 1996.

[69] Erez N. Ribak, Eugene Gershnik, and Matthew Cheselka. Stellar scintillations as a remote atmospheric wave-front sensor. *Opt. Lett.*, 21(6):435–437, Mar 1996.

[70] Erez N. Ribak. Alternative guide stars for adaptive optics. volume 3353 of *Proc.SPIE*, pages 3353 – 3353 – 10, 1998.

[71] Michael Lloyd-Hart, Stuart M. Jefferies, J. Roger P. Angel, and E. Keith Hege. Wave-front sensing with time-of-flight phase diversity. *Opt. Lett.*, 26(7):402–404, Apr 2001.

[72] Stephan Kellner *et al.* PIGS on sky - dream or reality? In *Proc.SPIE*, volume 5382 of *Proc.SPIE*, pages 5382 – 5382 – 6, 2004.

[73] Gordon D. Love, Richard M. Myers, Richard W. Wilson, David Felix Buscher, Tim Butterley, and Timothy J. Morris. Sensing the atmosphere on the upward path: Lgss without focal anisoplanatism for elts. volume 5382 of *Proc.SPIE*, pages 5382 – 5382 – 6, 2004.

[74] G. D. Love, R. M. Myers, R. W. Wilson, T. J. Morris, and T. Butterley. A Shack–Hartmann wavefront sensor projected on to the sky with reduced focal anisoplanatism. *Monthly Notices of the Royal Astronomical Society*, 368(2):837–843, 05 2006.

[75] T. E. Gureyev and K. A. Nugent. Phase retrieval with the transport-of-intensity equation. ii. orthogonal series solution for nonuniform illumination. *J. Opt. Soc. Am. A*, 13(8):1670–1682, Aug 1996.

[76] Michael Reed Teague. Deterministic phase retrieval: a green's function solution. *J. Opt. Soc. Am.*, 73(11):1434–1441, Nov 1983.

[77] David Redding Mark Milman and Laura Needels. Analysis of curvature sensing for large-aperture adaptive optics systems. *J. Opt. Soc. Am. A*, 13:1226–1238, 1996.

[78] Marcos A. van Dam and Richard G. Lane. Extended analysis of curvature sensing. *J. Opt. Soc. Am. A*, 19:1390–1397, 2002.

[79] T. J. Morris. An experimental rayleigh laser guide star ground layer adaptive optics system for the william herschel telescope. *Ph.D. thesis (University of Durham)*, 2005.

[80] D. Voelz. *Computational Fourier Optics*. SPIE Press, 2011.

[81] R G Lane, A Glindemann, and J C Dainty. Simulation of a kolmogorov phase screen. *Waves in Random Media*, 2(3):209–224, 1992.

[82] J.C. Dainty. *Laser speckle and related phenomena*. Topics in applied physics. Springer-Verlag, 1975.

[83] J. Goodman. *Introduction to Fourier Optics*. 1996.

[84] Huizhe Yang, Nazim A Bharmal, and Richard M Myers. Projected Pupil Plane Pattern: an alternative LGS wavefront sensing technique. *Monthly Notices of the Royal Astronomical Society*, 477(4):4443–4453, 2018.

[85] Frank Rosenblatt. The perceptron: A probabilistic model for information storage and organization in the brain. *Psychological review*, 65(6):386–408, 1958.

[86] Yann LeCun, Yoshua Bengio, and Geoffrey Hinton. Deep learning. *Nature*, 521(7553):436–444, may 2015.

[87] David E Rumelhart, Geoffrey E Hinton, and Ronald J Williams. Learning representations by back-propagating errors. *nature*, 323(6088):533, 1986.

[88] Andrew Paul Reeves. Laser guide star only adaptive optics. *Ph.D. thesis (University of Durham)*, 2015.

[89] Francois Roddier Nicolas Roddier. Curvature sensing and compensation: A computer simulation. volume 1114 of *Proc.SPIE*, pages 1114 – 1114 – 5, 1989.

[90] Christoph Baranec, Dani Atkinson, Reed Riddle, Donald Hall, Shane Jacobson, Nicholas M. Law, and Mark Chun. HIGH-SPEED IMAGING AND WAVEFRONT SENSING WITH AN INFRARED AVALANCHE PHOTODIODE ARRAY. *The Astrophysical Journal*, 809(1):70, aug 2015.

[91] A. Reeves. Soapy: an adaptive optics simulation written purely in Python for rapid concept development. In *Adaptive Optics Systems V*, volume 9909 of *Proc.SPIE*, page 99097F, July 2016.

[92] D Laidlaw, M J Townson, O J D Farley, R W Wilson, T Butterley, J Osborn, A Chacón, F Derie, J Milli, J Navarrete, M LeLouarn, M Sarazin, X Haubois, and E Masciadri. Optical turbulence profiling with Stereo-SCIDAR for VLT and ELT. *Monthly Notices of the Royal Astronomical Society*, 478(1):825–834, 04 2018.

[93] Paul Hickson. Wave-front curvature sensing from a single defocused image. *J. Opt. Soc. Am. A*, 11(5):1667–1673, May 1994.

[94] Huizhe Yang, Nazim Bharmal, Richard Myers, and Eddy Younger. Laboratory demonstration of an alternative laser guide stars wavefront sensing technique—projected pupil plane pattern. *Journal of Astronomical Telescopes, Instruments, and Systems*, 5(2):1 – 10 – 10, 2019.

[95] Gavin Dalton, Scott Trager, and et al. Construction progress of weave: the next generation wide-field spectroscopy facility for the william herschel telescope. volume 10702 of *Proc.SPIE*, pages 10702 – 10702 – 10, 2018.

[96] Craig H. Smith. The EOS Space Debris Tracking System. volume 10702 of *The Advanced Maui Optical and Space Surveillance Technologies Conference*, pages 10702 – 10702 – 10, 2006.

[97] Gert Finger, Ian Baker, Derek Ives Domingo Alvarez, Leander Mehrgan, Manfred Meyer, Jörg Stegmeier, and Harald J. Weller. Saphira detector for infrared wavefront sensing. volume 9148 of *Proc.SPIE*, pages 9148 – 9148 – 16, 2014.

[98] Laird A. Thompson, Scott W. Teare, Samuel L. Crawford, and Robert W. Leach. Rayleigh laser guide star systems: UnISIS bow-tie shutter and CCD39 wavefront camera. *Publications of the Astronomical Society of the Pacific*, 114(800):1143–1149, oct 2002.

[99] M. Sarazin and F. Roddier. The ESO differential image motion monitor. *Astronomy and Astrophysics*, 227:294–300, January 1990.